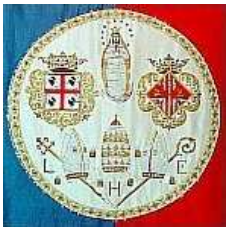

Università degli Studi di Cagliari

Facoltà di Scienze Matematiche, Fisiche e Naturali

Dipartimento di Fisica

PH. D. THESIS IN NUCLEAR, SUBNUCLEAR
PHYSICS AND ASTROPHYSICS

An infrared view of protostellar shocks

Advisors:

Prof. Luciano Burderi

Dott.ssa Teresa Giannini

PhD Student:

Luca Calzoletti

XX Ciclo

Contents

List of Figures

List of Tables

Introduction

The early phases of star formation occur in thick and obscured clouds of dust and molecular gas where, in the inner and denser regions, the material collapses under the influence of self-gravity, originating protostars.
The formation of protostars is one of the less known process of the whole stellar evolution, owing to the difficulty of obtaining detailed observations of the young sources and their environments. Indeed, the accretion processes of the Young Stellar Objects (YSOs) occur at spatial scales of the order of 1-100 AU, corresponding to angular sizes less than 1 arcsec even for the nearest objects, and such observations are prohibitive even at the spatial resolutions obtainable with the modern telescopes. Moreover, these regions are completely hidden at the optical wavelengths, since this radiation emitted by the sources are absorbed by dust, which re-emits at longer wavelengths, from the infrared to the millimetric. An accurate study of the first stages of YSO formation has been possible only over the last decade through the development of new technologies at infrared and millimetric wavelengths, which have allowed to observe deeper into the molecular clouds where protostars are accreting. The incubation period ends when the YSOs have almost completely lost the surrounding envelopes and appear as optically visible pre-main sequence stars in the H-R diagram.
It is during the first stages, when the protostars are embedded into cloud cores, that YSOs accumulate their mass. After a initial phase (main accretion) during which the material collapses in free-fall onto the stellar surface, the accretion process goes on through the circumstellar disc, which carries the material from the outer envelope of gas and dust toward the central protostellar core. As matter spirals through the disc, part of the infalling material is ejected away from the protostar in form of collimated and bipolar jets which remove the excess of angular momentum of the system, so that to the protostar can continue to build up its mass. Accretion and ejection are therefore intimately related, forming two aspects of the fundamental mechanism which regulates the protostellar accretion. Thus, since jets extend up to parsecs from the driving source, they reach less obscured ($A_V \leq 2$) regions with respect to those where the protostars are embedded

($A_V \sim 50$); as a consequence, jets can be observed more easily with respect to the circumstellar disc and they often represent the only observational target to reveal the presence of their driving source or to inderectly infer some properties of the protostars (like accretion rate and age).

Protostellar jets interact with the interstellar medium (ISM), transferring energy and momentum to the quiescent and cold ($T \sim 10$ K) gas of the molecular clouds. This interaction occurs in the form of supersonic waves (*shocks*) which compress and heat the gas; this, in turn, cools by emitting atomic, ionic and molecular lines. Through the analysis of the emission lines it is possible to study the physics and the chemestry of the shocked regions and derive the exchange of energy between the protostar and the interstellar medium.

Both the large variety of chemical elements that contribute to the gas cooling and the temperature and density gradients present in the post-shock regions, make the shock cooling visible in a wide range of wavelengths, from the UV to the radio domine. The near-infrared (NIR) spectral region (1-2.5 μm) is particularly suited to study protostellar shocks because several bright transitions of both molecular and atomic gas can be found in that spectral range. Moreover, unlike for the far-infrared and sub-mm instruments, the new NIR cameras have both a high spectral (up to 40 000) and spatial resolution (tens of milliarcsec) adequate to resolve both a wide number of transitions and the jet morphology. In the NIR bands, the main coolants are molecular hydrogen (H_2) and ionized iron ([Fe II]); the first is the most abundant constituent of the molecular clouds and its transitions are generally observed in warm regions where temperatures of about 3 000 K are reached, while iron, which is generated by the dust sublimation caused by the shock wave, is ionized and excited in the hot regions (T>10 000 K). Hydrogen recombination lines are observed as well, which originate from the hottest regions of the shocked gas. Therefore, the observations of NIR molecular, atomic and ionic lines probe shock regions corresponding to different excitation conditions of the gas.

From a morphological point of view, the jets results in separated, well-collimated shock events (*knots*), which occur in subsequent periods. Often, the jets end with more extended curved regions (*bow shocks*), which are known in literature as HH (Herbig-Haro) objects, from the names of the two astronomers who discovered them in the 1950s. Because of its parabolic geometry, the bow shock includes a variety of shocks, from the most violent close to the bow apex, to the less violent and oblique shocks, occurring along the wings of the bow. Therefore, different excitation conditions arise along the surface of a bow shock and, consequently, molecular and atomic lines are likely originated in different locations. Furthermore, the observed transitions can be used to derive, according to the available

theoretical models, both the shock physical parameters, such as temperature, density, ionization fraction, extinction and the kinematical paremeters, such as geometry, radial velocity and the jet inclination angle. The estimates of these parameters in HHs are fundamental to describe the varity of shocks occurring on the bow-shape surface and to provide constraints on the development of refined theoretical models.

In this aspect, the work presented in this thesis deals with a study of HH objects associated with young stellar objects carried out with two different spectroscopic techniques: the "classical" long-slit spectroscopy and the "novel" integral field (IFU) spectroscopy. IFU (Integral Field Unit) represents an innovative technique of investigation, which is capable of dispersing radiation from each point of the field of view, and not only from the region selected by a slit, as occurs in the long-slit or echelle spectroscopy. This new kind of spectroscopy is particularly suitable for studying bow shock structures, since it simultaneously investigates the different segments (bow and wings) occurring on the shock surface.

Long-slit spectroscopical data of a sample of HH objects (HH26, HH120, HH240), acquired in high (R$\sim$10 000) and low (R$\sim$800) resolution mode, are presented. The goal is to systematically analyse this set of bow shocks in order to infer the physical and kinematic properties of each object, trying to derive general results for these kind of sources. Nevertheless, this study highlights that long-slit spectroscopy is quite un-effective in describing a complex shock region, such as a bow shock.

The IFU spectroscopy technique is applied to observe HH99, which represents a well known prototype of bow shock. The diagnostics capabilities of the IFU are tested by obtaining bi-dimensional maps that sample the variations of the physical and kinematic parameters along the structure of the bow shock. The final aim of this analysis is to provide, for the first time, maps of physical parameters of a bow shock region and a set of observational data capable of constraining up-to-date, bi-dimensional shock models.

The thesis is structured as follows: in Chapter 1 a review of the star formation theory of low mass objects is presented, with a description of protostellar jets and HH objects phenomenology. In Chapter 2 the main tools needed to observe, analyse and interpret NIR spectroscopic data are exposed. The basics of the classical theory for planar-shocks are introduced in Section 2.1, with the effects of shock types on the atomic and molecular constituents of interstellar clouds. The planar-shock model is used to describe the bow shock physics in the framework of a paraboloid geometry (Section 2.2). Furthermore, in Section 2.3 is exposed the capability of NIR lines to diagnose physical parameters, using line ratios, is

analyzed . The capabilities presented in Chapter 2 are used to interpret the observations. The analysis and the discussions of the obtained results are given, for the long-slit and IFU spectroscopy respectively, in Chapter 3 and Chapter 4. Finally, the main results of our work are summarized in the Conclusions, considering future developments for the investigation of protostellar shocks by adopting the IFU technique for this purpose.

Chapter 1

The early phases of star formation

1.1 Molecular clouds

Star formation occurs within large and massive structures called *Giant Molecular Clouds* (GMCs). The GMCs are essentially composed of molecular gas, principally molecular hydrogen (H_2), and dust, which represents only 1/100 of the total mass. In spite of the scarce concentration, dust plays a fundamental role in molecular clouds since it blocks light, establishing the extinction properties of a cloud. GMCs are localised mainly on the Galaxy plane and they have a size of a few hundreds of parsec and masses of $10^4 - 10^6$ $M_\odot$ (e.g. Crutcher 1999; Evans 1999). It is estimated (Combes 1991) that more than 50 % of all the interstellar material of our Galaxy is concentrated in GMCs.

GMCs are studied through the analysis of emission lines corresponding to rovibrational transitions of their molecular constituent. The crucial thing is that GMCs are extremely cold objects, having a typical kinetic temperature of about 10 K. Therefore, even though H_2 is the main constituent, it is difficult to detect due to the high temperature ($\simeq$ 500 K) required to excite the molecule.

Thus, the most important tracer commonly used is the CO molecule because it is relatively abundant ($[CO]/[H_2] \simeq 10^{-4}$), it can be excited at low temperatures (T $\simeq$ 10 K) which characterize molecular clouds and its dissociation energy (11.09 eV) causes it to remain in a molecular form up to high temperatures.

The gas and dust distribution throughout the molecular cloud is not uniform, typically displaying very complex and filamentary structures at different spatial scales; the mean densities are of the order of 100 cm^{-3}, but small structures (of 0.1 - 0.4 pc) with density enhancements (up to 10^4 - 10^5 cm^{-3}) and masses in the

range 1 - 10 $M_\odot$ (Crutcher 1999; Evans 1999) correspond to regions (called molecular *cores*) where the star forming process begins because physical conditions for gravitational collapse occur.

1.1.1 Initial condition for collapse

The gravitational contraction of a core in a molecular cloud begins when the thermal pressure of the gas within the core is no longer sufficient to contrast self-gravity. This means, in the classical theory proposed by Jeans (Jeans 1902), that collapse occurs when the gravitational energy of the cloud core is greater than its thermal energy,

$$\mid E_g \mid > E_{th} \tag{1.1}$$

which, for a homogeneous spherical core with mass M, radius R and temperature T, is given by:

$$\frac{3}{5}\frac{GM^2}{R} > \frac{3}{2}\frac{M}{\mu m_H}kT \tag{1.2}$$

where G is the gravitational constant, k the Boltzmann constant, μ the mean molecular weight and m_H the mass of the hydrogen atom.
Usually, this inequality is expressed in terms of the Jeans mass M_J; gravitational collapse begins when the core mass M is greater than M_J:

$$M > M_J = \left(\frac{3}{4\pi\rho}\right)^{1/2}\left(\frac{5kT}{2G\mu m_H}\right)^{3/2} \simeq 6M_\odot\left(\frac{T^3}{n}\right)^{1/2} \tag{1.3}$$

where ρ is the density of the gas and $n = \rho/\mu m_H$ is the numerical density.
In absence of pressure support, the collapse due to gravitation occurs in a free-fall time:

$$t_{ff} = \left(\frac{3\pi}{32G\rho}\right)^{1/2} \simeq 1.4\times10^6\left(\frac{n}{10^3[\mathrm{cm}^{-3}]}\right)[\mathrm{yr}] \tag{1.4}$$

If $T = 10$ K and $n \geq 50$ cm^{-3}, which are typical values for GMCs (e.g. Blitz 1993), we have $M_J \simeq 100M_\odot$ and $t_{ff} \simeq 10^5$ yr; these values are smaller than the observed values of mass (10^4-10^6 $M_\odot$) and lifetime ($> 10^7$ yr) of the clouds. Thus, on the basis of the classical theory, molecular clouds should be small short-lived structures with a star formation rate of about 250-300 $M_\odot$ yr^{-1}, while observations indicate rates of only 3 $M_\odot$ yr^{-1} (Scalo 1986; Zuckerman & Evans 1974) .

The Jeans criterion is thus unable to describe observational data, providing only a necessary and not sufficient condition to have an unavoidable collapse. Therefore other mechanisms capable of hampering and delaying gravitational contraction must be present within the clouds.
Nowadays, three physical mechanisms are believed to concur with the thermal pressure in supporting the core against self-gravity: magnetic field, core rotation and gas turbulence. Thus, from Equation 1.1, the most general condition to be satisfied is:

$$\mid E_g \mid > E_{th} + E_{rot} + E_{magn} + E_{turb} \tag{1.5}$$

Considering again a homogeneous spherical core of mass M and radius R, it is possible to express the new terms in the previous Equation explicitly:

$$E_{rot} = \frac{1}{5} M R^2 \Omega^2 \tag{1.6}$$

$$E_{magn} = \frac{1}{6} B^2 R^3 \tag{1.7}$$

$$E_{turb} = \frac{1}{2} M v_{turb}^2 \tag{1.8}$$

where Ω is the core rotational velocity, B is the magnetic field inside the core and v_{turb} is the turbulence velocity of the molecular gas.
The debate about which of these mechanisms yields the main contribution in controlling star formation in the clouds is still open. We will now briefly describe these terms.

Rotation

Observational data prove that molecular cores have mean rotational velocity values in the order of 10^{-13} - 10^{-14} rad s^{-1}. The derived rotational energies (Equation 1.6) are negligible with respect to the gravitational energies. Thus rotation seems to be ineffective in hampering core collapse (Goodman et al. 1993).

Magnetic field

The presence of a magnetic field B (usually smaller than 10 μG in molecular clouds and up to 50 μG in the cores, Heiles et al. 1993) provides support against gravitational collapse because the ions present in the cloud gas tend to couple with the magnetic field lines. Moreover neutral constituents are affected by this phenomenon, since collisions couple ions with neutrals, resulting in an overall

magnetic pressure which halts and slows down gravitational contraction.
Assuming that the main contribution against gravitational energy (right side of Equation 1.2) comes from the magnetic energy (Equation 1.7), the criterion for core collapse can be expressed in terms of critical magnetic mass M_Φ (Tomisaka et al. 1988):

$$M > M_\Phi \simeq 0.3 G^{-1/2} B R^2 = 200 M_\odot \left(\frac{B}{3[\mu\mathrm{G}]}\right)\left(\frac{R}{1[\mathrm{pc}]}\right)^2 \tag{1.9}$$

If the cloud mass M exceeds M_Φ, the cloud globally implodes forming stars; it is the case of high mass stars in magnetically supercritical cloud cores ($M \gg M_\Phi$), where the collapse takes place in a free-fall time-scale t_{ff}.
Otherwise the formation of low mass stars occurs in magnetically subcritical cloud cores ($M \ll M_\Phi$), which are quasi-static equilibrium structures resulting from the balance of gravitational, magnetic and pressure forces. The core collapse in these systems occurs because of a process called *ambipolar diffusion* (Mestel & Spitzer 1956): since ions and neutrals are not strongly coupled, the neutral can drift across the field lines resulting in a gravitational condensation of the cloud matter without compressing the magnetic field lines. Truly neutral drift motion deforms the magnetic field lines, producing Alfvén waves that dissipate the magnetic field. As a result of these effects, ambipolar diffusion produces the effect of decreasing the critical magnetic mass, so that the core can collapse when $M \gg M_\Phi$ in a time-scale (ambipolar diffusion time t_{AD}) that depends on the efficiency of the coupling between ions and neutrals:

$$t_{AD} = 5 \times 10^{13} \chi\,[\mathrm{yr}] \tag{1.10}$$

where χ is the degree of ionization, i.e. the number of ions over the number of neutrals.
For typical values of molecular cores ($\chi \simeq 10^{-7}$, Caselli et al. 1998), $t_{AD} \simeq 5 \times 10^6$ yr, one order longer than the free-fall t_{ff}.
Finally, on the basis of this scenario, usually called the *standard theory*, an age-old problem of star forming systems can be solved: the conservation of angular momentum. Observational evidence shows that the angular momentum of the clouds is much larger than those found in stars. Since the total angular momentum of an isolated system (such as clouds are) must be conserved, the rotation speed should increase as the collapse proceeds, until a centrifugal barrier no longer allows it to progress, halting the star forming process. In collapsing cores with a strong magnetic field, the outgoing Alfvén waves remove angular momentum from the

rotating gas to the surrounding gas on a time-scale less then t_{ff}.
The standard theory was widely accepted in the 80s, until the advent of improved instrumentation and computer modelling techniques showed that the magnetic field is no longer the dominant physical process controlling star formation.

Supersonic turbulence

During the last decade, substantial observational evidence suggests that supersonic turbulence is the main process controlling star formation.
The random supersonic motion in molecular clouds is described by the Mach number $M = v_{turb}/c_s$, where $v_{turb} = \sqrt{< v^2 >}$ is the average speed of the random motions and c_s is the sound speed, and its observational evidence occurs from measures of molecular line widths; these generally indicate velocity dispersion of 4-6 km s^{-1} that cannot be accounted for unless considering non-thermal motions (e.g. Munoz-Tunon et al. 1995).
Turbulent supersonic motion is a dissipative phenomenon able to reallocate energy inside the cloud, providing a global support against gravitational collapse. The dissipation time for turbulent kinetic energy is indeed (Mac Low & Klessen 2004):

$$t_d = \frac{L_d}{v_{turb}} = 3\text{Myr} \left(\frac{L_d}{50[\text{pc}]} \right) \left(\frac{v_{turb}}{6[\text{km s}^{-1}]} \right)^{-1} \tag{1.11}$$

where L_d is the driving scale of the turbulence.
Numerical methods and computer simulations (Pavlovski 2004) demonstrate that supersonic turbulence within large clouds would dissipate in a time-scale which is comparable to the free-fall time-scale (Equation 1.4), then a recurring injection of energy is necessary to maintain turbulence as long as is necessary to obtain the observed core contraction times. Several mechanisms have been considered, such as galactic rotation, MHD wave propagation, protostellar outflows and, in particular, supernova explosions (Mac Low & Klessen 2004).
Moreover turbulence may promote local collapse through the formation of local density enhancements; passing shock front compresses the gas creating a Jeans unstable clump which gravitationally contracts and decouples from the turbulent flow.

1.2 The birth of low mass stars

Once the conditions for gravitational collapse are reached, accretion from surrounding material leads the star formation process.
The evolution of a *Young Stellar Object* (YSO) includes two fundamental phases: the protostellar phase and the pre-main sequence phase.
Protostars are contained within their envelope from which they are drawing material. In this phase the protostar acquires about 90% of its final mass and the accretion process is accompanied by the ejection of a powerful bipolar outflow. The interaction between stellar outflows and the cloud medium provides a very powerful tool to characterize the physical conditions where star formation occurs, and it represents the issue of this thesis.
Because of their circumstellar envelope, protostars are highly obscured and are very difficult to detect directly; at optical wavelengths, they are completely hidden, while at longer wavelengths such as the near-infrared (NIR) the obscuration caused by dust grains is considerably less, even if the protostars are still too deep to be detected directly. The study of the outflows therefore provides an important sign to gain knowledge of the evolution of the protostars themselves.
At NIR wavelengths, the best conditions to study the outflow-environment interactions are reached, given the reduced extinction and the high spatial and spectral resolution of modern telescopes.
Longer wavelengths, such as far-infrared (FIR) and sub-millimetre, must be reached in order to observe the regions close to the protostar, where the surrounding material is heated by both the accretion process and radiation.

1.2.1 The Protostellar phase

The theory of low mass star formation (Stahler et al. 1980a,b) assumes that the molecular core about to collapse is schematized as an isothermal sphere in quasi-equilibrium between thermal pressure and gravity. Thus it presents a density profile $\rho \propto R^{-2}$ and, when the collapse starts, the material is throw down according to the free-fall time-scale (see Equation 1.4).
Since $t_{ff} \propto \rho^{-1/2}$, the central zone collapses more rapidly than the outer part, resulting in a contraction which propagates from the inside to the outside at the sound speed velocity $c_s = (kT/\mu m_H)^{1/2}$ (*inside-out collapse*). Therefore a protostellar core in hydrostatic equilibrium is assembled, which accretes matter from the surrounding envelope.
At time t from the beginning of the collapse, the border between the infalling

envelope and the outer region, which is still in an equilibrium condition between gravity and thermal pressure, is given by the infall radius $R_{inf} = c_s t$, that is the distance covered by the wave which propagates the collapse from the core towards the outer envelope. Inside the infalling envelope, material falls towards the centre at the free-fall velocity

$$v_{ff} = (2GM/R)^{1/2} \tag{1.12}$$

The accretion rate is:

$$\frac{dM}{dt} \equiv \dot{M}_{acc} = \rho 4\pi R^2 c_s = 2\frac{c_s^3}{G} \tag{1.13}$$

This depends on the sound speed in the medium and, since for the protostellar cores $c_s \simeq 0.3$ km s^{-1}, one derives accretion rates in the order of $10^{-5} - 10^{-6}$ M$_\odot$ yr^{-1}.

In a protostellar object, the core temperature is not high enough to permit injection of the hydrogen fusion reaction and the luminosity is given by the accretion process, which is determined by radiation of the gravitational energy of the infalling matter that strikes the protostellar core. The accretion luminosity is given by:

$$L_{acc} = \frac{GM\dot{M}_{acc}}{R} \tag{1.14}$$

where M and R are referred to the mass and radius of the central core. For typical values of 1 $M_\odot$ and 4 $R_\odot$, the luminosity is $50L_\odot$; a protostar is therefore much brighter than a main sequence star of equal mass.

Even if the rotation of the molecular cloud is insufficient to prevent collapse, it strongly affects the accretion process of the protostars. Once the cloud is rotating at an angular velocity Ω, the infalling material (i.e. located at $R < R_{inf}$, where R_{inf} is the external radius of the infalling envelope) transports a certain value of angular momentum; since the latter must be conserved, the tangential velocity V_t grows as long as the material approaches the core;

$$v_t = \frac{\Omega R_{inf}^2}{R} \tag{1.15}$$

The accretion can normally continue until the distance R_c is approached, where the condition $v_t = v_{ff}$ occurs; here the material finds a centrifugal barrier that prevents it from falling to the central core. The accretion is blocked and the stars

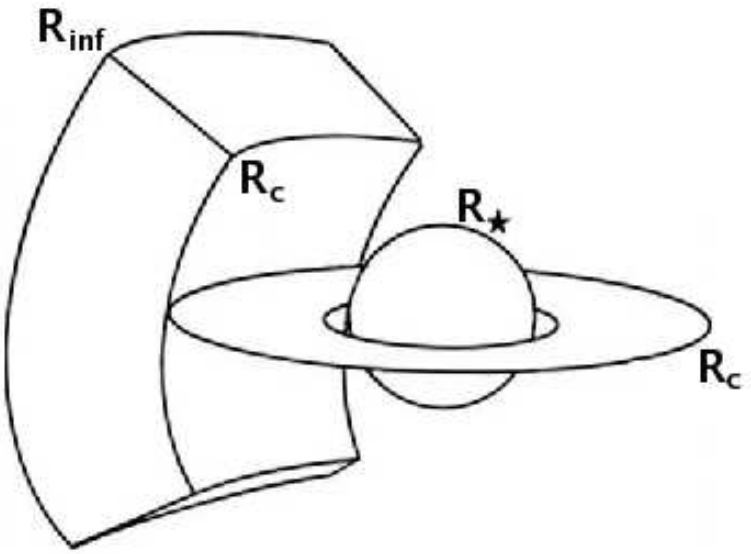

Figure 1.1: Schematization of the protostar surrounding region, where $R_\star$, R_c, and R_{inf} define the protostellar core, the accretion disc and the infalling envelope respectively.

cannot be formed.

Inevitably a mechanism able to disperse angular momentum must exist; when the envelope material reaches R_c, it accumulates on an *accretion disc* around the source and from there it spirals onto the central protostar losing angular momentum for viscous friction. The expression for R_c, which defines the outer radius of the accretion disc, comes from the condition $v_t = v_{inf}$, using Equations 1.12 and 1.15,

$$R_c = \frac{\Omega^2 R_{inf}^4}{2GM} \tag{1.16}$$

The structure of a protostar during the main accretion phase is schematized in Figure 1.1. Four different regions can be discriminated: a hydrostatic nucleus of radius $R_\star$, an accretion disc ($R_\star < R < R_c$), an almost spherical envelope in free fall towards the core ($R_c < R < R_{inf}$) and a static and isothermal outer envelope ($R > R_{inf}$). R_c and R_{inf} have values of the order of 10^{14} cm and 10^{16} cm, respectively.

1.3 Protostellar flows

Observations show that during the accretion process some of the material is ejected at high velocity (100 - 300 km s^{-1}) away from the protostar in the form of bipolar *jets* (Richer et al. 2000). These supersonic jets shock the interstellar medium, gen-

erating *knots* and *bow shock* structures and sweep away the surrounding material forming extended *outflows* (see Figures 1.2, 1.3 and 1.4).

1.3.1 Jets and outflows from protostars

The protostellar jet is another mechanism, like is the protostellar disc, through which the excess of angular momentum is removed from the system. In fact, if all of the angular momentum of the disc were transferred to the central object, this would soon reach a high rotational velocity which would increase the centrifugal force at the stellar surface preventing any further accretion.
Several theories have been formulated to explain which mechanisms are capable of accelerating, collimating and finally ejecting the infalling material. The prevalent interpretation is that jets are powered by the accretion and that the stellar magnetic field is responsible for the ejection process.
The evidence of a connection between jet and disc is based on various observational results (Bachiller 1996); jets and outflows are commonly found in YSOs together with circumstellar discs and their axes are found to lie always perpendicular to the disc planes. Moreover, jet evolution is linked with the accretion history of the protostar; fast and more collimated jets are associated with the early phase, whereas slow and less collimated jets are associated with evolved protostars, and the jet mechanical luminosity is correlated with the bolometric luminosity of the source, which is driven by accretion (Bally & Lada 1983).
In YSOs, the ejected mass and momentum are too great to be driven only by radiation pressure from the central source; consequently the most favoured mechanism involves magneto-centrifugal acceleration from the circumstellar disc described by a Magnetised-Ejection Structure (MAES) (Konigl & Pudritz 2000). In the MAES scheme, three main models are usually considered to describe the injection of stellar wind, which are wind from the protostar alone (Sauty et al. 2002), wind from the accretion disc alone (*disc wind*, Ferreira 2002) and wind from the interaction zone between the disc and the protostar (*X wind*, Shu & Shang 1997).
Even if the details of these models are different, the common basic principle is that a poloidal magnetic field is frozen into the rotating accretion disc. If the field lines are inclined with respect to the rotation axis by a sufficiently large angle (more than 30°), it is energetically favourable for the material to leave the disc plane and to move outwards along the field lines, that rigidly rotate with the disc at constant angular velocity. As the gas moves toward larger radii, it is accelerated by magneto-centrifugal acceleration and further out the field lines become increasingly wound up by the inertia of the attached gas, generating a

strong toroidal component, which is the main agent in collimating the flow along the rotational axis. Thus the angular momentum is carried out by the rotation of the fluid and by the twisted magnetic field.
Such models predict that the mass outflow rate is a constant fraction of the mass accretion rate,

$$\dot{M}_{out} = k\dot{M}_{acc} \tag{1.17}$$

where a k value of ~ 0.1 is typically taken in the most favoured models, which is in line with observations (Bontemps et al. 1996).
Figure 1.2 represents a great example of what has been described so far; a powerful bipolar outflow is emerging from a dense molecular core where the protostar accretion process is taking place. The outflow shocks the surroundings, resulting in bright knots and bow-shape morphology regions.

1.3.2 HH objects

High velocity jets from YSOs interact with their surroundings with high supersonic impacts, producing shock waves.
The excited gas restores the accumulated thermal energy through emission lines of the atomic and molecular constituents of the gas, which allow for the shock surfaces to be observed. The resulting shocks excited regions which are seen in the optical bands are called *Herbig-Haro* (HH) objects, from the two astronomers George Herbig and Guillermo Haro which independently, around 1950, noted the presence of strong optical emission lines ([SII], [OII] and H) forming '*little fuzzy blobs nearby'* T Tauri stars in Orion (Herbig 1950; Haro 1953).
At longer wavelengths, the extinction is widely reduced (see Section **??**) and observations of H_2 and CO lines reveal the outflow morphology (see Figure 1.3): in particular, the high abundance of H_2 and the fact that its transitions occur in the NIR, make it an excellent tracer of the shock structure, while the low excitation CO emissions trace the bulk mass swept up by the flow.
Thus from an observational point of view, the outflows result as a flowing structure with velocity ranging from 50 to 500 km s^{-1}, size ranging from 0.1 to 10 pc and lifetime ranging from 10^3 to 10^5 yr (Bachiller & Tafalla 1999); along the outflow, bow-shape shocks are the brighter recurring structures which are seen (see Figure 1.4), suggesting that the interaction between outflow and surrounding medium occurs mainly through a curved shock.

Figure 1.2: Star forming process in a molecular cloud seen with the Hubble Space Telescope (HST). From the dense 'egg' where the protostar is accreting material, a powerful bipolar outflow moves far away, forming knots and bow-shape shock regions.

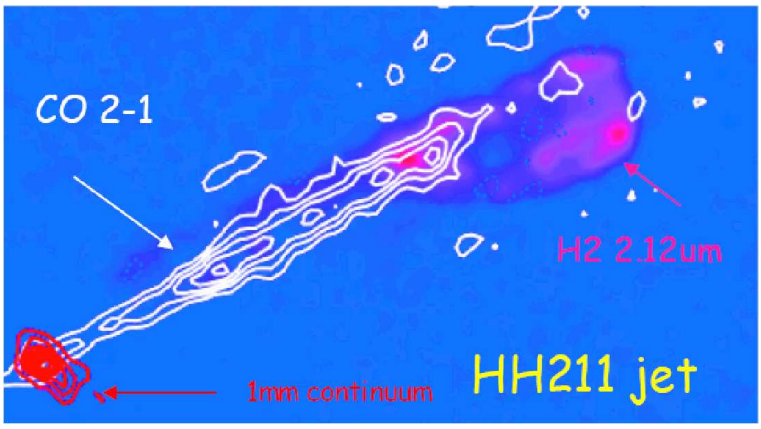

Figure 1.3: The superimposition of CO contours on a H_2 line image at 2.12 μm of the HH211 reveals the whole structure of the outflow (Gueth & Guilloteau 1999).

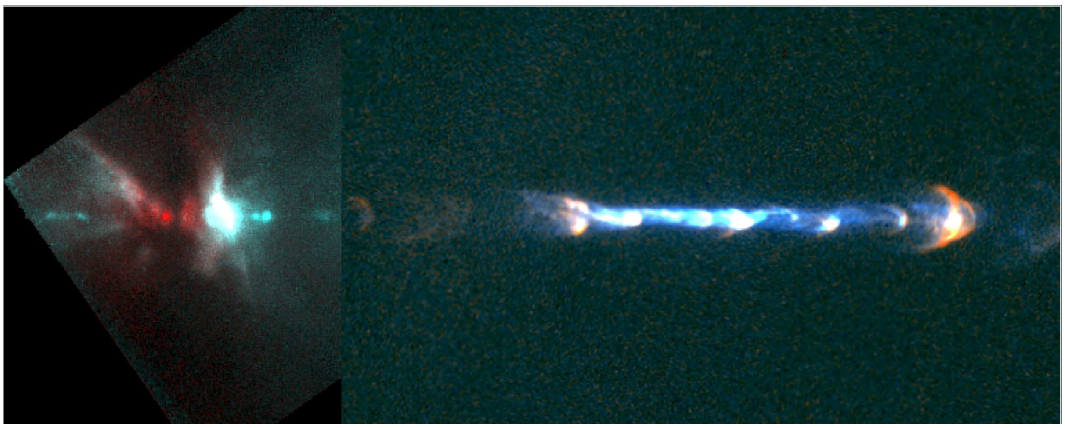

Figure 1.4: A HH111 outflow image composed by an infrared image (left image, around the source) and an optical image (rigth image, the extended jet flow). The shocked regions close to the jet driving source are visible at the infrared wavelength, even if the source is still hidden by the dense protostellar disc. The jet departs from the molecular core and becomes visible at the optical wavelengths, showing its structure composed of shocked knots and bow shape surfaces (HST image database://hubblesite.org/gallery/album/).

1.3.3 Bow Shocks

The structure of a bow shock can be schematized with the 2-D structure in Figure 1.5.

In a schematic bow shock model (better described in Section 2.2) the interaction between the jet coming from the YSO and the ambient medium occurs via two different shocks: a *reverse shock*, which decelerates the supersonic flow and a *forward shock*, which accelerates the slower ambient gas upstream. In the reference frame of the reverse shock, usually called *Mach disk*, upstream material is decelerated and compressed, forming a dense clump from which pressurised material is ejected out sideways; it interacts with the ambient material forming a bow shape forward shock.

Thus, according to this curved geometry, a mixture of excitation conditions are expected in a bow shock: the strongest shock occurs at the bow head and it weakens as it moves towards the bow wings, as the bow surface becomes more oblique with respect to the ambient flow.

According to this scenario, high excitation optical and infrared atomic lines should arise from the head of the bow, where high energetic shocks (J-type shock) dissociate the molecular constituents of the gas, whereas molecular emissions mainly originate in the cooling regions along the wing, where non dissociative shock (C-type shock) are not able to excite the atomic constituents. A description of C- and J-type shocks is exposed in the next Chapter.

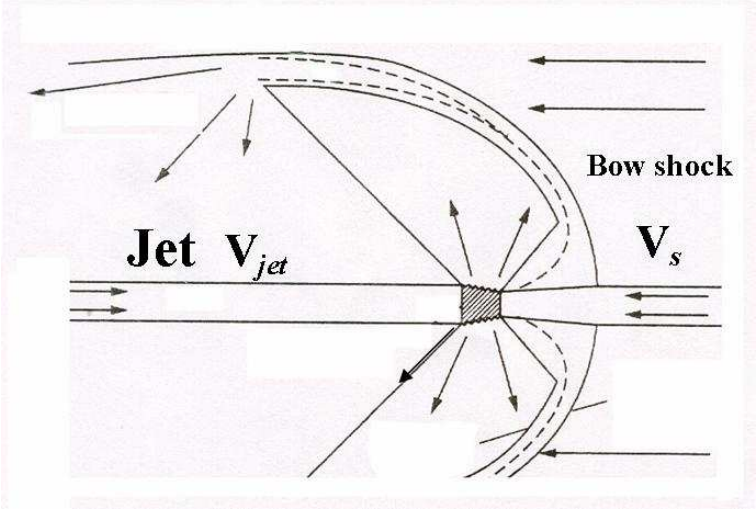

Figure 1.5: Schematic structure of a bow shock. In the reference frame of the bow shock the high speed jet material, entering from the left, is decelerated at the Mach disc, while the ambient medium is decelerated on a different shock front. Between the two surfaces the material is compressed and forced out sideways, forming side shock regions, the bow wings.

Chapter 2

Protostellar shocks: theory and observations

2.1 Interstellar shock physics

A shock is a discontinuity in the physical properties of a fluid; discontinuity implies a substantial change in a physical quantity which characterizes the fluid, on a scale which is smaller than the other physical dimensions.
A medium answers to a mechanical stress with a sound wave that is described by the D'Alembert Equation:

$$\nabla^2 \delta P = \frac{1}{c_s^2} \frac{\partial^2 \delta P}{\partial t^2} \tag{2.1}$$

According to Equation 2.1, the pressure wave propagates through the medium at the sound velocity c_s, gently altering the physical variables since the perturbation is dispersed and a new equilibrium configuration is reached. If a perturbation has a speed greater than the sound velocity, there is no wave that can alert the medium of the passage of the perturbation, and it therefore appears as a shock wave.
For the gas in a molecular cloud, typical values for temperature and density result in $c_s \sim 10$ km s^{-1}, thus the protostellar outflows prove to be highly supersonic and their impact with the interstellar medium produces shock waves. The ambient gas is compressed by the shock, then heated and accelerated; subsequently it radiates thermal energy through the emission of atomic and molecular lines. During the impact, important physical and chemical changes on the gas are produced, such as molecular dissociation, atomic ionization, dust grain destruction.

2.1.1 The Rankine-Hugoniot Jump Equations

Considering the supersonic flow as a one-dimensional flow of a fluid with density ρ_1 and pressure P_1, propagating with constant velocity v_1, the shock occurs ideally on a discontinuity surface (*shock front*) perpendicular to the direction of the propagation of the flow. Downstream from the shock front, the fluid has a

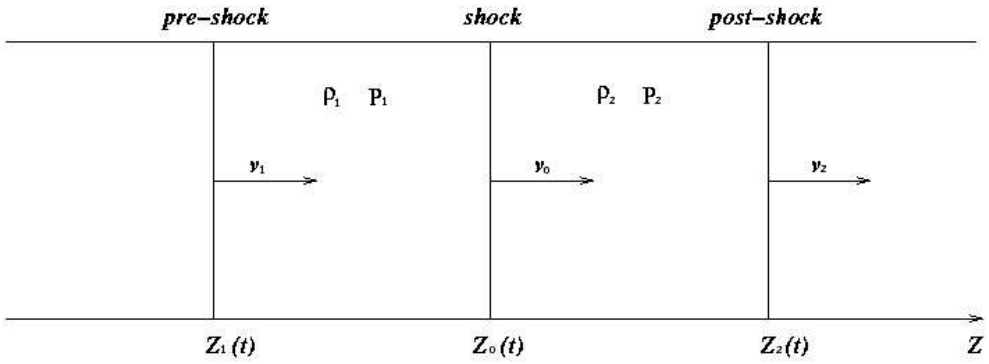

Figure 2.1: Schematic view of a planar shock. z_0 represents the shock front position, while z_1 and z_2 are comoving surfaces into pre-shock and post-shock fluids, respectively.

different density, pressure and velocity (*post-shock fluid*), which are denoted with subscript 2 to distinguish them from pre-shock quantities (subscript 1) (see Figure 2.1).

To derive how the pre-shock quantities are linked to the post-shock quantities, we can fix the conservation of mass, momentum and energy through the shock front; let the z-axis be the direction of propagation of the flow, and $z_1(t)$, $z_0(t)$, $z_2(t)$ the positions of the surfaces, comoving with the fluid, located respectively upstream, on the shock front and downstream.

Thus, we can note that there is no variation of mass inside the volume enclosed by the upstream and downstream surfaces;

$$\frac{d}{dt}\int_{z_1(t)}^{z_2(t)} \rho \, dz = 0 \tag{2.2}$$

Moreover, the variation in the linear momentum is produced by a pressure variation between P_1, which acts from the outside towards the fluid, and P_2, which acts on the external medium;

$$\frac{d}{dt}\int_{z_1(t)}^{z_2(t)} \rho \, v \, dz = P_1 - P_2 \tag{2.3}$$

Finally, the variation of energy between the two surfaces depends on the variation of the mechanical power per unit area acting on the surfaces:

$$\frac{d}{dt}\int_{z_1(t)}^{z_2(t)} \rho\,(v^2/2+\sigma)\,dz = P_1 v_1 - P_2 v_2 \tag{2.4}$$

where σ is the internal energy. Equation 2.4 does not consider the gravitational potential energy, which could be regarded as a constant across the shock dimension, and the energy lost from the fluid through radiation. This latter approximation is also called *adiabatic condition*.

Let us consider these conditions when we examine the two surfaces close to the shock front; in order to do this, we bring the surfaces $z_1(t)$ and $z_2(t)$ near to each other, until both approach $z_0(t)$. We can perform this limit since the surface positions are arbitrary and the thickness of the shock front (roughly set at one particle mean free path) is small compared with the length scale for variations outside the front.

It is possible to demonstrate (Stahler & Palla 2005) that Equations 2.2, 2.3 and 2.4 become,

$$\rho_2 V_2 = \rho_1 V_1 \tag{2.5}$$

$$P_2 + \rho_2 V_2^2 = P_1 + \rho_1 V_1^2 \tag{2.6}$$

$$\frac{1}{2}V_2^2 + \sigma_2 + \frac{P_2}{\rho_2} = \frac{1}{2}V_1^2 + \sigma_1 + \frac{P_1}{\rho_1} \tag{2.7}$$

where $V_1 = v_1 - v_0$ and $V_2 = v_2 - v_0$ are the upstream and downstream velocity relative to the shock front.

Equations 2.5, 2.6 and 2.7 are the *Rankine-Hugoniot Conditions* (R-H) for a non-radiating (adiabatic) shock. We note that the R-H equations are expressed in the reference frame of the shock front, therefore V_1 is the shock velocity (here after V_s), while V_2 is the post-shock velocity (here after V_{ps}) seen from the shock front. From here on, we will still denote the post-shock quantities with the subscript ps.

Now we can consider the fluid as an ideal gas, then the internal energy $\sigma = 1/(\gamma-1)P/\rho$, where γ is the constant adiabatic index. Thus, using the R-H conditions for an ideal gas, we can write the following equations:

$$\frac{V_s}{V_{ps}} = \frac{\rho_{ps}}{\rho_1} = \frac{(\gamma+1)M^2}{(\gamma-1)M^2+2} \tag{2.8}$$

$$\rho_1 V_s^2 = \frac{P_{ps}}{2}(\gamma+1) + \frac{P_1}{2}(\gamma-1) \tag{2.9}$$

In Equation 2.8 we have introduced the *Mach number* $M = V_s/c_s$, where $c_s = (\gamma P/\rho)$ is the adiabatic sound speed ahead of the shock front. The Mach number provide an evaluation of the strength of the shock: if the shock is a "strong shock" ($V_s \gg c_s$), $M \gg 1$, while for a "weak shock" ($V_s \simeq c_s$) M approaches one. Similarly, the ratio P_{ps}/P_1 can estimate the shock strength, since for a "strong shock" $P_{ps} \gg P_1$, while in the case of "weak shock" $P_{ps} \approx P_1$.
If we consider that a "strong shock" occurs in the fluid, equations 2.8 and 2.9 become:

$$\frac{V_s}{V_{ps}} = \frac{\rho_{ps}}{\rho_1} \simeq \frac{(\gamma+1)}{(\gamma-1)} \tag{2.10}$$

$$\rho_1 V_s^2 \simeq \frac{P_{ps}}{2}(\gamma+1) \tag{2.11}$$

These equations are determined once the gas typology is known; if the fluid is a monoatomic atomic gas, $\gamma = 5/3$, while for a fluid composed of molecular gas, $\gamma = 7/5$.
Thus we can use Equations 2.10 and 2.11 to express the variation of physical quantities crossing the shock front in the case of a strong shock occurring on an atomic ideal gas:

$$\rho_{ps} = 4\rho_1 \tag{2.12}$$

$$V_{ps} = \frac{1}{4}V_s \tag{2.13}$$

$$P_{ps} = \frac{3}{4}\rho_1 V_s^2 \tag{2.14}$$

$$\frac{P_{ps}}{\rho_{ps}} = \frac{3}{16}V_s^2 \tag{2.15}$$

We can interpret these equations declaring that, further ahead on the shock front, the medium is four times more compressed then the pre-shock medium (Equation 2.12) and that it reaches a velocity equal to 1/4 of the shock velocity (Equation 2.13). Moreover 3/4 of the dynamic pressure of the pre-shocked gas is converted into gas pressure after the shock (Equation 2.14).
Equations 2.12, 2.13, 2.14 and 2.15 are the Rankine-Hugoniot Equation for a *Jump* ("J") shock; Jump implies the presence of a discontinuity in the variation of physical quantities, which occurs when the heat deposition length is negligible

compared with the cooling length. Using Equation 2.15 and the state equation for an ideal gas ($P = \frac{\rho kT}{\mu m_H}$, where k is the Boltzmann constant, μ is the mean atomic weight of the gas particles and m_H is the hydrogen mass), the temperature of the shocked gas is:

$$T = \frac{3}{16}\left(\frac{\mu m_H}{k}\right) V_s^2 \tag{2.16}$$

or equivalently, expressing V_s in km s^{-1}, Equation 2.16 can be written in Kelvin units:

$$T = 1.4 \cdot 10^5 \left(\frac{V_s}{100\,\mathrm{km\,s^{-1}}}\right)^2 [\mathrm{K}] \tag{2.17}$$

Discontinuities in flow velocity, temperature and density are shown in Figure 2.2, where the velocity is referred to the ambient gas.

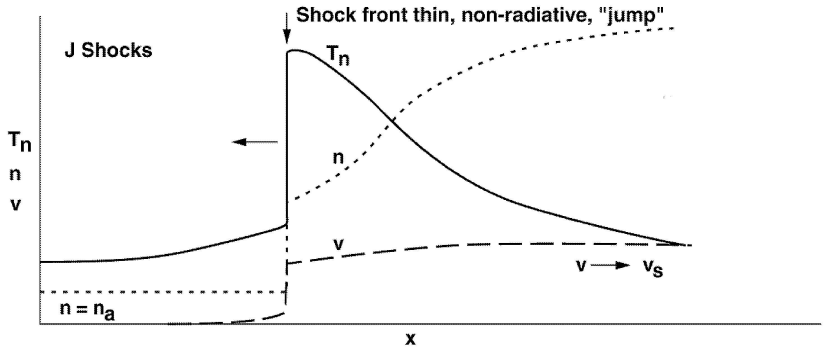

Figure 2.2: Schematic structure for a J-shock. In this framework, the temperature (T), density (n) and velocity (v) variations are reported (Hollenbach 1997).

If the post-shock temperature is sufficiently high, energy lost through radiation must be considered during the shock event. In principle, the loss occurs over a region which is much broader than the characteristic shock front dimension; nevertheless, assuming this cooling distance to be sufficiently small, the entire region can be seen as a single, radiating shock front. In this case, the post-shock gas cools to the pre-shock temperature ($T_{ps} = T_1$) and the shock is called *isothermal*. In isothermal shocks Equations 2.5 and 2.6 are still valid, whilst in Equation 2.7 we have to consider an extra term which represents the flux radiated both in the $+z$ and -z directions. We shall not investigate this condition, but we highlight that the post-shocked gas pressure is expressed by the Equation (Stahler & Palla 2005):

$$\rho_{ps} = M_1^2 \rho_1 \tag{2.18}$$

Equation 2.18 shows that for an isothermal shock, the gas compression can be arbitrarily high, unlike the adiabatic shock, where it is fixed to be 4 (or 6 for a molecular gas). This means that the gas becomes denser as it cools and, since ρV is conserved through the shock front, the post-shock velocity must decrease. The decrease of the post-shock velocity introduced by this cooling effect has been estimated by Hartigan et al. (1987) to be an additional factor of about 10, resulting in $V_{ps} = 1/40 V_s$ for Equation 2.13.

2.1.2 From J-type to C-type shocks

In the previous Section we described the shock conditions without discriminating between neutral and ionised components of the ISM. We have considered these components coupled with each other, establishing a single fluid.
The interstellar medium is however composed of both neutral and ionised material. Since the star formation regions are permeated by a magnetic field, this affects the charged constituent of the medium and, therefore, modify the shock structure. From here on, we refer to "ions" or "charged fluid" in a general sense, including electrons, atomic and molecular ions and as well as charged dust grains.
In the presence of a magnetic field B, we have to consider that disturbances propagate through the magnetic field as an Alfvén wave, for which the propagation speed is the *Alfvén velocity*:

$$V_A \equiv \frac{B}{\sqrt{4\pi\rho}} \tag{2.19}$$

where the magnetic field B is always assumed to be perpendicular to the direction of the shock propagation.
Only ions are subject to the Lorentz force, so only these constituents of the fluid can carry the Alfvén wave; this means that equation 2.19 is the Alfvén velocity of a medium with density ρ only if neutrals and ions are sufficiently coupled. But, since such collisions are infrequent in the ISM, we can assume that ions and neutrals are decoupled and must be regarded as two separate fluids; thus an Alfvén disturbance propagates only through the charged fluid at the ion Alfvén velocity,

$$V_{iA} = \left(\frac{\rho}{\rho_i}\right)^{1/2} \cdot V_A \tag{2.20}$$

Then two different perturbation speeds must be considered: the neutral gas sound speed,

$$V_n = \left(\frac{\gamma n_n k T}{\rho_n} \right)^{\frac{1}{2}} \tag{2.21}$$

and the ion magnetosonic speed V_{ims}, which represent the "signal" speed of the charged fluid (Draine 1980),

$$V_{ims} = \left[\frac{V_{iA}^2 + V_i^2}{1 + V_{iA}^2/V_n^2} \right]^{\frac{1}{2}} \tag{2.22}$$

where n and ρ are the number and mass densities respectively, γ the adiabatic index, k the Boltzmann constant, T the temperature and V_i the ionic gas sound speed.

The structure of the shock depends essentially on the strength of the magnetic field and on whether or not the shock velocity exceeds the ion magnetosonic velocity. If there is no magnetic field, no Lorentz force acts on the charged fluid and then no decoupling occurs between ionic and neutral fluids, which flow at the same velocity. In this case, a discontinuous J-shock occurs when the shock velocity exceeds the sound speed in the medium.

If a magnetic field is present, it acts on the charged fluid creating a disturbance which travels at V_{ims} speed; if V_s is greater than both V_{ims} and V_n, no disturbance can travel ahead of the shock front and a J-shock still occurs. Otherwise, when $V_{ims} > V_s$, but still $V_s > V_n$, the ion magnetosonic wave (*magnetic precursor*) propagates faster than the shock wave and "alerts" the medium ahead of the shock front of the oncoming shock. The magnetic precursor transfers energy and momentum from the charged to the neutral fluid via collisions and afterwards the neutrals are heated and compressed before the arrival of the shock front. What happens when the J-front arrives? This depends on the strength of the magnetic field; for moderate values of B, this interaction does not strongly affect the neutral fluid and a J-shock front is still present in the neutral fluid, while the charged fluid variables change continuously. This shock is called a *J-shock with magnetic precursor*.

With the increase of the magnetic field (or of the ionization fraction) and with the decrease of V_s, the length of the magnetic precursor ($\sim V_{ims} - V_s$) increases; this means that more collisions between neutrals and ions occur ahead of the shock front, resulting in a reduced effect of the neutral fluid discontinuity at the transit of the J-front.

When the magnetic field is in excess of the a critical value B_{crit}, the effects of the magnetic precursor on the neutral fluid are so pronounced that the discontinuity completely disappears and the flow variables become continuous everywhere. Thus the shock becomes a *Continuous* (C-type) shock.
Figure 2.3 shows how the effect of a transverse magnetic field B_0 modifies the structure of the shock from a J-shock, through a J-shock with magnetic precursor to a C-shock. The critical magnetic field dividing J-type from C-type shocks can

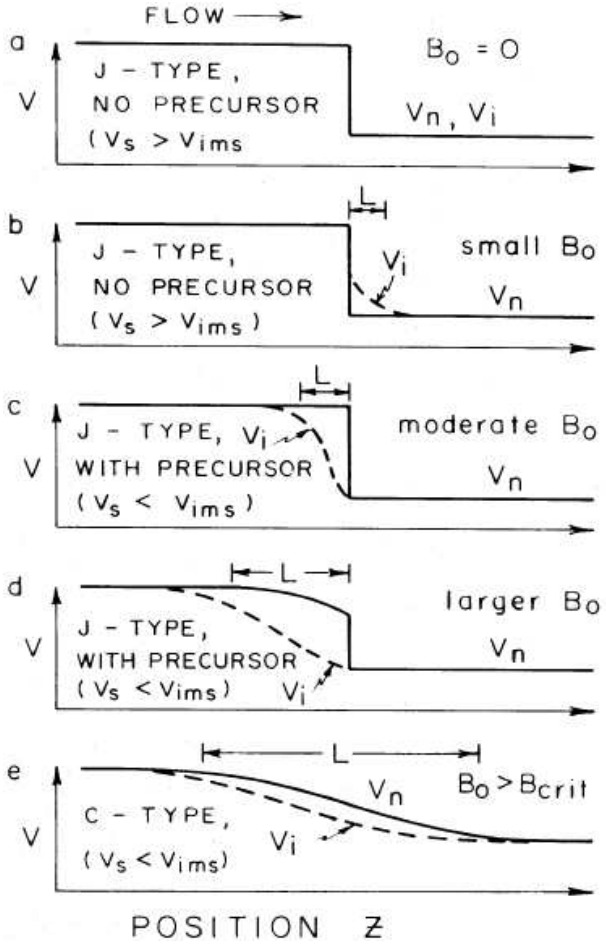

Figure 2.3: Schematic illustration of the effects of a transverse magnetic field B_0 on the shock structure in a partially ionized gas. Neutral velocity v_n and ion velocity v_i are shown in the reference frame comoving with the shock. As B_0 increases, v_i shows a different behaviour with respect to v_n, but the shock acquires a magnetic precursor when $V_{ims} > V_s$ and this can affect the neutral component by a further increasing of B_0. Finally, when B_0 becomes larger than B_{crit}, the J front ceases to exist, leaving a continuous behaviour for both the neutral and ionic constituents (Draine 1980).

be found analytically by requiring the downstream neutral flow to be supersonic for $B > B_{crit}$, such as the upstream neutral flow is, and a continuous solution exists. In a more realistic view, a pratical dermination of B_{crit} is obtained by numerical solutions for the shock structure by starting with small values of B_{crit}

and increasing until the J discontinuty disappears (Draine 1980).
Figure 2.4 shows the behaviour of the gas temperature for a shock which is evolving from a J-shock (upper), through a J-shock with magnetic precursor (middle) to a C-shock (lower). These plots highlight that, while the discontinuity disappears moving through a C-shock, lower values of the peak temperatures are reached.

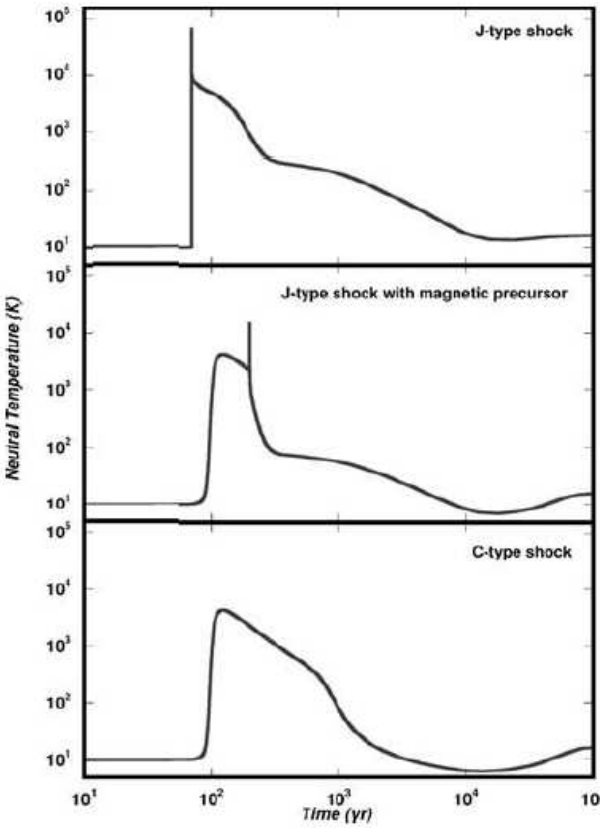

Figure 2.4: Evolution of neutral temperature profile as a function of the flowing time from a J-type to a C-type shock (McCoey et al. 2004).

2.1.3 Shock cooling

In the previous Section we have described the shock mechanisms without considering the effects of the two shock types on the atomic and molecular constituents of interstellar clouds. Now we want to highlight which constituents are the most important elements responsible for the post-shock gas cooling.
J-type shocks reach a peak temperature between 10^4 K and 10^5 K, thus they can dissociate molecules and excite or ionize atoms. As an example, Figure 2.5 shows the evolution of the temperature profile and of the abundance of atomic, molecular and ionized hydrogen for a J-shock (V_s = 25 km s^{-1}, $n_H = 10^4$ cm^{-3} and B = 0, Flower et al. 2003). At the shock front, the temperature rises to $\sim$

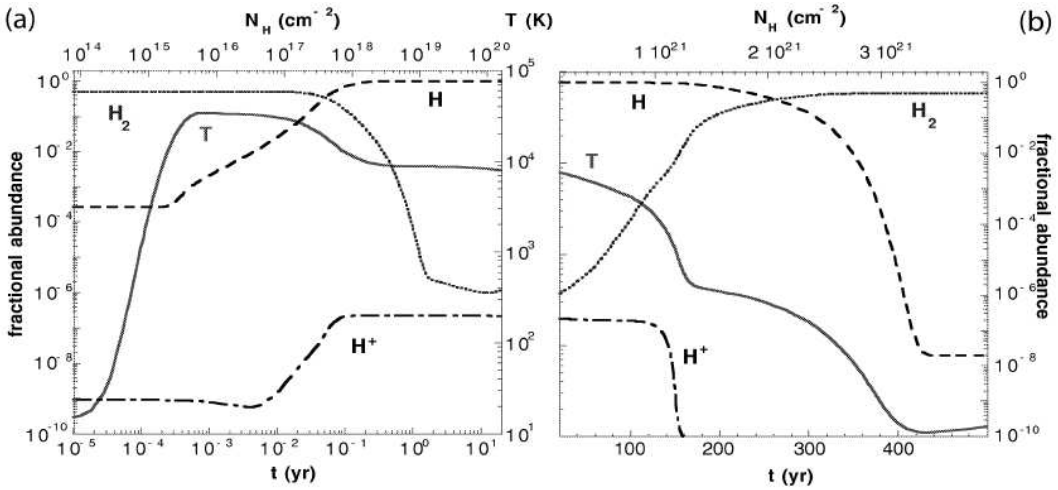

Figure 2.5: The variations of temperature and abundance of atomic, molecular and ionized hydrogen occurring in a J-shock (V_s = 25 km s^{-1}, $n_H = 10^4$ cm^{-3} and B = 0). The abscissa are the flow time and the protons column density N_H. The left panel reproduces the variations in a time interval close to the shock event, while the right panel describes the conditions of the post-shocked gas (Flower et al. 2003).

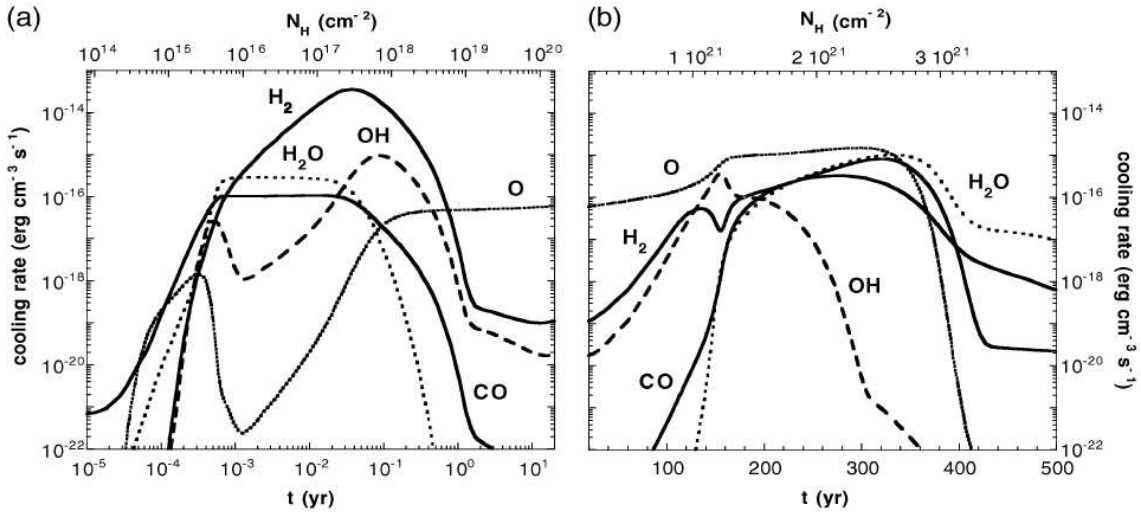

Figure 2.6: The cooling rates of principal atomic and molecular coolants occurring in a J-shock (with the same parameter as in Figure 2.5, Flower et al. 2003).

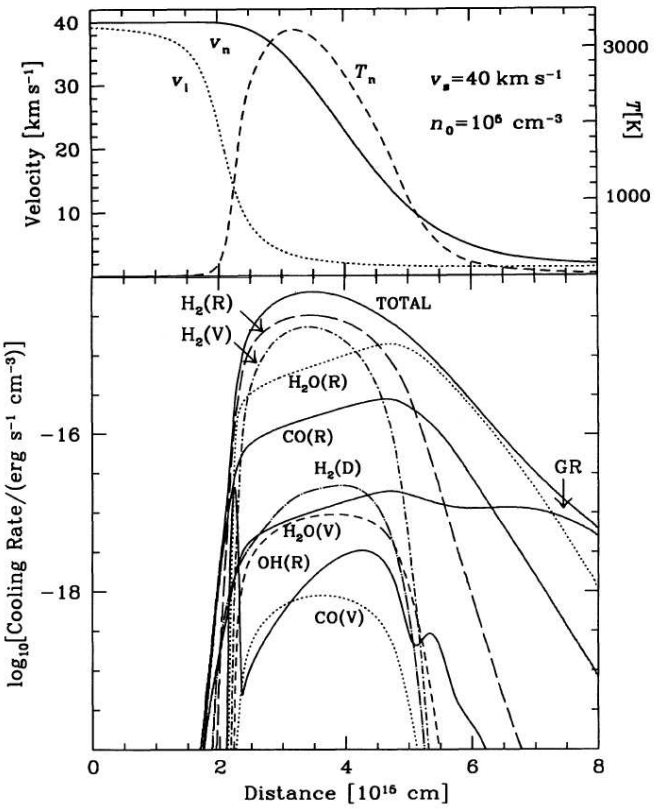

Figure 2.7: The upper panel shows the shock profiles for a 40 km s $^{-1}$ C-shock propagating in a gas with pre-shock H_2 density of 10^5 cm^{-3} and with pre-shock magnetic field of 447 μG. The variations of neutral fluid velocity (v_n), ionized fluid velocity (v_i) and neutral fluid temperature (T_n) are reported as a function of distance through the shocked region. The lower panel shows, for the same C-type shock, the variations with the distance of the cooling rates attributable to the principal cooling mechanisms, which are: vibrational (V) and rotational (R) emissions of molecules; gas-grains collisions (GR); H_2 dissociation (D); all combined (TOTAL) (Kaufman & Neufeld 1996).

33 000 K and then it falls to $\sim$ 10 000 K owing to the H_2 cooling; it then remains approximately constant in a region where the H_2 is dissociated. The displacement between the temperature peak at the shock front and the beginning of the H_2 dissociation is due to a non-instantaneous response of the molecular hydrogen to the sudden temperature increase at the J discontinuity.

In the plateau region, the cooling is dominated by the atomic components of the gas, as is shown in Figure 2.6: from the shock front up to the point where the temperature remains sufficiently high, the cooling rate of the most important constituents of the molecular gas (H_2, CO, OH, H_2O) drops simply because the molecules are dissociated, while atoms remain the principal coolants. The presence of the plateau region demonstrates that the cooling efficiency of atoms (mainly atomic oxygen) is very weak compared to the cooling efficiency of molecules, in particular of molecular hydrogen.

At the edge of the plateau, the decrease in temperature is accompanied by an enhancement of H_2 abundance: this occurs because physical conditions for the H_2 reformation on the grains surface are reached and the molecular hydrogen again becomes the principal coolant.
In C-type shocks, the lower peak temperatures reached (unit of 10^3 K) are not able to dissociate the molecules, which constitute, such as in J-type shocks, the predominant coolants of the post-shocked gas compared with atoms. As an example, the lower panel of Figure 2.7 displays the cooling rates of the principal coolants (H_2, CO, OH, H_2O) as a function of the distance from the shock front, for the C-shock by Kaufman & Neufeld (1996). Molecular hydrogen emits through all the post-shocked region and it is the most efficient coolant compared with the other molecular constituents, especially along the distance interval where the major cooling occurs (that is from 2 $\times 10^{15}$ cm to 5 $\times 10^{15}$ cm, see upper panel in Figure 2.7).
Thus, a common result for both C- and J-type shocks is evident: the molecular hydrogen, whenever it exists, is the most efficient coolant in the shock cooling. When H_2 and the other molecular components are dissociated, the cooling is regulated by the atomic constituents and, as we will see in Section 2.3.3, ionized iron plays a very important role at the near-infrared wavelengths.

2.2 Diagnostics of bow shocks with line profiles and images

In Section 1.3.3 we described the interactions between supersonic outflows and the interstellar medium as shocks occurring on bow shape morphology surfaces, called bow shocks, while in the previous Section, we described the variations of physical parameters across the shock fronts (both for Jump or Continuous shocks) in case of planar shocks, that is where the shock front is schematized as a one dimensional moving plane.
Thus, to describe a bow shock with the knowledge of planar shock models, we can assume that each point of the bow surface acts as a single thin planar shock, with the velocity component perpendicular to the surface becoming the shock velocity acting in that point. Under this hypothesis, the strength of the shock velocity reduces moving from the bow head to the bow flanks. In this framework discontinuous J-type shocks mainly occur on the bow head, where high velocity shocks dissociate molecules and excite the atomic components. Since magnetic fields per-

meate the medium, the presence of a magnetic precursor becomes more important as the velocity decreases, which means that the shocks evolve to continuous C-type shocks moving to the bow flanks. Thus on the bow wings, the molecular gas components are not dissociated and we can expect to observe mainly molecular hydrogen emission.

Several analytic and numerical models, which assume different bow geometries, have been developed over the past years to describe the bow morphology; here we want to describe a simple parabolic bow shape model (see Figure 2.8) and use that model to interpret the observed spectral profiles and spectral images in order to obtain the principal kinematics and geometric parameters. The bow shape is

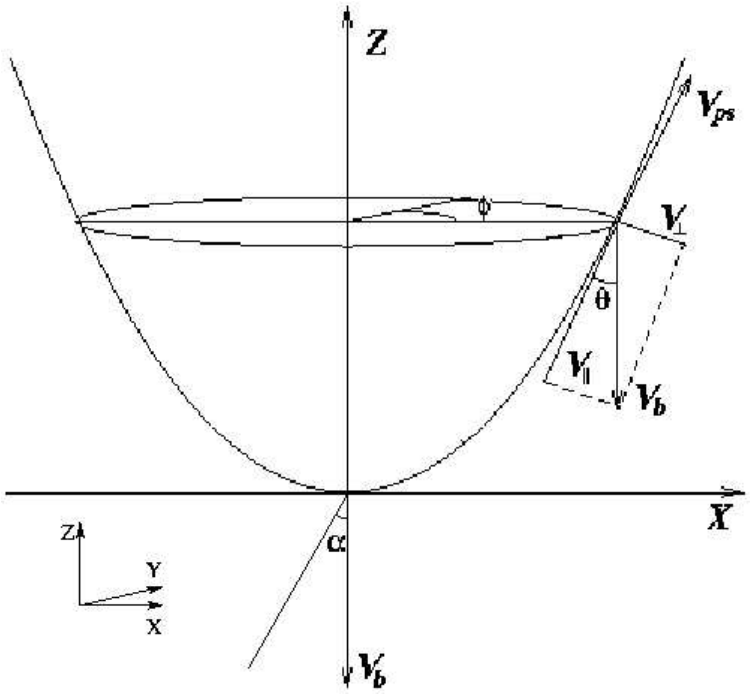

Figure 2.8: Parabolic bow shock geometry.

described by a parabolic surface where the apex coincides with the origin of the coordinate system,

$$z = \frac{R^2}{2b} \tag{2.23}$$

where $R = \sqrt{x^2 + y^2}$ is the radius at the distance z along the longitudinal axis of the bow and b is the shape parameter of the parabolic surface. Moreover we define ϕ as the azimuthal angle around the $z-$axis. The $x - y$ plane is tangent to the apex of the paraboloid, while the line of sight lies in the $x - z$ plane, forming an angle α with the $z-$axis.

We assume the bow to be moving through a stationary medium with a velocity V_b along the negative direction of the $z-$axis, which represents the central axis of the surface. In each point of the bow surface, an angle θ is defined as the angle between the direction in which the bow is moving and the tangent to the surface in that point.
In the reference system of the shock front, the ambient medium flows toward the bow as a wind that impacts the surface with a velocity V_w (V_w is directed on the $+z-$direction); at the bow surface, V_w is resolved into normal and tangential components to the bow, that are $V_\perp = -V_w \sin\theta$ and $V_\parallel = -V_w \cos\theta$, respectively. The component $V_\perp$ represents the shock velocity (V_s) at the considered point and, according to the model of strong shocks, the value of the expected post-shock velocity is $\sim 1/40$ of the shock velocity, since it decreases taking into account both the jump conditions for a strong shock (a factor 4) and the effect of cooling for an isothermal shock (a factor 10) (see Section 2.1.2). As a consequence, we can assume that the post-shock velocity in the direction normal to the surface (i.e. the shock velocity direction) is negligible and that the entire post-shocked gas moves tangentially to the bow surface.
The radial velocity of the shocked emitting gas (V_r) is therefore the component of $V_\parallel$ along the line of sight. The unit vectors along the line of sight ($\hat{a}$) and along the direction tangential to the bow surface ($\hat{t}$) are expressed in cylindrical coordinates:

$$\hat{a} = \sin\alpha\,\hat{i} + \cos\alpha\,\hat{k} \tag{2.24}$$

$$\hat{t} = \sin\theta\,\cos\phi\,\hat{i} + \sin\theta\,\sin\phi\,\hat{j} + \cos\theta\,\hat{k} \tag{2.25}$$

where $\hat{i}, \hat{j}, \hat{k}$ are the unit vectors in the direction of the $x-, y-, z-$axes respectively.
Then, the observed radial velocity is:

$$\begin{aligned} V_r &= -V_w \cos\theta\,\hat{t}\cdot\,\hat{a} \\ &= -V_w \cos\theta\,(\sin\alpha\,\sin\theta\,\cos\phi + \cos\alpha\,\cos\theta) \end{aligned} \tag{2.26}$$

This Equation is obtained for the case of a bow inside a moving medium. If instead the bow is moving through a medium at rest, Equation 2.26 involves simply a change of the reference frame, i.e. the speed of the bow along the line of

sight must be added:

$$\begin{aligned} V_r &= -V_w \cos\theta\, \hat{t} \cdot\ \hat{a} + V_b \cdot\ \hat{a} \\ &= V_b \cos\theta\, (\sin\alpha\ \sin\theta\ \cos\phi + \cos\alpha\ \cos\theta) - V_b \cos\alpha \end{aligned} \tag{2.27}$$

where $V_b = -V_w \hat{k}$, because the bow is travelling in the $-z-$direction.
Now we consider how to determine the expressions for the maximum and the minimum observed radial velocities. This is a very important aspect because it allows us to estimate the bow velocity from a direct measure of an observed spectral line profile (Hartigan et al. 1987).
First, we notice that the maximum and the minimum observed radial velocities occur when $\phi = 0, \pi$, i. e. when $V_\parallel$ lies on the $x - y$ plane, which represents the plane where the angle α is defined. Thus, from Equation 2.27, we can write the radial velocity of the emitting gas in the $x - z$ plane:

$$V_r = V_b \cos\theta\, (\cos\alpha\ \cos\theta \pm \sin\alpha\ \sin\theta) - V_b \cos\alpha \tag{2.28}$$

where the + and - signs refer to the two sides of the curve, where the maximum and minimum radial velocities lie, respectively. Setting $\partial V_r / \partial\theta = 0$ we obtain the maximum and the minimum observed radial velocities, which occur when $\theta_M = \alpha/2$ and $\theta_m = \pi/2 - \alpha/2$ respectively (Hartigan et al. 1987).
It is important to notice that the axial symmetry of the bow surface means that the radial velocities of each expanding ring simply change sign when they are seen with an angle $180° - \alpha$: this implies that the meaning of $\pm$ determinations in Equation 2.28 are inverted if $\alpha > 90°$.
Substituting θ_M and θ_m values into Equation 2.28, we find the maximum and the minimum radial velocities,

$$\begin{aligned} V_{rM} &= \frac{V_b}{2}[1 + \cos\alpha] - V_b \cos\alpha \\ V_{rm} &= -\frac{V_b}{2}[1 - \cos\alpha] - V_b \cos\alpha \end{aligned} \tag{2.29}$$

and, from these equations, we notice that:

$$FWZI = V_{rM} - V_{rm} = V_b \tag{2.30}$$

This means that the observed spectral profile of a line emitting over the entire bow shock has the Full Width at Zero Intensity (FWZI) equal to the bow speed, which is the shock velocity at the apex of the bow. For example, in the NIR, [Fe II]

line profiles are very suitable to perform this measure, since [Fe II] emit from the bow head to certain regions of the bow flanks (where the excitation conditions for [Fe II] emissions still occur).

This measure is independent of the orientation angle and of most uncertain parameters of the shock models. Moreover, having V_b, a direct measure of the angle α can be performed using Equations 2.29; however, since Equations 2.29 determine the cosine of α, this estimate is accurate just when $\alpha \approx 90°$, while for oblique flows ($0° < \alpha < 45°$, $135° < \alpha < 180°$) the measure is not accurate because V_{rM} or V_{rm} have near zero radial velocity values.

In the front region of the bow surface, the component of the bow velocity normal to the shock surface (i.e. the shock velocity in that point), may exceed a critical shock velocity V_{dis}, which represents the velocity at which H_2 is dissociated. If this is the case, the molecular hydrogen emits over the bow wings but does not emit over the bow cap, which represents a dissociation cap where emission from atomic elements occurs. Therefore, it is possible to define as z_{dis} the position along the $z-$axis where the plane including the "beginning" of the dissociation cap is located; certainly it depends on V_b, V_{dis} and on the shape of the bow surface. Setting $V_{dis} = V_b \sin\theta_{dis}$ and, considering that for a generic angle θ, $\tan\theta = dR/dz$ is,

$$V_{dis} \;=\; V_b \sin\left(\arctan\frac{dR}{dz}\right)\Bigg|_{z=z_{dis}} \tag{2.31}$$

and assuming the parabolic bow shape defined by Equation 2.8,

$$V_{dis} = V_b \frac{\sqrt{b/2z}}{\sqrt{1+b/2z}}\Bigg|_{z=z_{dis}} \tag{2.32}$$

thus, z_{dis} can be expressed in the explicit form:

$$z_{dis} = \frac{b}{2}\left[\left(\frac{V_b}{V_{dis}}\right)^2 - 1\right] \tag{2.33}$$

The determination of V_{dis} has been widely discussed over the last decades: a first value of 24 km s^{-1} was inferred by Kwan (1977), subsequently Draine et al. (1983) hypothesized $V_{dis} = 50$ km s^{-1}, a result confirmed by Smith & Brand (1990) . More recently, Le Bourlot et al. (2002) showed that V_{dis} can increase up to 80 km s^{-1} for low values of the pre-shock density (see Figure 2.9).

The bow shape can be determined using H_2 emission line maps by a direct measurement of the radius of the last emitting ring R_{dis}, below which the molecular

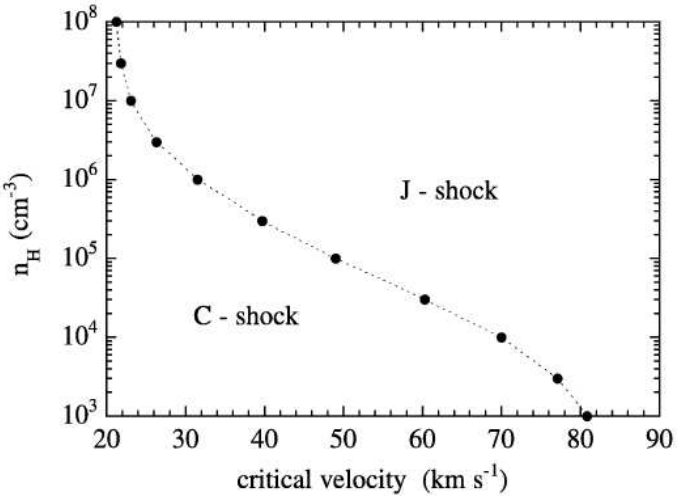

Figure 2.9: Maximun shock speed (critical velocity) consistent with the existence of a C-type shock, as a function of the pre-shock gas density (Le Bourlot et al. 2002).

gas is no longer excited (see Figure 2.10). Indeed, assuming the usual parabolic surface and using Equations 2.23 and 2.33, b is:

$$b = \frac{R_{dis}}{\sqrt{\left(\frac{V_b}{V_{dis}}\right)^2 - 1}} \tag{2.34}$$

where V_b can be estimated using atomic lines spectra (Equation 2.30) and V_{dis} must be assumed theoretically.

Several models have been developed to interpret the H_2 emission arising from the bow shock surface. Smith (1991) discusses how to simulate emission line maps of molecular hydrogen using a model in which a C-shock generates the H_2 emission. In this model, he considers the H_2 line 1-0 S(1) at 2.12 μm and he sets $V_{dis} = 47$ km s^{-1}, a b parameter of 2 for the bow shape (see Equation 2.23), a medium with H_2 density equal to 10^6 cm^{-3}, a uniform magnetic field $B = 10^{-3}$ G and a fractional ionization of 10^{-7}.

Figure 2.10 shows the derived H_2 intensity distribution obtained by Smith (1991) for a bow moving in a quiescent molecular gas. In the upper panel, the intensity of a bow moving in the plane of the sky ($\alpha = 90°$), is displayed for three different bow speed values; it demonstrates how, with an increase in the bow velocity, the H_2 emission is displaced progressively away from the front.

In the lower panels in Figure 2.10, the emission of a 120 km s^{-1} moving bow is displayed, as seen from different α angles. These panels show how the dissociation cap, which is seen as a truncation of the bow surface at $\alpha \sim 90°$, appears as a projected hole when the bow is observed from oblique angles ($15° < \theta < 60°$).

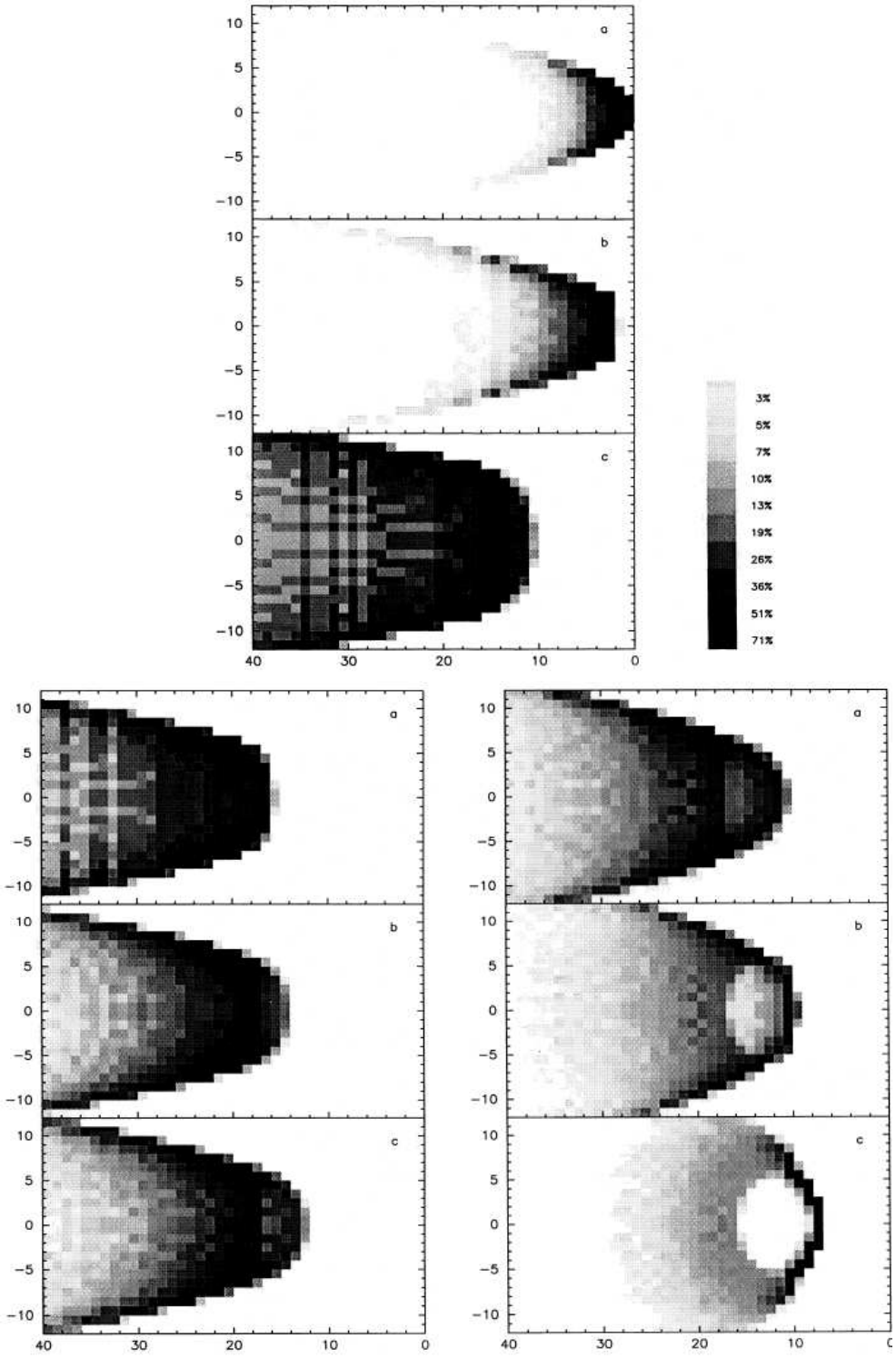

Figure 2.10: Intensity map of molecular hydrogen emission. In the upper panel, intensity distribution for a bow moving in the plane of the sky as a function of different bow speeds V_b: 60 km s^{-1} (a), 80 km s^{-1} (b) and 160 km s^{-1} (c). In the lower panels, intensity distribution of a 120 km s^{-1} bow shock as a function of the inclination angle α: 90° (a), 75° (b), 60° (c) in the left panel and 45° (a), 30° (b), 15° (c) in the right panel. The bow apex has been shifted to the position (10,0) (Smith 1991).

Moreover, at these orientations, the tail of the emission tends to disappear and to be replaced by a diffuse region and the H_2 emission can occur from ahead of the apex. Furthermore, as the angle α tends to zero, the projection of the H_2 emission becomes narrower, since it is delimited by the region derived by the projection of the dissociation cap and the region where the molecular gas is no longer excited. Now we want to show how molecular hydrogen line profiles should appear according to a parabolic bow shape model.

This analysis was performed by Schultz et al. (2005) and the results are displayed in Figure 2.11; here H_2 line profiles, generated from a bow shock approaching to the observer, are illustrated varying the viewing angle α and the cooling function p (see below); the flux is normalized to the peak intensity and the velocity is normalized to the bow velocity V_b (in these cases 50 and 100 km s^{-1}). The cooling function index p measures how much of the kinetic energy of the shock is transferred to the excitation of a molecular transition, according to the formula:

$$I \propto V_s^p = V_b^p \sin^p \theta \tag{2.35}$$

The parameter p describes the physics of the shocks, indicating the amount of shock energy that is restored in a molecular transition and then it represents the shock cooling mechanism. In particular, p has an upper limit of 3 in the case that all the shock energy is transferred into excitation.

The effect on the line profile of increasing the cooling function index (see Figure 2.11) is to increase the relative contribution from the regions near the apex of the bow, since the intensity increases as $\sin^p \theta$ (see Equation 2.35). Thus, as p increases, there is an increase in the strength of the blue wing of the line profile, because the bluest emission (except for the case of $\alpha \sim 90°$) comes from the region where the strongest shocks occur (that is the bow head). Moreover the line profiles reported in Figure 2.11 depend on the α angle; the profile exhibits a peak of the blue emission at a velocity -V_b when the bow is viewed head-on ($\alpha = 0°$), and this peak moves towards zero velocity with the increase of α, up to the point where the bow is viewed from the side ($\alpha = 90°$), when the profile is symmetrical about at $V = 0$ (as long there is no extinction, see caption of Figure 2.11).

It is important to highlight that the behaviour of line profiles reported in Figure 2.11, i.e. an overall line symmetry except for some excess for the blue wings, are typical for the parabolic model; other bow shapes (e.g. cubic or other function, see Schultz et al. (2005)) change the line profiles dramatically, especially resulting in more asymmetric profiles.

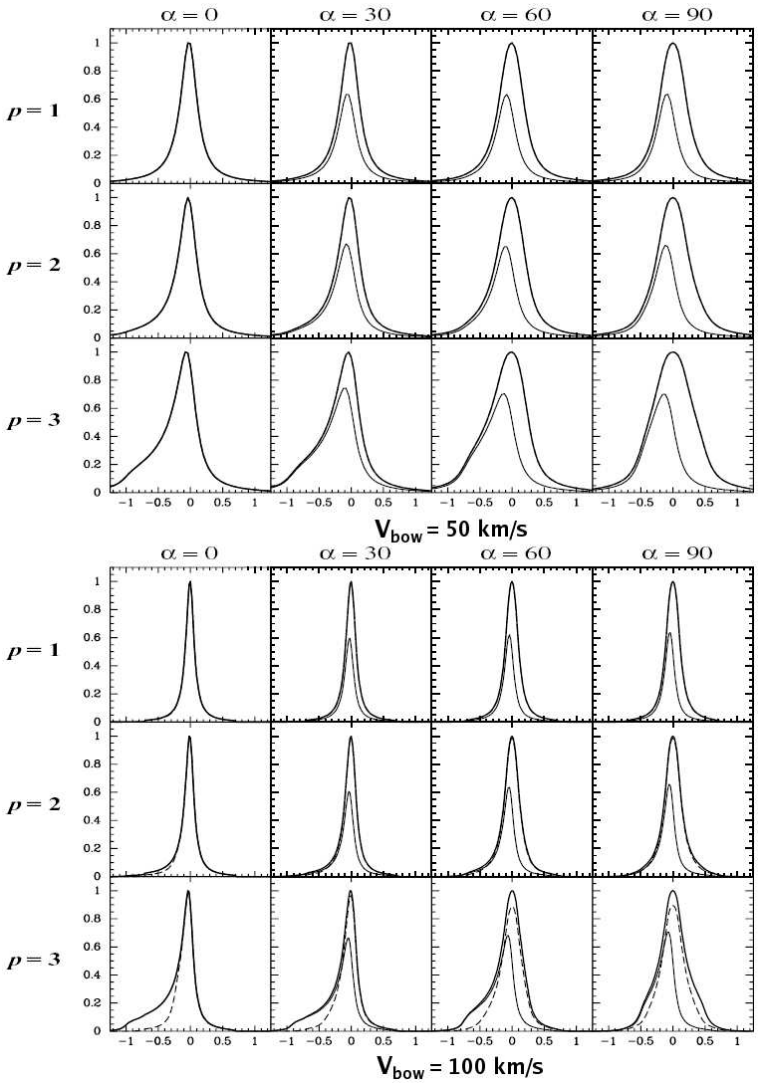

Figure 2.11: Profiles of H_2 lines according to a parabolic bow shape model as they appear when changing the viewing angle α and the cooling function index p, for two values of the bow velocity (V_{bow} = 50 km s^{-1}, upper panel, and V_{bow} = 100 km s^{-1}, lower panel). Heavy solid line represents a model with no extinction and no dissociation occur for the molecular hydrogen, light solid line denotes that extinction occurs but no dissociation, and dashed line indicates that dissociation occurs with V_{dis} = 50 km s^{-1} but with no extinction. The extinction hypothesis assumes that dust within the hollow bow completely blocks emission from gas not directly visible to the observer, resulting in a lack of red emission as the bow is viewed from the side. The introduction of V_{dis} = 50 km s^{-1}, which evidently does not effect the case with V_{bow} = 50 km s^{-1}, involves the suppression of blue emission when the bow is observed with $\alpha < 90°$, while both red and blue wings are suppressed when $\alpha = 90°$ (Schultz et al. 2005).

2.2.1 Kinematic analysis of emission lines

Spectroscopy of bright atomic and molecular lines (e.g. [Fe II] at 1.64 μm and H_2 at 2.12 μm) allows us to study the kinematics of HH objects. This can be performed by measuring the flow radial velocity which is the peak of the line profile. This measure allows to:
(i) understand if the observed object belongs to the receding (red) or approaching (blue) lobe of the outflow,
(ii) discriminate radial velocity variations (accelerations or decelerations) along the jet axis,
(iii) combining the radial velocity with the tangential velocity, the latter obtainable by measurements of the distance covered by the shock using images taken between two different epochs. This combination enables to derive the total object velocity through the cloud, along with the inclination angle with respect to the line of sight (Caratti o Garatti et al. 2007).
If the observed transition has no dispersion along the wavelength dimension (i.e. it is a Dirac function) and is located at the wavelength λ_{peak}, the object's radial velocity measured by the observer (v_{obs}) can be expressed with the Doppler formula:

$$v_{obs} = \frac{\lambda_{peak} - \lambda_0}{\lambda_0} \cdot c \tag{2.36}$$

where λ_0 is the vacuum wavelength of the transition and c is the light speed ($c \simeq 3 \cdot 10^5$ km s^{-1}) .
In fact, a more interesting measure is the object's velocity with respect to the parent cloud within which the flow is moving (which approximately coincides with the motion of the exciting source); to achieve this, since the cloud velocities v_{cloud} provided in literature are generally measured with respect to the Local Standard of Rest (LSR), it is necessary to express v_{obs} in this reference system. The correction term v_{corr}, which provides the observer velocity with respect to LSR, can be obtained by taking into account the rotation of the Earth, the motion of Earth-Moon system and the Sun with respect to the LSR system[1]. Thus, the observed velocity v_{LSR} with respect to the LSR is:

$$v_{LSR} = v_{obs} + v_{corr} \tag{2.37}$$

[1] v_{corr} can be accomplished, for example, with the task *rvcorrect* of the astronomical analysis package IRAF (Image Reduction and Analysis Facility), distributed by NOAO (National Optical Astronomy Observatories).

and, finally, the velocity of the object with respect to the local cloud becomes:

$$v_{obj} = v_{LRS} - v_{cloud} \tag{2.38}$$

The turbulence generated by the impact between the outflow and the interstellar medium produces a distribution of velocity associated with the transition; the measure of the FWHM of the line profile provides the velocity dispersion Δv associated with these internal motions.
The measurement of the FWHM depends on the spectral resolution of the observations ($R = \lambda/\Delta\lambda$), which generates an instrumental broadening of the observed line. Generally speaking, the observed FWHM (FWHM_{obs}) is a convolution of the intrinsic line width (FWHM_{int}) and the instrumental profile (FWHM_{str}). If both these lines are Gaussian, it follows that:

$$FWHM^2_{obs} = FWHM^2_{int} + FWHM^2_{str} \tag{2.39}$$

Thus the FWHM_{int} is obtained performing the de-convolution,

$$FWHM_{int} = \sqrt{FWHM^2_{obs} - FWHM^2_{str}} \tag{2.40}$$

where FWHM_{str} is linked to the spectrograph resolution power at the wavelength λ by the relation:

$$FWHM_{str} \equiv \Delta\lambda = \frac{\lambda}{R} \tag{2.41}$$

Generally the nominal resolution of the spectrograph does not coincide with the real resolution that may be found on the spectral image. The latter can be estimated by a FWHM measure of atmospheric OH lines (see Section **??**), which are abundant in the NIR bands and are not resolved (being few km s^{-1} wide) at the highest resolutions achieved by modern infrared spectrographs ($\mathrm{R} \leq 40\,000$).

Position-Velocity diagrams

The *Position-Velocity (P-V) diagrams* represent a very interesting tool to study the kinematics of the atomic and molecular constituents of the shocked gas.
Figure 2.12 shows two synthetic P-V diagrams of the H_2 line at 2.12 μm(Davis et al. 1999); the central and right panels display the spectral behaviour (expressed in velocity units) of the line emission selected with the two vertical slits indicated on the left panel, which represents an image of the 2.12μm line emission generated from a C-type shock on a bow-shape surface. This example shows how the val-

ues of the peak velocity and the velocity dispersion can be significantly different observing different emitting regions of the bow shock.

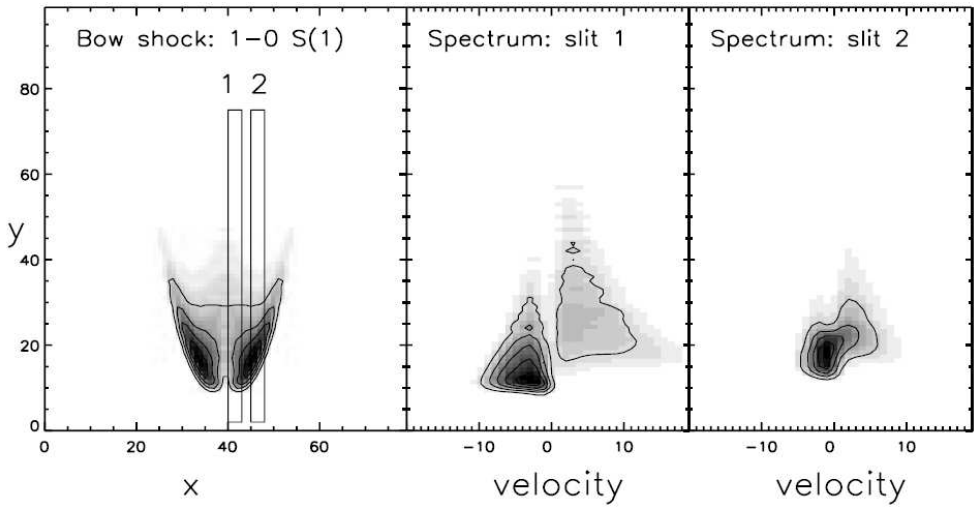

Figure 2.12: Synthetic P-V diagrams: on the image of H_2 emission at 2.12 μm generated by a C-type bow shock (left panel), two vertical slits select the regions for those two P-V diagrams (central and right panel) are generated. The reported velocity unit are km s^{-1} (Davis et al. 1999).

2.3 Physical parameters from near-infrared observations

2.3.1 Near-infrared lines

Figure 2.13 represents an example of a NIR (1-2.5 μm) spectrum of a HH object. The spectrum is dominated by H_2 and forbidden [Fe II] lines and other observed atomic lines are [CI], [SII], [SIII], [PII], [TiII], [NI][2] and atomic hydrogen lines). This is a general result occurring in HH objects that suggests that H_2 and [Fe II] lines are well suited to probe the physical processes occurring in HH objects.

H_2 roto-vibrational lines

The molecular hydrogen is the chief constituent of the molecular cloud. It is the simplest molecule which can be formed, since it consists of two electrons and two

[2]The forbidden lines, which are represented with the square brackets, are those having zero electric dipole momentum and are therefore generated from electric quadrupole or magnetic dipole momentum.

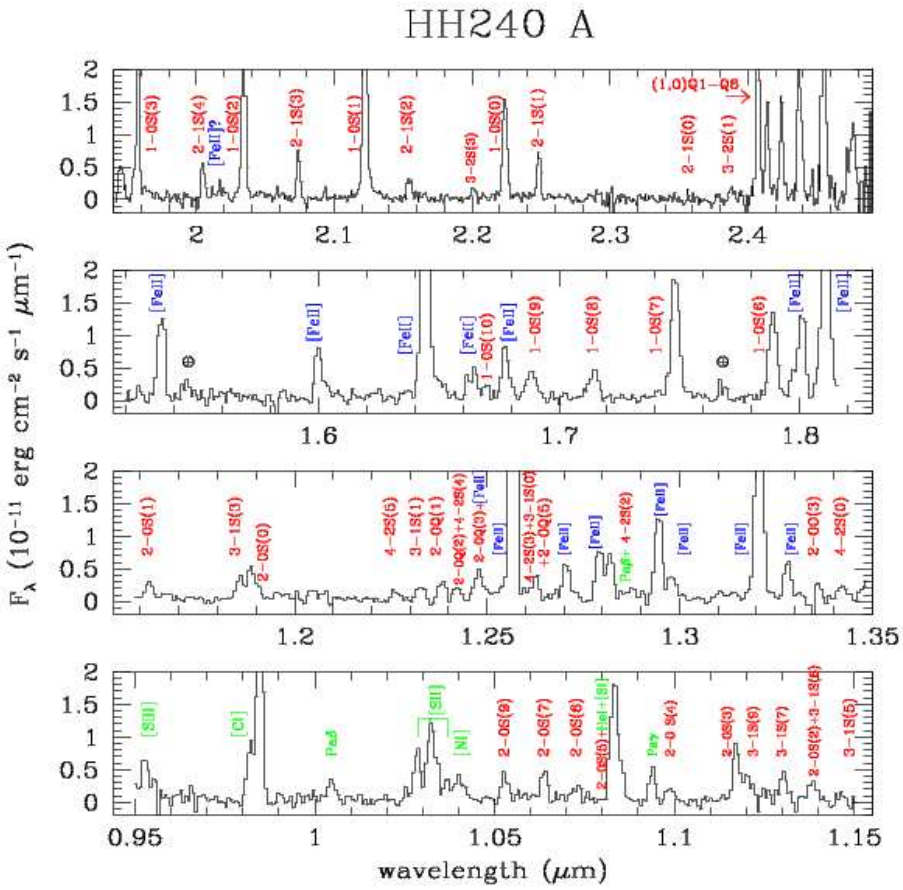

Figure 2.13: Near-infrared spectrum of the object HH240A collected with the SofI spectrometer at the NTT telescope. The prevalence of H_2 lines (red) is evident while, for the atomic transitions, the most abundant features are [Fe II] lines (blue) compared with the others (green) (Nisini et al. 2002).

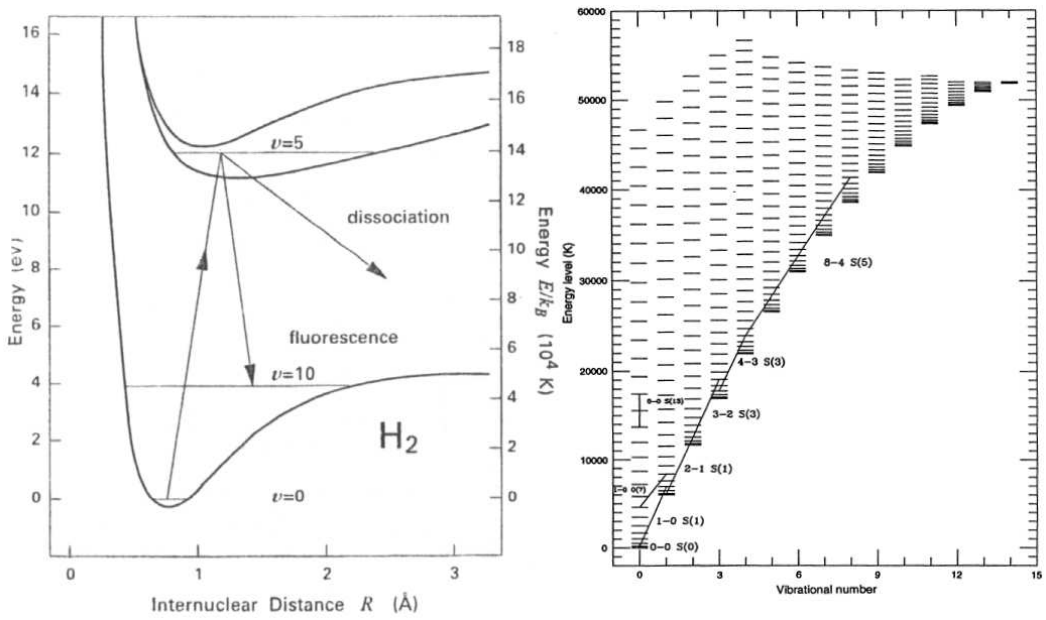

Figure 2.14: Left figure: potential energy (reported with two different scales) of molecular hydrogen as a function of internuclear distance. The three curves correspond to the ground and to the first two excited electronic states, while the horizontal lines represent vibrational levels. The arrows describe the photo-excitation, followed by fluorescent decay or dissociation. Right figure: H_2 energy levels for the electronic ground state. Some H_2 transitions are reported (Burton 1992).

protons bound in a covalent bond. Moreover atomic hydrogen is absolutely the most abundant element in the interstellar medium, being about 10^4 times more abundant with respect to other elements. Nevertheless, H_2 is difficult to detect in the cold molecular cloud; the lowest excited energy level has an associated excitation energy of 510 K, which is quite far above the temperature of the quiescent molecular gas.

This is due to the simplicity and symmetry of the molecular hydrogen. The energetic structure of H_2 is formed by rotational, vibrational and electronic levels, thus the total energy is the sum of these contributions;

$$E = E_{rot} + E_{vib} + E_{elect} \tag{2.42}$$

where,

$$E_{rot} = \frac{\hbar^2}{2I} J(J+1) \tag{2.43}$$

$$E_{vib} = \hbar\omega_0(v + 1/2) \tag{2.44}$$

J is the rotational quantum number, I is the moment of inertia, v is the vibrational quantum number and $\omega_0 = 2\pi\nu_0$, where ν_0 is the fundamental vibrational

frequency.
Figure 2.14 shows a schematic view of the energetic structure of molecular hydrogen, with a particular of the levels belonging to the ground state.
The momentum of inertia of H_2 is the smallest of any diatomic molecule, so Equation 2.43 shows that the energy levels are widely spread out. The ground electronic state has 14 vibrational levels and a continuum level above the binding energy, that is 4.48 eV, which corresponds to a kinetic energy of $\sim$ 24 km s^{-1} (Kwan 1977).
H_2 is mainly excited either by absorption of UV radiation or by collisions between H_2 molecules, H atoms and electrons; the first process pumps the H_2 into its electronic excited states and it is followed by optical and IR fluorescence emission, while the second populates the ro-vibrational levels of the electronic ground state. The latter is most typically found in shocks and it is the main excitation mechanism observed in jets and HH objects.
The selection rules for H_2 transition are regulated by its homopolar nature; it does not have a permanent dipole and it can radiate only through electric quadrupole transitions since it has a permanent quadrupole moment. Consequently, transitions between different J-states are allowed only if $\Delta J = 0, \pm 2$, with the transition $J(0 \rightarrow 0)$ being forbidden, but there are no restrictions imposed on the v quantum number.
Generally the ro-vibrational transitions are designated as $v_{in} - v_{fin} A(J_{fin})$, where v_{in} and v_{fin} denote the initial and final vibrational state and A is the rotational quantum gap, denoted by S, Q, O for $J_{fin} - J_{in} = -2, 0, 2$, respectively.
The H_2 transitions observed in the NIR have a large spread in energy excitation (from $\sim$ 6 000 K to $\sim$ 40 000 K) allowing to trace the gas temperature and the excitation conditions over a wide range of energies.
The most important H_2 transition observed in the NIR bands is the 1-0S(1) line at 2.12 μm (transition from v=1 and v=0 and from J=3 and J=1). It is among the brightest H_2 lines (its luminosity represents 10% of the luminosity of the entire H_2 lines) and it is located in the middle of the K band, where good conditions of atmospheric trasmission are reached (see Figure **??**). Because of its high luminosity, the 1-0S(1) line is used in imaging to find jet emissions, bow shocks and, generally, shock regions in a molecular ambient where H_2 is excited. For this purpose, an image acquired in the K band is subtracted from an image acquired in the narrow band built around the 2.12 μm wavelength (H_2 filter): in this way the regions of interaction between protostellar outflow and ambient cloud will be pointed out (see Figure 2.15).

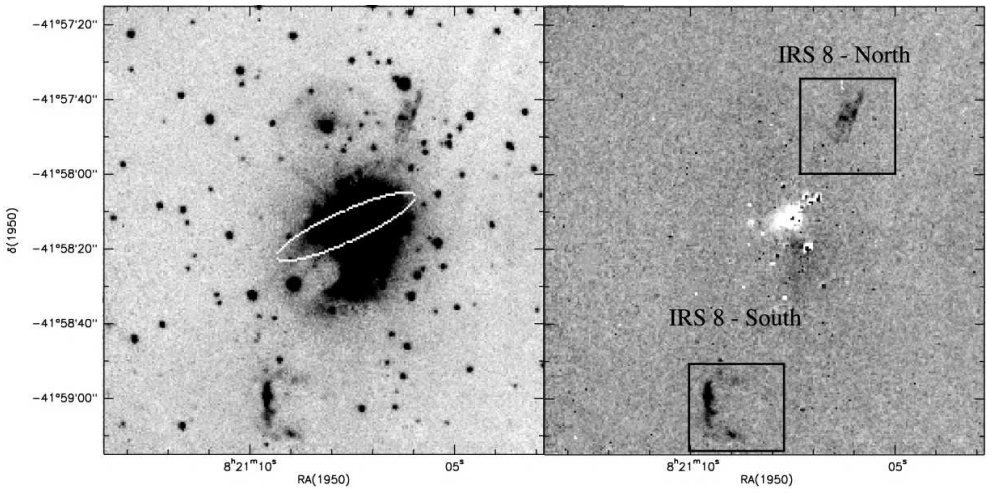

Figure 2.15: The left image shows the field of the YSO IRS8 acquired with a narrow band filter at 2.12 μm; the ellipse indicates the uncertainty position of the source identified with IRAS (InfraRed Astronomical Satellite). On the right, the H_2 - K image of the same field is shown. The continuum subtracted image evidences just the two lobes of the outflow (indicated into square boxes) traced by H_2 emission (Lorenzetti et al. 2002).

[Fe II] lines

In cold molecular clouds, iron is usually strongly depleted into dust grains and thus its gas-phase abundance is extremely low. The violent shocks generated in HH objects can destroy all or part of the dust grains, allowing the release of Fe in gas-phase into the interstellar medium where, because of its low ionization potential (7.9 eV), is usually observed in single ionized form. [Fe II] lines are found in a large wavelength range, from UV to middle-IR. In particular, the brightest lines observed in the NIR bands are those connecting the fine structure levels of the ^{4}D term with the levels of the ^{4}F and ^{6}D terms (see Figure 2.16); for this reason most of the observed lines have very similar excitation energies, raging from $\sim$ 11 000 K to $\sim$ 13 000 K.

Table 2.1 reports the main parameters for the bright forbidden [Fe II] lines observed in the NIR spectral range, such as the spectroscopic nomenclature, the vacuum wavelength, the energy for the upper level and the critical density (see below).

2.3.2 Collisionally excited lines: LTE and NLTE approximations

Under shock conditions, atomic and molecular lines are emitted due to the radiative decay of collisionally excited energy levels. Here we want to describe how the line intensity depends on the main physical parameters involved in this process.

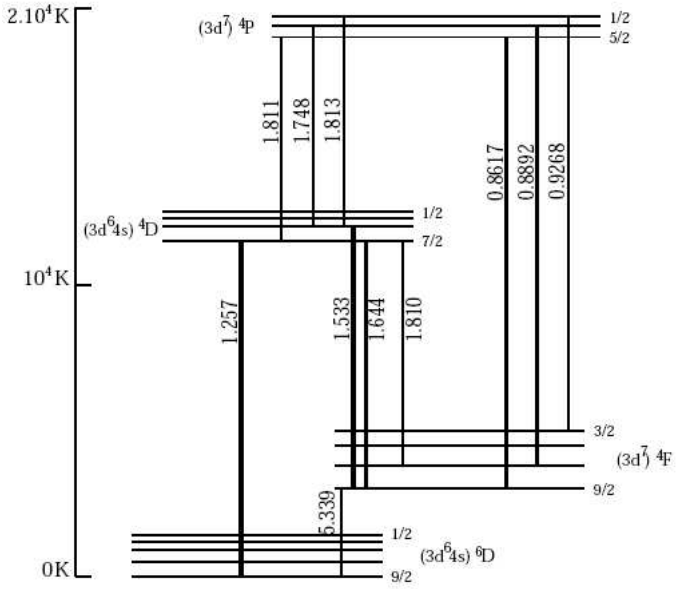

Figure 2.16: [Fe II] energy levels. The most prominent lines originate from the fine structure levels of ^4D term.

Table 2.1: Most important bright [Fe II] lines in NIR spectral range.

Transition	λ (μm)	E_{up} (K)	n_{cr} (cm^{-3})
$a^4D_{7/2}-a^6D_{9/2}$	1.257	11446	7.2 10^4
$a^4D_{7/2}-a^6D_{7/2}$	1.321	11446	7.2 10^4
$a^4D_{7/2}-a^4F_{9/2}$	1.644	11446	7.2 10^4
$a^4D_{5/2}-a^4F_{9/2}$	1.534	12074	5.5 10^4
$a^4D_{5/2}-a^4F_{7/2}$	1.677	12074	5.5 10^4
$a^4D_{3/2}-a^4F_{7/2}$	1.600	12489	4.3 10^4

Let us consider a transition from the upper level i to the lower level j of an atomic or molecular species, being n_i and n_j the respective number densities (cm^{-3}), A_{ij} and ν_{ij} the Einstein coefficients for spontaneous emission (s^{-1}) and the transition frequency (s^{-1}), respectively. The variation of intensity occurring when the radiation passes through a path length ds (*Equation of Radiative Transfer*) can be writte as:

$$\frac{dI}{ds} = -k\,I + \epsilon_{ij} \tag{2.45}$$

In the right side of Equation 2.45 there are the contributions of both the processes (emission and absorption) which concur to the intensity variation: k is the *opacity* of the medium along the considered path, while ϵ_{ij} is the *emission coefficient* for the transition $i \rightarrow j$ and it is defined as the energy emitted by the gas per unit volume, per second, per steradiant (erg s^{-1} cm^{-3} sr^{-1}),

$$\epsilon_{ij} = \frac{n_i A_{ij} h\nu_{ij}}{4\pi} \tag{2.46}$$

The A_{ij} coefficient values of forbidden lines, such as those observed in nebular ambients, are very small (lower then a factor $\sim 10^5$ for the magnetic dipole and a factor $\sim 10^8$ for electric quadrupole transitions compared to permitted lines); since the absorption coefficient k depends linearly on A_{ij} (Genzel 1991), the opacity is usually very low for these lines, thus we can ignore the k term in Equation 2.45 and assume that they are *optically thin* lines.
Thus the observed intensity of an optically thin line is:

$$\begin{aligned} I_{ij} &= \int \epsilon_{ij} ds \\ &= \frac{h\nu_{ij}}{4\pi} A_{ij} \int n_i ds \\ &= \frac{h\nu_{ij}}{4\pi} A_{ij} \int f_i n ds \end{aligned} \tag{2.47}$$

where the integration is taken along the line of sight and we have introduced the fractional population of the i level $f_i = n_i/n$ (n is the particle density of the emitting species). In such an Equation, the critical quantity to be determined is the fractional population f_i.
For optically thin lines and assuming the contribution from an external radiating field to be negligible, as occurs in interstellar shock enviroments where only collisional excitation occurs, the fractional population of the different levels can be computed from the *Statistical Equilibrium Equations* in which only collisional

excitation and de-excitation are considered.
These can be written as:

$$\sum_{j\neq i}^{N} n_j n_0 \gamma_{j,i} + \sum_{j>i}^{N} n_j A_{j,i} = n_i \left(\sum_{j\neq i}^{N} n_0 \gamma_{i,j} + \sum_{j<i}^{N} A_{i,j} \right) \tag{2.48}$$

where n_0 is the number density (cm^{-3}) of the collision partners (electrons, hydrogen atoms and molecules), $\gamma_{i,j}$ are the collisional excitation and de-extitation rate coefficients ($\mathrm{cm}^3\ \mathrm{s}^{-1}$) and, finally, the sum is taken over the N levels that are populated.
Each one of Equations 2.48 describes the equilibrium between the rates that populate (left side of Equation) and the rates that de-populate (right side of Equation) the i level. The $\gamma_{i,j}$ coefficients represent the average of the product between the collisional cross section for a collision $i \rightarrow j$ at velocity v and the velocity v ($< \sigma_{i,j} v >$). The average is taken over all the possible collision energies weighted by a distribution function that is assumed to be a Maxwell-Boltzmann distribution at kinetic temperature T (Genzel 1991);

$$\gamma_{ij} = \langle \sigma_{ij} v \rangle = \frac{4}{\sqrt{\pi}} \left(\frac{\mu}{2kT} \right)^{\frac{3}{2}} \int_0^{+\infty} dv \left(\sigma_{ij}(v)\, v \right) v^2 e^{-\mu v^2/2kT} \tag{2.49}$$

where μ is the reduced mass of the collision partners .
As a consequence, the dependence on the temperature of Equations 2.48 is implicit in the $\gamma_{i,j}$ coefficients.
Moreover, the excitation coefficients $\gamma_{i,j}$ are linked with the de-excitation coefficients $\gamma_{j,i}$ by the relation:

$$\gamma_{j,i} = \gamma_{i,j}\, g_i / g_j e^{-h\nu/kT} \tag{2.50}$$

where g_i is the degeneracy of the i level.
In conclusion, Equations 2.48 give the density population of a level as a function of the local values of T and n_0, therefore they are referred as *Non Local Thermal Equilibrium* (NLTE) conditions.
From Equations 2.48 we can see that collisional de-excitation dominates over radiative de-excitation when:

$$\sum_{j\neq i}^{N} n_0 \gamma_{i,j} > \sum_{j<i}^{N} A_{i,j} \tag{2.51}$$

that is,

$$n_0 > n_{cr} = \frac{\sum_{j<i}^{N} A_{i,j}}{\sum_{j\neq i}^{N} \gamma_{i,j}} \tag{2.52}$$

Equation 2.52 defines the *critical density* which is a very important parameter defining a threshold density for n_0 that influences the diagnostic capability of a line.
To better highlight this aspect, let us consider a two level system (Genzel 1991). In that case, Equations 2.48 simply become:

$$n_j(\gamma_{ji} n_0) = n_i(\gamma_{ij} + A_{ij}) \tag{2.53}$$

or, using Equation 2.50,

$$\frac{n_i}{n_i + n_j} = \frac{g_i/g_j e^{-h\nu/kT}}{1 + g_i/g_j e^{-h\nu/kT} + n_{cr}/n_0} \tag{2.54}$$

If the density is much larger than the critical density of a given level ($n_0 \gg n_{cr}$), Equation 2.54 becomes:

$$\frac{n_i}{n_j} = \frac{g_i}{g_j} e^{-h\nu_{ij}/kT} \tag{2.55}$$

Thus the levels are populated according to the Boltzmann distribution, which represents a thermalized distribution at the kinetic temperature T. This condition defines the *Local Thermal Equilibrium* (LTE) limit.
Using Equation 2.55, the fractional population f_i in LTE conditions is

$$f_i = \frac{n_i}{n} = \frac{g_i e^{-E_i/kT}}{\sum_j g_j e^{-E_j/kT}} = \frac{g_i e^{-E_i/kT}}{Q} \tag{2.56}$$

where E_i is the excitation energy of the i level and Q is called the *partition function.*
In the LTE limit the fractional population depends only on the local temperature values, then it is no longer dependent on the path length; as a consequence the observed line intensity (see Equation 2.47) becomes:

$$I_{ij} = \frac{h\nu_{ij}}{4\pi} A_{ij} f_i \int n ds \propto N \tag{2.57}$$

In this limit, the line intensity is proportional only to the column density $N = \int nds$.
Otherwise, if the density is lower than the critical density, collisional de-excitations are negligible and the level population is sub-thermal. Equation 2.54 becomes:

$$\frac{n_i}{n_j} = \left[\frac{n_i}{n_j}\right]_{therm} \frac{n_0}{n_{cr}} \tag{2.58}$$

that involves a different expression for f_i:

$$f_i = [f_i]_{therm} \frac{n_0}{n_{cr}} \tag{2.59}$$

In the sub-thermal limit, the observed line intensity is:

$$I_{ij} \propto \int n n_0 ds \propto N n_0 \tag{2.60}$$

and it is dependent on both the column density and the colliders density.
A consequence of the introduction of the critical density is that, for a given T value, the line intensity of a gas is a linear function of n_0 till the considered gas is in a sub-thermal condition ($n_0 < n_{cr}$, see Equation 2.60) and it reaches a constant value when n_0 exceeds the value of the gas critical density, no longer being dependent on the colliders density variations (see Equation 2.57); an example is reported in Figure 2.17, where the emissivity of the [Fe II] transition at 1.25 μm ($n_{cr} = 7 \cdot 10^4$) is reported as a function of the collider (electron) density. Thus, if we consider two lines of the same species with similar excitation energy (i.e. the relative population of emitting levels is not affected by temperature variations), but with different critical densities, the ratio of these lines is sensitive to gas density variations while it is poorly sensitive to temperature variations. The considered ratio is more sensitive to density variations as the difference between critical density values grows.
On the contrary, the ratio of two lines originated from levels with different excitation energies probes the gas temperature, since the populations of the upper levels depend on the efficiency of the collisional rates, which are a function of the kinetic temperature. In this case, the line ratios are predicted by NLTE models which solve the Equations of Detailed Balance 2.48 once the atomic parameters (i.e. spontaneous rates, energy levels and rates for electron collisions) are determined.

2.3.3 Diagnostics with [Fe II] lines

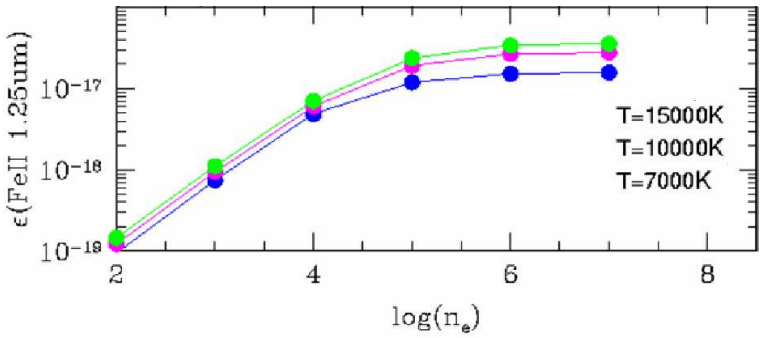

Figure 2.17: Emissivity ($\epsilon = I/N$) as a function of the electron density n_e (electrons are the main colliders for an atomic gas) for a near infrared [Fe II] emission line. Different behaviours are reported for different values of gas temperature.

The [Fe II] transitions in NIR bands were introduced in Section 2.3.1; now we want to discuss the diagnostic capabilities of these lines, considering the results presented in Section 2.3.2. First we notice that, for an atomic gas, the main colliders are electrons, then we will refer to the collider density n_0, used in Section 2.3.2, as the electron density n_e of the gas.

Electron density and gas temperature determinations

The [Fe II] line ratios in NIR bands are particularly suitable to diagnose electron density since these transitions have different critical densities (see Table 2.1), while most of the observed lines have very similar excitation energies, due to their electronic structure (see Figure 2.16).
In order to exploit the [Fe II] line intensity ratios for diagnostic purposes, we used a NLTE code (Nisini et al. 2002) to solve the Equations of detailed balance 2.48. This model considers the first 16 fine structure levels of [Fe II], comprising transitions among a^6D, a^4F, a^4D and a^4P terms; spontaneous rates are generally taken from Nussbaumer & Storey (1988), while energy levels and rates for electron collisions are adopted from Zhang & Pradhan (1995). Three theoretical [Fe II] line ratios are reported in Figure 2.18; the weak dependence of the line ratios with temperature variations is remarkable and, as a general result, NIR [Fe II] lines are suitable to measure electron densities up to 10^5 cm^{-3}.
To diagnose the gas temperature from [Fe II] line ratios, we have instead to consider transitions coming from the upper levels, such as ^4P term or further, which have excitation energies greater than 19000 K (see Section 2.3.2).

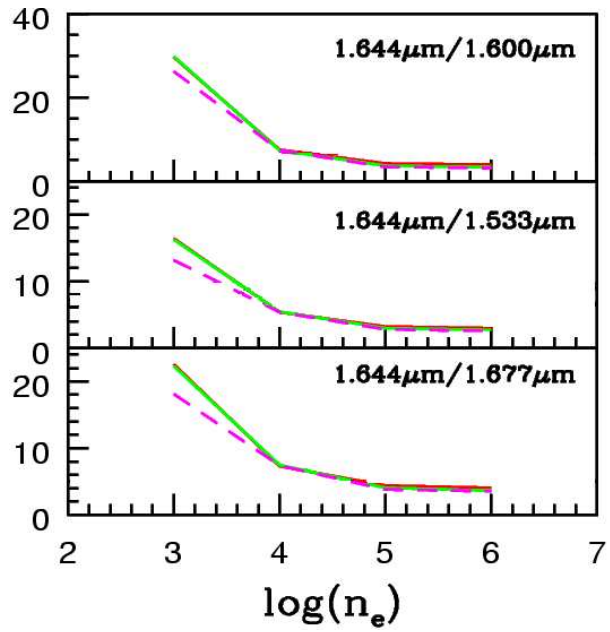

Figure 2.18: Theoretical 1.644μm/1.600μm, 1.644μm/1.533μm and 1.644μm/1.677μm [Fe II] line ratios as a function of the electron density n_e. The solid and dashed curves correspond to temperature values of T = 4 000 K and T = 15 000 respectively (Nisini et al. 2002).

Gas-phase Fe abundance

The iron gas-phase abundance (n(Fe)) in Herbig-Haro objects is expected to be regulated by the efficiency of the shock in disrupting core of the dust grains, releasing metals in the gas phase.

Estimates of n(Fe) in shock environments have so far given sparse results, from values close to the solar one (Beck-Winchatz et al. 1996), up to intermediate (Nisini et al. 2002) and very high depletion factors (Mouri & Taniguchi 2000; Nisini et al. 2005).

Recently, new methods were introduced to derive iron gas-phase abundance using NIR lines instead of optical lines. In particular [P II] lines, which are often observed in HH objects (e.g transitions at 1.147 μm and at 1.188 μm), are particularly suitable for this purpose.

These lines have interesting similarities with [Fe II] lines: they lie nearby in wavelength, they have similar excitation temperatures, critical densities, first ionization potentials (I.P.$_P$ = 10.5 eV and I.P.$_{Fe}$ = 7.9) and radiative recombination coefficients, making the [P II]/[Fe II] ratio independent from variations of extinction, temperature, density and excitation.

The important difference between iron and phosphorus is that the depletion into dust grains of the latter is very low; thus, at variance with iron, the gas-phase abundance of P in molecular clouds is close to the solar one.

Therefore, the Fe/P relative abundance gives a direct estimate of the iron depletion or, equivalently, of the efficiency of shock in dust destruction.
We can express the emissivities (see Equation 2.46) of a generic $i \rightarrow j$ transition for both [P II] and [Fe II] as:

$$\epsilon_{[\mathrm{Fe\,II}]} = \frac{h\nu_{Fe}}{4\pi} A_{[\mathrm{Fe\,II}]} f_{[\mathrm{Fe\,II}]} n_{[\mathrm{Fe\,II}]} \tag{2.61}$$

$$\epsilon_{[\mathrm{P\,II}]} = \frac{h\nu_{P}}{4\pi} A_{[\mathrm{P\,II}]} f_{[\mathrm{P\,II}]} n_{[\mathrm{P\,II}]} \tag{2.62}$$

The intensity line ratio is therefore given by[3]:

$$\frac{I_{[FeII]}}{I_{[PII]}} = \frac{\epsilon^{mod}_{[\mathrm{Fe\,II}]}}{\epsilon^{mod}_{[\mathrm{P\,II}]}} \frac{n_{[\mathrm{Fe\,II}]}}{n_{[\mathrm{P\,II}]}} \tag{2.63}$$

where we have called $\epsilon^{mod} = (h\nu)/(4\pi)Af$ the emissivity given by the theoretical NLTE models which describe the level population in relation of local values of temperature and density.
Assuming that in shock conditions phosphorus and iron are all single ionized, that means $n_{[\mathrm{Fe\,II}]}/n_{[\mathrm{P\,II}]} = n_{Fe}/n_P$, we can use Equation 2.63 for providing a direct measure of Fe/P relative abundance:

$$\frac{\chi_{Fe}}{\chi_P}(Fe/P)_\odot = \frac{I_{[FeII]}}{I_{[\mathrm{P\,II}]}} \frac{\epsilon^{mod}_{[PII]}}{\epsilon^{mod}_{[FeII]}} \tag{2.64}$$

where χ is the gas-phase element fraction with respect to the solar element abundance. When $\frac{\chi_{Fe}}{\chi_P} = 1$ the solar abundance ratio $(Fe/P)_\odot \simeq 100$ is measured (Asplund et al. 2005), which is the expected ratio when iron is all in gas-phase. Generally it is assumed that values of the $\frac{\chi_{Fe}}{\chi_P}$ ratio larger than 0.4 indicate that a fast shock has recently passed through the atomic gas, destroying most of the dust grains (Oliva et al. 2001).

2.3.4 Diagnostics with H_2 lines

The large number of H_2 lines generally observed in HH objects are a suitable tool to estimate the temperature of the molecular gas through the construction of *rovibrational* (or *Boltzmann*) *diagrams*.
The quadrupolar nature of H_2 transitions involves very weak radiative rates (two or three orders of magnitude weaker than for the typical rates for molecular tran-

[3]Here the assumption is that all the [Fe II] and [P II] emissions along line of sight are in the nebular ambient where the shock occurs.

sitions) and thus their critical densities are very low (10^2-10^3 cm^{-3} at $\sim$ 2000 K, see Equation 2.52).

For these reasons, as we saw in Section 2.3.2, the observed H_2 transitions are optically thin and quickly thermalized at the typical density values of the shocked gas. For a hydrogen molecule in a LTE distribution, the fractional population $f_{v,J}$ of a level v,J is given by the Boltzmann distribution expressed by Formula 2.56:

$$f_{v,J} = \frac{n_{v,J}}{n} = \frac{g_{v,J}}{Q} e^{\frac{-E_{v,J}}{kT}} \tag{2.65}$$

where the statistical weight $g_{v,J}$ is given by the product between the nuclear spin statistical weight and the rotational statistical weight ($g_{v,J} = (2J+1)(2I+1)$). Using the expressions 2.47 for the line intensity, we have:

$$I_{v,J} = \frac{h\nu_{v,J}}{4\pi} A_{v,J}\, N_{v,J} = \frac{h\nu_{v,J}}{4\pi} A_{v,J}\, g_{v,J} \frac{e^{\frac{-E_{v,J}}{kT}}}{Q} N \tag{2.66}$$

where $N_{v,J}$ is the column density of a level v,J and N is the total H_2 column density.

Then Equations 2.66 can be combined writing:

$$\frac{N_{v,J}}{g_{v,J}} = \frac{4\pi}{h\nu_{v,J}\, A_{v,J}\, g_{v,J}} I_{v,J} = \frac{e^{\frac{-E_{v,J}}{kT}}}{Q} N \tag{2.67}$$

and finally taking the natural logarithm:

$$ln\frac{N_{v,j}}{g_{v,J}} = ln\left(\frac{I_{v,j}\, 4\pi}{g_{v,J}\, h\nu_{v,J}\, A_{v,J}}\right) = -\frac{E_{v,J}}{kT} + ln\frac{N}{Q} \tag{2.68}$$

Thus, we can construct the Boltzmann diagram plotting the $ln\frac{N_{v,J}}{g_{v,J}}$ values (which depend from the molecular parameters and the extinction corrected line intensities) against the excitation energies $E_{v,J}$; if the gas is completely thermalized at a single temperature, the values arrange along a straight line, with a slope proportional to T^{-1} (see Figure 2.19). Moreover, the intercept gives the column density of the molecular hydrogen involved in the emission.

If the gas probed by the observed H_2 lines presents instead a temperature gradient, the data points will be displayed along a curve and different fits are therefore necessary to better represent the temperature stratifications (see Figure 2.20).

Boltzmann diagrams are also suitable tools to constrain shock models from observational data. In fact, the column density of a H_2 level is sensitive to the parameters that characterize the shock model (i.e. pre-shock density, shock veloc-

ity, the age of the shock and the strength of the magnetic field) and the response of the level populations to these variables can be seen in the Boltzmann diagram. From a qualitative point of view, if the post-shock gas is in LTE, the Boltzmann plot is a curve with a little scatter of the points about the median line. Departures from LTE enhance the scatter, i.e. the level populations are no more represented by Boltzmann distributions. In practice, increases in the shock velocity and pre-shock density act to increase the rate of collisions that vibrationally excite H_2 molecules and thus decrease the departure from LTE. The presence of a magnetic field, differently, acts to dampen and broaden the shock wave; therefore, an increased magnetic field strength enhances the departure from LTE.

Therefore, in the framework of C- and J- shock models described in Section 2.1.2, the presence of a magnetic precursor can be displayed in the Boltzmann diagram by a prominent point scatter. Moreover, in the hypothesis that the diagram is probing a gas with a single temperature, the shape of the curve suggests the type of shock occurring in the gas; a single straight line is expected in the case of a C-shock, while the curved behaviour is more marked in the J-shock case. This is what is generally observed in the theoretical Boltzmann diagrams (e.g. Giannini et al. 2006) and it can be explained considering that a C-shock is responsible for most of the emissions from lower H_2 levels, which result in an approximately constant temperature, while the temperature varies rapidly in a J-shock, which is responsible for the emissions from higher excitation levels (Flower & Pineau des Forêts 1999).

Pure C-type shocks do not predict temperatures of the molecular gas in excess of 3 000 K (see Figure 2.7), while the maximum temperature of a pure J-type shock strongly depends on the shock velocity. For high velocity J-type shocks, the molecular gas is dissociated and H_2 reforms further downstream, when temperatures decrease below $\sim$ 500 K (see Figure 2.5); then, only low excitation temperature lines are predicted by this model. In low velocity J-type shocks, on the other hand, H_2 is not dissociated; thus, also lines coming from high vibrational levels are excited and visible on the Boltzmann diagrams.

In bow shocks, the behaviour of Boltzmann diagrams depends on the region of the bow sampled by the observations; as we have seen, the velocity at the head of the bow could be high enough to create a dissociative J-shock cup, while C-type shocks are expected in the bow wings, where the velocity is lower.

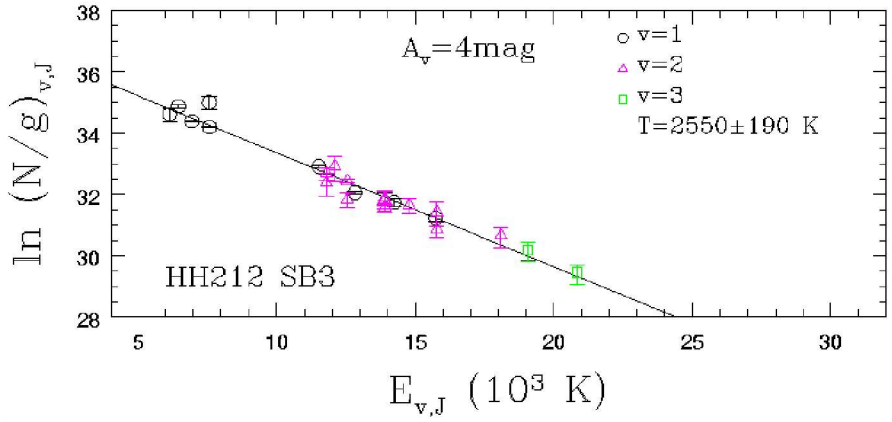

Figure 2.19: Example of Boltzmann diagram in which observational points are well fitted by a single temperature (Caratti o Garatti et al. 2006).

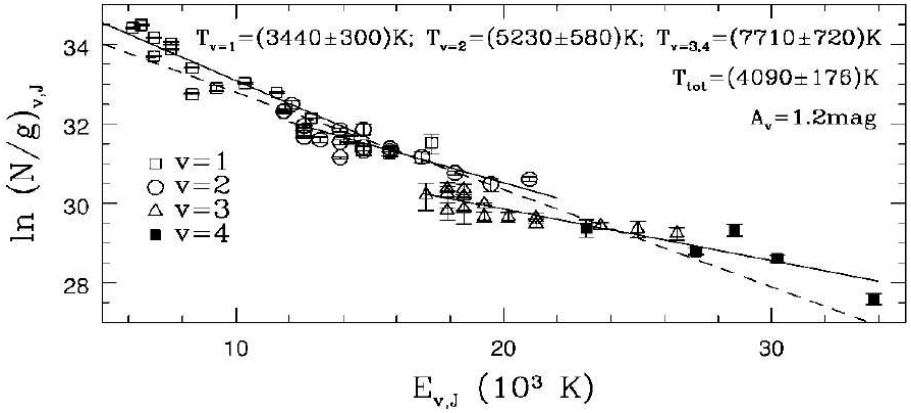

Figure 2.20: Example of Boltzmann diagram in which three different linear fits better reproduce the temperature stratification (Giannini et al. 2002).

2.3.5 Visual extinction determination

The wide sample of molecular hydrogen and [Fe II] lines observed in HH objects are very suitable also to determinete the extinction occurring in the observed molecular and atomic gas.

The theoretical intensity ratio between two optically thin lines originating from the same upper level is (see Equation 2.47):

$$\frac{I_1}{I_2} = \frac{\nu_1}{\nu_2}\frac{A_1}{A_2} \tag{2.69}$$

This ratio is independent from the local physical conditions, being a function only of atomic parameters (i.e. line frequencies ν and A coefficients).

Since the observed line depends on the extinction A_λ at the line wavelength λ,

$$I_{obs} = I \cdot 10^{-A_\lambda/2.5} \tag{2.70}$$

the ratio 2.69 becomes:

$$\frac{I_{obs1}}{I_{obs2}} = \frac{I_1}{I_2} 10^{-(A_{\lambda_1} - A_{\lambda_2})/2.5} \tag{2.71}$$

where $A_{\lambda_1} - A_{\lambda_2}$ is the differential extinction, or reddening ($E(\lambda_1 - \lambda_2)$), between λ_1 and λ_2.

If the Einstein A coefficients and the line frequencies are known, the theoretical ratio 2.69 for the selected transitions is determined; then, having a measure of the observed intensity ratio, it is possible to derive the reddening $\mathrm{E}(\lambda_1 - \lambda_2)$. Adopting an extinction law (i.e. $A_V = f(A_\lambda, \lambda)$) the visual extinction A_V is determined. It is also important to highlight that the two lines should be selected with sensibly different wavelengths, in order for the considered ratio to be a good indicator of extinction.

Several bright H_2 lines observed at NIR wavelengths can be selected to obtain an accurate determination of the extinction, as the 1-0S(1) at 2.12 μm, the 1-0S(2) at 2.03 μm, the 2-0S(1) at 1.16 μm and the 2-0Q(3) at 1.25 μm lines. However some bright H_2 lines, as the 1-0Q(3) at 2.42 μm and the 1-0Q(4) at 2.44 μm lines, suffer from poor atmospheric transmission at their wavelengths, making them no longer suitable for extinction determination.

In regions where molecular and atomic gas are spatially separated, as in bow shocks, both molecular hydrogen and ionized iron lines can be used to determine the extinction along the line of sight of the whole extended source.

The extinction measure performed using [Fe II] lines unfortunately suffers from an uncertain on the determination of A coefficients. Nowadays, two distinct sets of A values are listed in literature: one computed with different methods by Quinet et al. (1996) and the other provided by Nussbaumer & Storey (1988).

In order to understand how this uncertain affects the line intensity measurements and, as a consequence, their diagnostic capability, let us consider the ratio between the two bright [Fe II] transitions at 1.64 μm and 1.25 μm often used for this purpose (see Section 4.4.1).

The value of A ratio estimated by Nussbaumer & Storey (1988) is 31% higher than the Quinet et al. (1996) one; thus, adopting the extinction law of Rieke & Lebofsky (1985)[4], the A_V obtained with the Nussbaumer & Storey (1988) co-

[4]that can be approximated as: $I = I_{obs} \cdot 10^{0.168 \cdot A_V \cdot \lambda^{-1.75}}$

efficients results 2.7 mag greater than the one obtained with the Quinet et al. (1996) coefficients. This implies that the line intrinsic intensities obtained with the Nussbaumer & Storey (1988) model are larger and, even if this increase does not excessively affect the NIR lines (the intensity grows by a factor of 2.8 for a line at 1 μm and a factor of 1.4 for a line at 2 μm), it becomes important at optical wavelengths (the intensity grows by a factor of 33.6 for a line at 0.5 μm).

In principle, the values of the A coefficients can be empirically derived from observations of [Fe II] lines in objects of known extinction, through Equations 2.69 and 2.71. In this way, a third list of A coefficients, based on the observation of P Cygni, was recently given by Smith & Hartigan (2006) which implies A values 10%-40% higher than the theoretical values.

In Chapter 4 this method will be used to infer the A coefficients of some [Fe II] transitions and a discussion will be given on the main observational problems affecting this procedure.

Chapter 3

NIR long-slit spectroscopy of HH objects

This Chapter aims to present the analysis of three Herbig-Haro objects (HH26, HH120, HH240) by means of their near-infrared, long-slit spectra acquired with the spectrograph ISAAC (at VLT). The excitation and kinematic properties of these shocked regions are derived through a diagnostic analysis performed on H_2 and atomic ([Fe II]) lines, following the procedures described in Chapter 2.

3.1 Observations

ISAAC (Infrared Spectrometer And Array Camera[1]) is an infrared (1-5 μm) imager and spectrograph located at the Unit Telescope 1 (UT1) of the Very Large Telescope at Cerro Paranal (e.g. Moorwood 1998).
Figure 3.1 shows the optical layout of ISAAC: the instrument is composed of two independent optical arms, one equipped with an 1024 $\times$ 1024 pixels Hawaii Rockwell array suitable for short wavelengths (SW, 1-2.5 μm) and the other equipped with an 1024 $\times$ 1024 pixels InSb Aladdin array for long wavelengths (LW, 2.5-5 μm). Spectroscopy with ISAAC is performed through 2 gratings, for Low and Medium Resolution (LR and MR), 4 slits of different widths (0.3, 0.6, 1 and 2 arcsec) whose length is 120 arcsec, and 6 filters, 4 of which cover the SW interval and the others the LW interval.
The final spectral resolution of the instrument depends on the grating and the slit used, as is summarized in Table 3.1 for the case of SW spectroscopy.
A calibration unit is located inside the instrument for both wavelength calibration (Xenon and Argon lamps) and spectroscopic flat-fielding.

[1] http://www.eso.org/instruments/isaac/

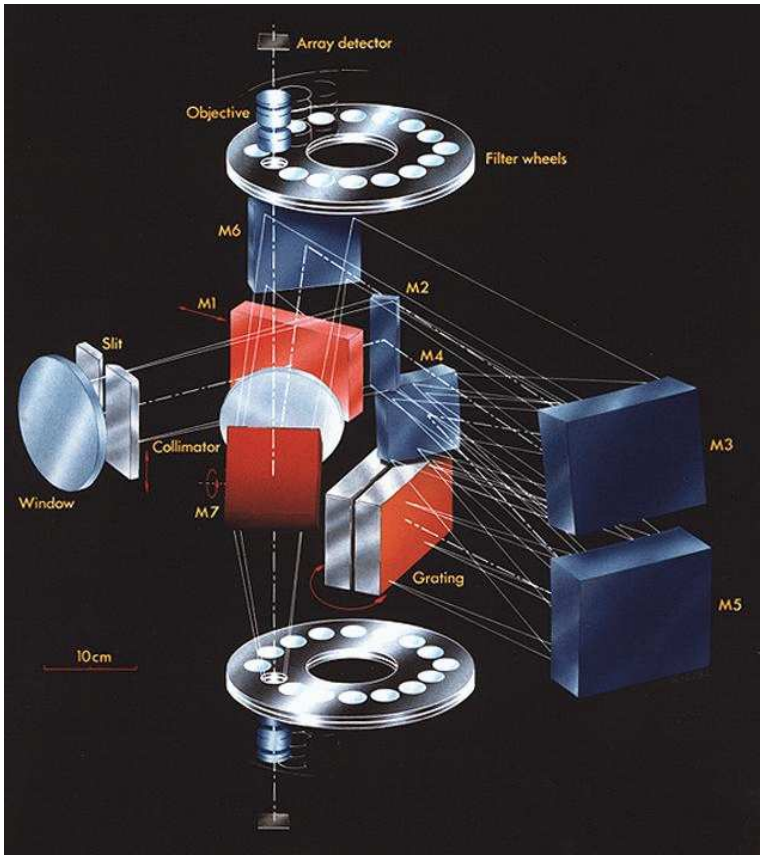

Figure 3.1: ISAAC optical layout. The light coming from the telescope enters the instrument through the slit (left side). If the instrument is set as a spectrograph, the M1 mirror is retracted and the light is collimated by several mirrors to the grating; from here, following the same optical path and, finally, through the M6 and M7 mirrors, the light is directed to one of two optical arms (the top and bottom cameras are optimized for the 1-2.5 μm and 2-5 μm spectral range respectively), where it is focused through an objective onto the detector array. (ISAAC User's Manual)

For the observations exposed in this Chapter, we used the instrument in the SW configuration, characterized by a field of view of $2.5' \times 2.5'$ and a pixel scale of $0.147''$. The HH sample were observed in December 2005; in particular, spectral images of HH26 and HH120 were acquired in MR mode with a $0.3''$ slit (corresponding to R=8 900-10 000), while HH240 was observed in LR mode (with a $0.6''$ slit, R=840-860). Table 3.2 summarizes the log of the observations.
Spectroscopic images were acquired by nodding the telescope in order to remove the sky emission, alternating frames with the source in two different positions (A and B), following the order A, B, B′, A′, A″, B″ and so on (ABB′A′ procedure, see ISAAC User's Manual[2]). Moreover a couple of telluric O-type standard stars were observed before and after each on-source integration in order to remove the

[2]www.eso.org/instruments/isaac/doc

Table 3.1: ISAAC spectral resolution for SW spectroscopy. The resolution in each spectral domain is reported for the 1″ slit. For the other slits, the resolution scales as R/d, where d is the slit width.

Spectral range (μm)	Spectral coverage (μm)	R(1″)
SW - LR		
0.98 - 1.10	0.29	550
1.10 - 1.40	0.36	500
1.42 - 1.82	0.48	500
1.82 - 2.50	0.72	450
SW - MR		
0.98 - 1.10	0.046	3 400
1.10 - 1.40	0.059	3 100
1.40 - 1.82	0.079	3 000
1.82 - 2.50	0.122	2 600

Table 3.2: Log of the observations.

Object	Location	Distance (pc)	Band (μm)	Resolution	Integration Time (s)
HH26	L1630	400	1.61-1.69	10 000	2 400
			2.08-2.20	8 900	2 400
			2.19-2.31	8 900	2 400
HH120	CG30	450	1.61-1.69	10 000	3 200
			2.08-2.20	8 900	2 400
			2.19-2.31	8 900	2 400
HH240	L1634	460	1.07-1.43	860	1 800
			1.41-1.89	840	2 400

atmospheric spectral response.
Reduction, calibration and analysis were performed using IRAF packages and IDL scripts; in particular, wavelength calibration was performed, in the high resolution images, using the OH atmospheric lines observed on the target frames and, in the low resolution spectral images, using the Xenon-Argon lamps.
The estimated uncertainty in wavelength calibration in high resolution mode is within 3 km s^{-1}, derived directly from OH atmospheric lines fitting, and the instrumental broadening, as measured from Gaussian fits to OH lines, is 18 km s^{-1} and 14 km s^{-1} in H and K filters, respectively. This corresponds to a velocity spread uncertainty which is smaller than the spectral resolution element, that is 30 km s^{-1} and 34 km s^{-1}, respectively.

3.2 Analysis and Results

3.2.1 HH26

HH26 is a Herbig-Haro object situated in the L1630 Orion dark cloud at a distance of $\sim$ 400 pc (Anthony-Twarog 1982). Figure 3.2 shows a H_2 image of the HH26 region where the ISAAC slit position through the knot HH26A and the exciting source HH26IRS is superimposed. Table 3.3 reports the lines observed, together with the spectral identification, the vacuum wavelength and the excitation energy. This region is a site of active star formation where several HHs (HH24-HH26) and young stellar objects, in different evolutionary states, are located (Giannini et al. 2004). The protostar HH26IRS (α_{2000}=$05^h46^m03.9^s$, δ_{2000}=-00°14′52.5″) drives an extended molecular outflow, traced by millimetric transitions of CO molecule (Gibb & Heaton 1993). Imaging in the 2.12μm H_2 line (Davis et al. 1997) reveals a string of shocked H_2 knots (HH26A - HH26D) along the outflow axis, which represents the infrared counterpart of the blueshifted molecular lobe associated with this source.
Proper motion was measured in HH26 by Chrysostomou et al. (2000), who found velocities ranging from less than 70 up to 200 km s^{-1}; the lowest value pertains to HH26A, which should be a stationary shock region, while the highest is associated with HH26C, which should represent the working surface of the bow shock.
Optical spectra and images obtained by Jones et al. (1987) show that the HH26 region consists of four low excitation knots, supporting the interpretation of a zone of turbulent interaction between the jet flow and the surrounding environment (Davis et al. 2000).

Table 3.3: Lines observed in high resolution mode.

Line	λ_{vac} (μm)	E_{up} (K)	Object(s)
	H_2 lines		
1-0S(0)	2.2233	6471	HH26, HH120
1-0S(1)	2.1218	6951	HH26, HH120
1-0S(9)	1.6877	15723	HH26, HH120
1-0S(10)	1.6665	17312	HH26, HH120
1-0S(15)	1.6314	26264	HH26
1-0S(17)	1.6457	30156	HH120
1-0S(19)	1.6750	34131	HH26
2-0O(8)	1.6104	14764	HH26
2-0O(9)	1.6796	15764	HH26, HH120
2-1S(1)	2.2477	12551	HH26, HH120
2-1S(2)	2.1542	13151	HH26, HH120
3-1O(7)	1.6453	19087	HH26, HH120
3-2S(2)	2.2870	18387	HH26, HH120
3-2S(3)	2.2014	19087	HH26, HH120
3-2S(4)	2.1280	19913	HH26, HH120
4-2Q(13)	1.6123	32857	HH26, HH120
4-2O(5)	1.6223	22760	HH26, HH120
4-3S(5)	2.2010	25625	HH26, HH120
4-3S(6)	2.1460	26618	HH120
4-3S(7)	2.1004	27708	HH26
5-3O(3)	1.6135	26737	HH26, HH120
6-4Q(3)	1.6162	31663	HH26
6-4Q(5)	1.6431	32714	HH26
6-4Q(7)	1.6829	34175	HH26
7-5S(1)	1.6205	35616	HH26
	Atomic lines		
[Fe II] $a^4D_{7/2}$–$a^4F_{9/2}$	1.6440	11446	HH26, HH120
[Fe II] $a^4D_{5/2}$–$a^4F_{7/2}$	1.6773	12074	HH120
[Fe II] $a^4D_{3/2}$–$a^4F_{7/2}$	1.5999	12489	HH240
[Fe II] $a^2H_{11/2}$-$a^2G_{9/2}$	2.2244	29265	HH120
[Si I] $^1D_2$-$^3P_2$	1.6459	9063	HH26

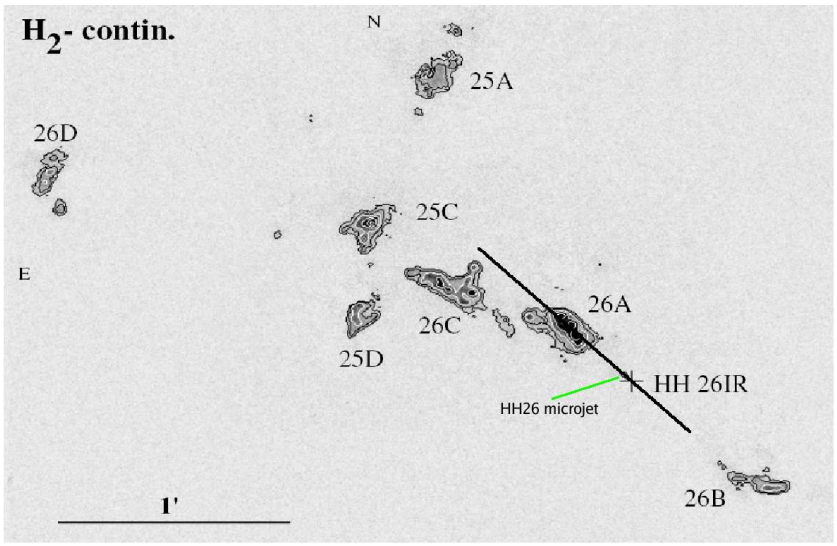

Figure 3.2: H_2 image of the HH26 region taken with the 3.8 m U.K. Infrared Telescope (UKIRT, Hawaii) (Davis et al. 1997). The ISAAC slit position is superimposed.

More recently, the analysis of near-infrared atomic and molecular lines performed by Giannini et al. (2004) showed that the HH26A emission can be explained with a J-shock with magnetic precursor model ((C+J)-shock model). This interpretation is moreover supported by far infrared spectra of the HH26 region obtained by Benedettini et al. (2000), who interpreted the observed emission (from [OI], CO, H_2O and H_2 lines) as due to a mixture of C- and J-type shocks.

H_2 Excitation diagram

The high resolution spectra of HH26 show a considerable number of H_2 transitions (23 lines, see Table 3.3) in a wide range of excitation energies (from $\sim$ 6 000 K to $\sim$ 36 000 K). Thus, the excitation structure of this source can be investigated following the method of the Boltzmann diagram (see Section 2.3.4).
The analysis starts by considering the Boltzmann diagram of HH26A developed by Giannini et al. (2004), which is shown in Figure 3.3; these authors observed transitions up to v=4 and E_{up}=27 000 K and the data points were fitted with a single straight line, obtaining a gas temperature of T= 3 360 $\pm$ 110 K. This is of the order of the peak temperature predicted in non-dissociative C-shocks, even if a departure of data points relative to high excitation transitions from a single straight line suggests the presence of a J-type shock component (see Section 2.3.4). Thus, observations were interpreted in the framework of a J-type shock with magnetic precursor with $V_{shock} = 52$ km s^{-1} and $n_H = 10^4$ cm^{-3} (pre-shock density).

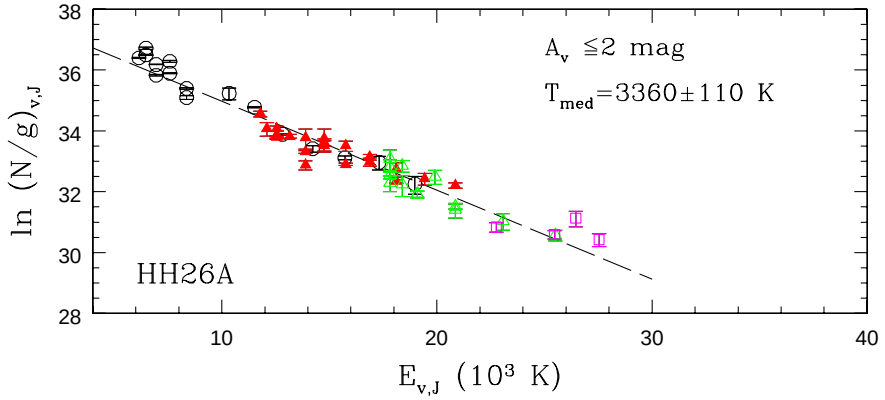

Figure 3.3: Boltzmann diagram of HH26A reported in Giannini et al. (2004). White circles, red triangles, green triangles and magenta squares represent transitions coming from the vibrational levels 1,2,3,4 respectively. The temperature value refers to the displayed linear fit.

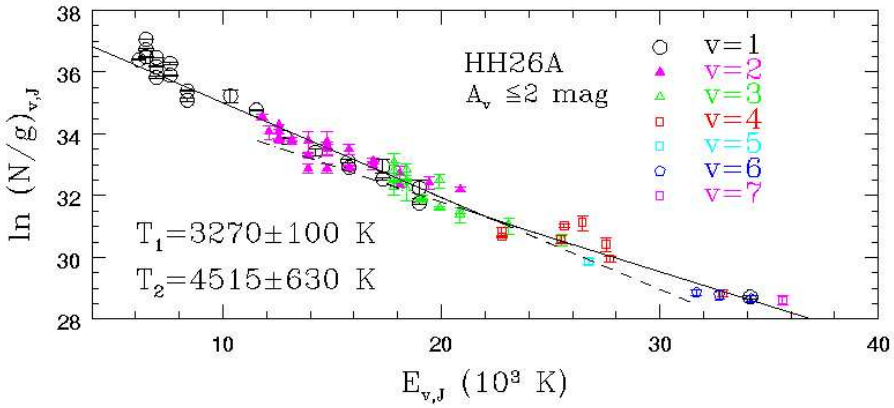

Figure 3.4: Boltzmann diagram of HH26A obtained integrating the lines observed with ISAAC with those observed by Giannini et al. (2004). The departure from a single straight line at high energies suggests the existence of a temperature stratification of the molecular gas.

In order to test the predicted (C+J) model on the basis of a larger number of lines, the transitions observed with ISAAC were used to complement the Boltzmann diagram of Giannini et al. (2004), obtaining the plot shown in Figure 3.4. The visual extinction adopted by Giannini et al. (2004) ($A_V \leq 2$) was assumed for the data analysis and the transitions coming from different vibrational levels are indicated with different symbols (from v=1 to v=7), to better represent the rotational series within the same vibrational level.

The new data, observed with high signal-to-noise ratio up to $E_{up} \sim 40\,000$ K, results in a Boltzmann diagram which shows a departure from a straight line at the high excitation levels. This behaviour suggests that more than a single temperature must be considered to describe the excitation conditions of the molecular gas; in particular two different temperatures were identified ($T_1 = 3\,270 \pm 100$ K

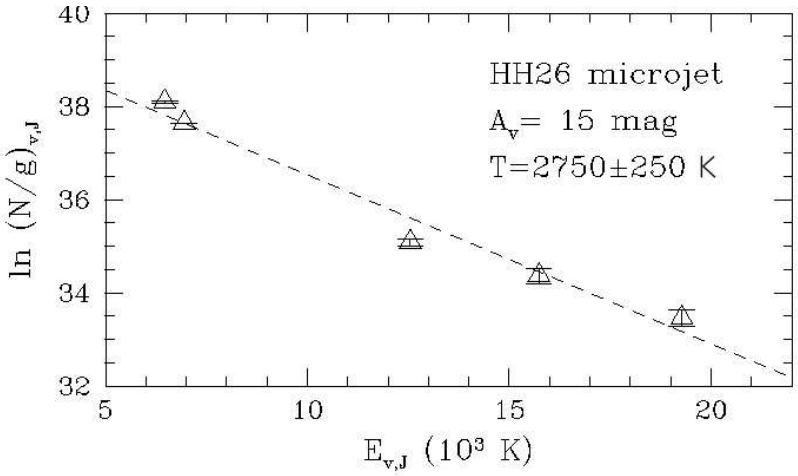

Figure 3.5: Boltzmann diagram of the microjet obtained with five low excitation H_2 lines.

and $T_2 = 4\,515 \pm 630$ K) matching the low excited ($E_{up} < 22\,000$ K) and high excited ($E_{up} > 22\,000$ K) lines respectively.

This temperature stratification confirms the hypothesis that a (C+J) model is suitable to describe this shocked region, where the high energy H_2 levels are populated by the discontinuous J-component, which generates the higher temperature component of the shock. Nevertheless, the T_2 temperature suggests a new scenario according to which molecular hydrogen could survive also at temperatures higher than 3 000 K; this aspect will be better discussed in Chapter 4, where a more sofisticated analysis of the bowshock HH99, performed with integral field spectroscopic data, will confirm this result.

In addition to HH26A, ISAAC observations encompass the H_2 microjet located close to the HH26IR source (see Figure 3.2). Such a feature was firstly identified by Davis et al. (2001), who called this kind of small scale jet as Molecular Hydrogen Emission Line (MHEL) regions, in analogy to the FEL (Forbidden Emission Lines) regions detected in T Tauri stars.

The Boltzmann diagram of the HH26 microjet was obtained by considering five low excitation lines detected in this region, which are the 1-0S(0), 1-0S(1), 1-0S(9), 2-1S(1) and 2-1S(2) lines. The result is shown in Figure 3.5; the best linear fit is obtained taking $A_V = 15$ mag and the resulting temperature is $2\,750 \pm 250$ K.

As a consequence of the comparison of Boltzmann diagrams obtained in HH26A and in the microjet, it is possible to infer that the jet is propagating from a dense environment ($A_V = 15$ mag), located close to the HH26IRS source, to a region (HH26A) with a small extinction value ($A_V \leq 2$ mag). At the same time, the temperature of the molecular gas increases moving from the microjet to the HH26A knot. This aspect will be better discussed in the following.

Kinematic structure

The kinematical structure of the HH26 jet can be investigated by considering the P-V diagrams (see Section 2.2.1) shown in Figure 3.6, obtained with the high resolution spectral images of the 1-0S(1) line at 2.12 μm and [FeII] line at 1.64 μm. The H_2 spectral image shows the very complex structure of HH26, which

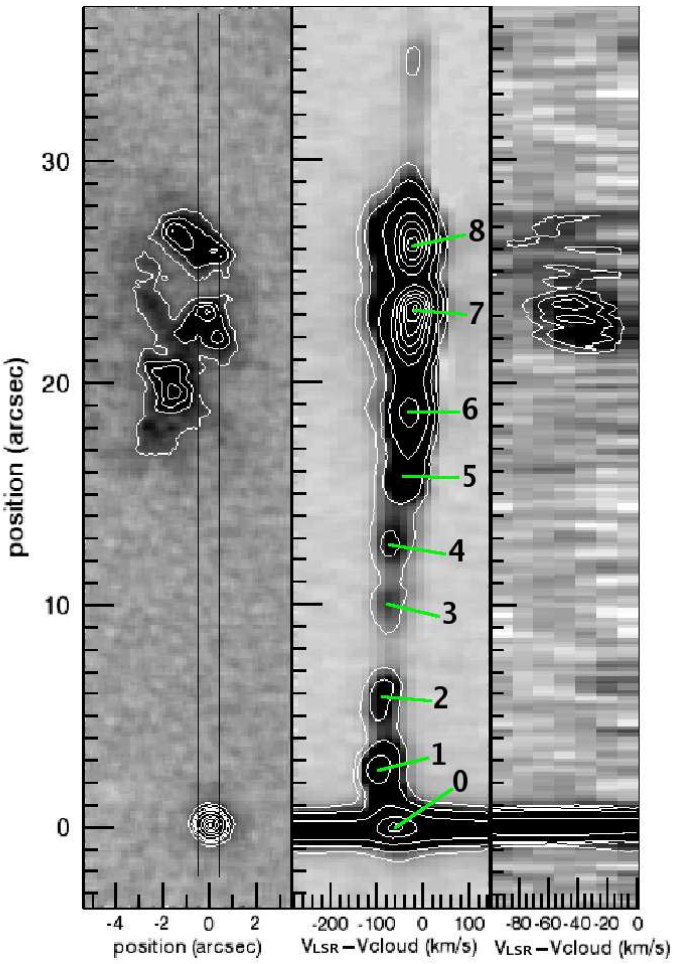

Figure 3.6: H_2 2.12μm line (central panel) and [FeII] 1.64μm line (right panel) are compared with the ISAAC acquisition image in H_2 narrow band (left panel). The slit position is reported along HH26A and the outflow exciting source HH26IRS; the zero spatial position is referred to the latter. The reported radial velocities are specified with respect to the ambient cloud velocity (Milman 1975). The positions of the 9 knots identified for the spectral analysis are reported.

is composed of several substructures generated by the subsequent interaction between the jet and the ambient medium.

For the spectral analysis, 9 different apertures (corresponding to the individual knots) were selected at the positions of the emission peaks along the slit direction; the peak positions and the radial velocities are reported in Table 3.4. The bright knots 7 and 8 correspond to the region generally identified as HH26A, while the

Table 3.4: Position and radial velocity of the apertures (knots) selected for the spectral analysis of HH26A. The radial velocity is with respect to the local cloud (V_{cloud} = 11 km s^{-1} Milman 1975) and the peak positions are expressed as offset from HH26IRS.

Knot	Peak position (arcsec)	V_{LSR} - V_{cloud} [1] (km s^{-1})
0	0	-59.6
1	2.8	-90.7
2	5.7	-86.5
3	9.8	-75.2
4	12.9	-70.9
5	15.4	-34.2
6	18.8	-24.3
7	23.2	-17.2
8	26.3	-17.2

[1]The uncertainty on the radial velocity is estimated around 3 km s^{-1}.

label 0 indicates the position of the source HH26IR is indicated. Other knots are observed for the first time; among them, knots 1 and 2 identify the microjet. The aperture sizes selected for the spectral analysis are reported in Figure 3.7, superposed to the spatial profiles of 1-0S(1) and 2-1S(1) lines.
Two main results emerge:
(i) the observed knots are all blueshifted (see velocity values reported in Table 3.4);
(ii) the jet accelerates in the internal region close to the source (knots 0 and 1), reaching the maximum radial velocity of $V \sim 91$ km s^{-1}. Further out, the jet decelerates until it reaches a constant velocity of $V \sim 17$ km s^{-1} at the position of the terminal shock surface (HH26A).
To study the kinematic structure in detail, in Figure 3.8 the squares of velocities of each knot against the distance from HH26IRS are plotted, having corrected both velocities and distances for the inclination angle of the flow direction with respect to the line of sight (65°, Davis et al. 2000). The linear fits to the data points provide the accelerations occurring through the knots from a measure of the angular coefficients (the direct measure of the angular coefficient provides the double of the acceleration, as it derives from the conservation of energy). In particular, 4 different linear fits (shown in Figure 3.8) were performed: the first provides a measure of the acceleration ($\sim 7 \cdot 10^{-9}$ km s^{-2}) close to the exciting source, while the others show how the jet progressively decelerates ($\sim$1.5, $\sim 0.7 \cdot 10^{-9}$ km s^{-2}) until it reaches a constant velocity.

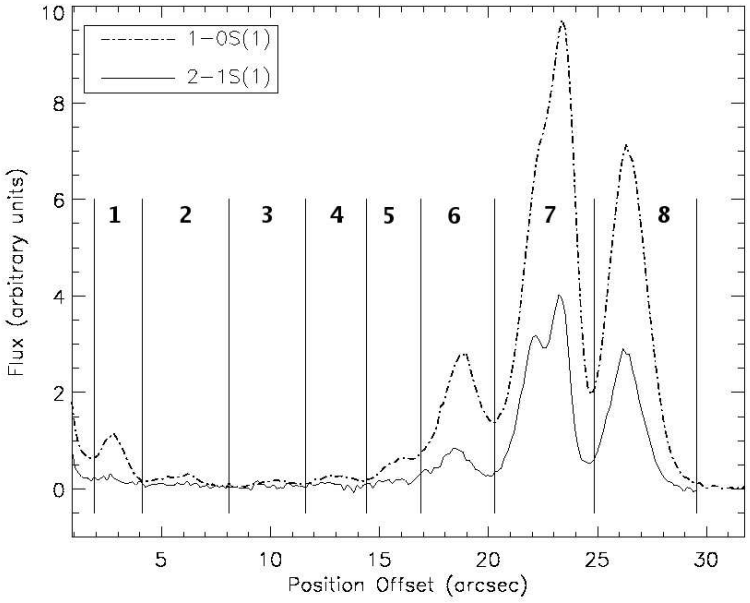

Figure 3.7: Spatial profile of 1-0S(1) and 2-1S(1) lines as a function of the distance from HH26IRS. Vertical lines define the apertures used for the spectral analysis. The signal-to-noise ratio of the 2-1S(1) spectra obtained in the regions of low intensity (i.e. apertures 2, 3 and 4) is greater than 4.

We expect that such deceleration corresponds to a transfer of the kinetic energy of the jet into thermal energy of the gas; hence, we expect a temperature enhancement in those knots where a deceleration is evident.

To verify this hypothesis, we selected the ratio between 1-0S(1) and 2-1S(1) lines (see in Figure 3.7 the spatial profiles along the knots of these transitions). This ratio represents a valuable probe of the temperature of the molecular gas, which can be estimate by adopting a LTE model (see Section 2.3.4); in particular, the two transitions have different excitation energies ($\Delta E \sim 6\,000$ K) and similar wavelengths, so that their ratio is a good pointer of temperature variations and, simultaneously, independent on the extinction. As we have seen, to provide an accurate estimate of the gas temperature, a large number of lines is needed to construct a Boltzmann diagram (e.g. see Figure 3.4); for this reason we limit ourselves to evaluate just the temperature variations.

Figure 3.9 shows, for each considered knot, the temperature offset measured from the 2-1S(1)/1-0S(1) ratio. The offset is given with respect to the temperature value measured in knot 0 (T$\sim$2700 K, see Figure 3.5). This plot essentially shows an increase in temperature moving from the internal region close to HH26IRS to the external shock surface (HH26A). This behaviour, if compared with the decreasing values of both the peak radial velocities (see Table 3.4) and accelerations

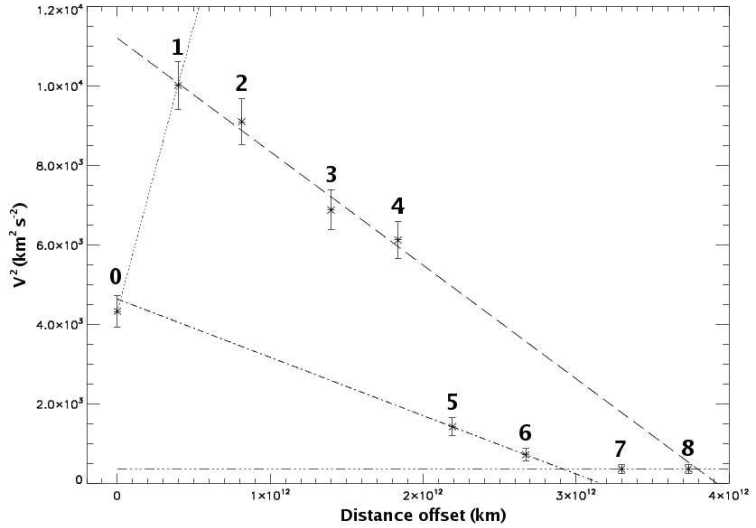

Figure 3.8: HH26 acceleration plot. Distances and velocities are corrected for an inclination angle of 65° with respect to the line of sight (Davis et al. 2000). According to the reported linear fits, we obtain an acceleration $\sim 7 \cdot 10^{-9}$ km s^{-2} occurring between knots 0 and 1, followed by 2 decelerations ($\sim$1.5 and $\sim 0.7 \cdot 10^{-9}$ km/s^{-2}) until a constant velocity is reached.

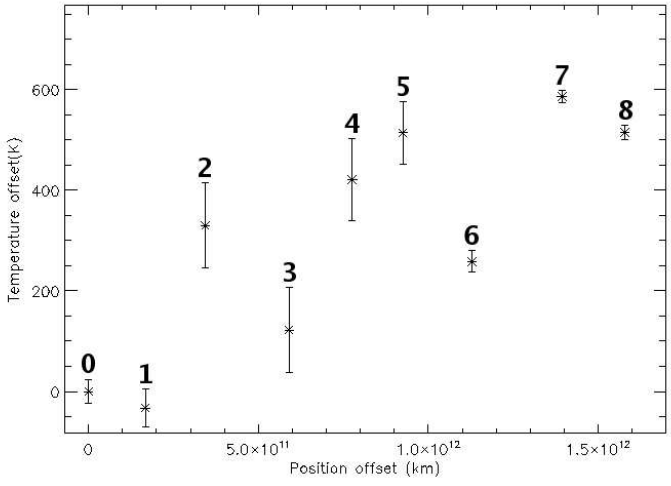

Figure 3.9: Temperature offset (with respect to the temperature value measured in knot 0) at each knot position. The temperature values are computed by the 2-1S(1)/1-0S(1) ratio under LTE conditions.

(see Figure 3.8), suggests that the increase in temperature comes from the loss of kinetic energy.
Nevertheless, this measure is affected by the long-slit instrumental setup which, selecting a restricted region of the shocks, is sensitive to the local variations of temperature. This can explain the local temperature minimum at knot 3 and knot 6 positions. In Chapter 4 the variation of molecular gas temperature along the bow shock structure will be pointed out adopting the IFU spectroscopy.

Bow shock morphology

The high resolution line profiles of H_2 and [Fe II] transitions provide an interesting tool to put constraints on the shock type (see Section 2.2).
In particular, the [Fe II] transition at 1.64 μm, detected with a signal-to-noise ratio ~ 10 (see Figure 3.10), can be used to estimate a shock velocity ~ 60 km s^{-1} and a peak velocity $\sim$ -43 km s^{-1}, using the Equations 2.30 and 2.38 respectively. This result indicates that the atomic gas in the jet is blue-shifted (as in the case of molecular outflow) and that the measured shock velocity is consistent with the one predicted by Giannini et al. (2004) according to a (C+J) shock model ($V_{shock} = 52$ km s^{-1}).
At variance with [Fe II], the H_2 transition at 2.12 μm shows a very high signal-to-noise ratio (about 1700); thus, this line profile (see Figure 3.11) can be used to perform a detailed comparison with bow shock models.
In particular, we consider the model developed by Schultz et al. (2005), described in Section 2.2, of a parabolid bow shock approaching the observer. To better compare the observed line profile with the theoretical ones (see Figure 2.11), the 1-0S(1) line shape is shown in Figure 3.11 by normalizing the velocities to the shock velocity (60 km s^{-1}), and the intensity to the peak intensity. In this comparison it is important to have in mind that the theoretical profiles are generated considering the emission coming from the entire bow surface, while the observed line originates from a restricted bow region selected by the slit.
From this comparison it follows that:
(i) as a first approximation, the overall symmetry of the observed line profile is consistent with a paraboloid geometry. Indeed, models with different shapes would produce very asymmetric spectral profiles (Schultz et al. 2005);
(ii) the presence of a marked blue wing suggests two possible, alternative interpretations: the first, which originates from a direct comparison of the observed line profile with the theoretical ones (see Figure 2.11), states that the strength of emission coming from the region close to the bow apex increases relatively to the

emission coming from the rear regions. This behaviour suggests that no molecular dissociation occurs at the bow head, as could be expected for a bow with V_{bow}= 60 km s^{-1}, and that the efficiency in converting kinetic energy in gas excitation is high. The second interpretation considers the slit observational setup; if the slit intercepts the bow head, the relative contribution of the high-blue velocities with respect to the central velocities can simply increase because a large part of the rear region of the bow is not observed.

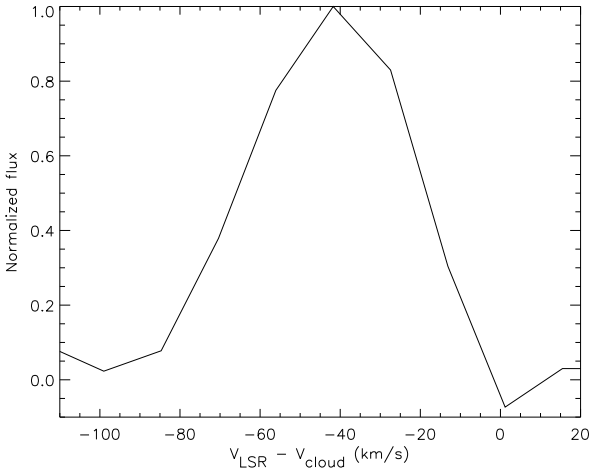

Figure 3.10: High resolution line profile of [Fe II] at 1.64μm observed in the HH26A region. The peak radial velocity is V_{peak} =-43 km s^{-1}.

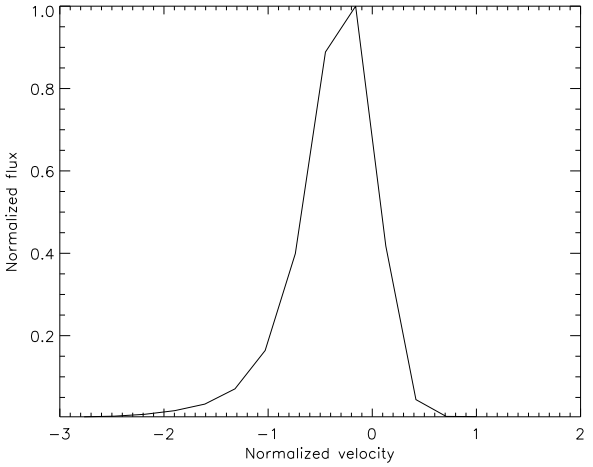

Figure 3.11: High resolution line profile of 1-0S(1) line at 2.12 μm observed in the HH26A region. The observed radial velocities are normalized with respect to the bow velocity ($V_s = 60$ km s^{-1}), while the flux is normalized to the peak intensity.

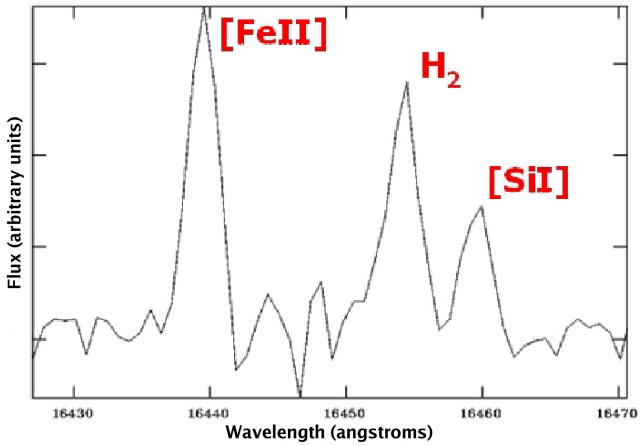

Figure 3.12: Segment of the HH26A spectrum where the line identified as the [SiI] transition is compared with the 3-1O(7) H_2 line and with the only observed [Fe II] line at 1.644 μm.

A possible silicon detection

The brightest transition of the neutral silicon ([SiI]) in the NIR falls in the H band at 1.6459 μm. The upper level of this transition can be easily populated in shock regions ($E_{up} = 9\,063$ K) and the abundance of the silicon in the interstellar medium is comparable to that of Fe, Mg and S (of the order of 10^{-5} with respect to the hydrogen). Nevertheless, [SiI] transitions were never observed in jets because the Si ionization potential (8.2 eV) allows this element to be easily ionized in presence of shock waves or ionizing photons.

In the high resolution spectra of HH26A, a feature observed with S/N=6 (see Figure 3.12) might be identified as the [SiI] transition at 1.6459 μm, according to the following motivations:

(i) the ionization potential of Si is close to but larger than the Fe one (7.9 eV); thus the observation of a very faint [Fe II] emission (generally, HH objects show prominent [Fe II] emissions) is consistent with the presence of Si in neutral form;

(ii) the observed feature, if identified as a [SiI] line, should present a blue-shifted peak velocity of -38 km s^{-1}, which is in full agreement with the peak velocity measured on H_2 and [Fe II] lines.

The only alternative to the [SiI] identification is that the observed feature is the 1-0S(17) H_2 transition at 1.6457 μm. However, the 1-0S(17) line should result red-shifted by $\sim$ 10 km s^{-1}, which is rather improbable given that the other 23 detected H_2 transitions have a blue-shifted peak velocity.

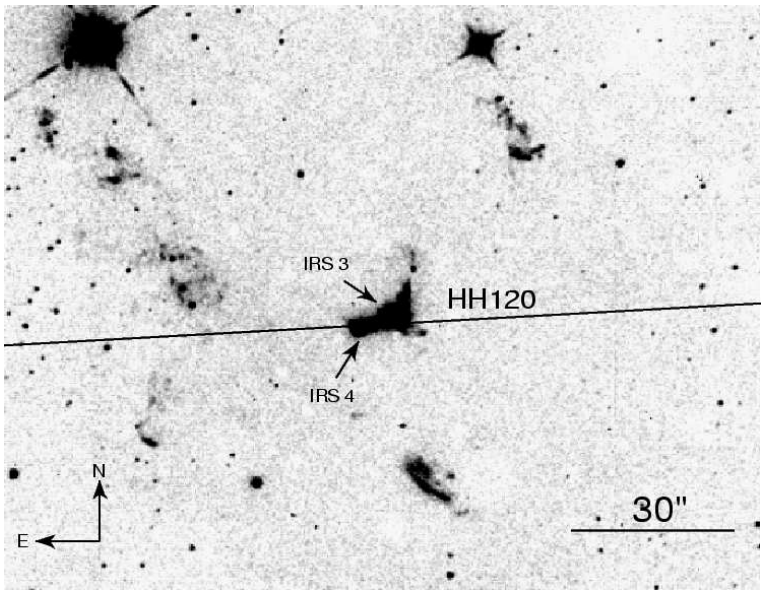

Figure 3.13: H_2 image of HH120 region taken with the New Technology Telescope (NTT, La Silla) (Nisini et al. 2002). The ISAAC slit position is superimposed.

3.2.2 HH120

HH120 is a compact object situated in the cometary globule CG30 of the Gum Nebula (Pettersson 1984), at a distance of about 450 pc (Graham & Heyer 1989). Figure 3.13 shows the ISAAC slit position superimposed on a H_2 image of HH120 region. Table 3.3 reports the observed lines, togheter with the spectral identification, the vacuum wavelength and the excitation energy.

Two infrared sources are identified inside the nebulosity of HH120: the young source IRS4 (α_{2000}=$08^h09^m32.8^s$, δ_{2000}=-36°05′00.0″), which is considered as the exciting source of the jet (Pettersson 1984), and the source IRS3, which has been identified as a reflection nebula (Gredel 1994).

Near-infrared studies show that HH120 is characterized by a prominent emission of both [Fe II] and H_2 lines (Nisini et al. 2002), which prove to be spatially correlated although not coincident, suggesting the presence of both a slow C-type shock responsible for the H_2 emission and a fast J-type shock able to dissociate the gas and produce the copious ionic emission (Gredel 1994).

Kinematic structure

The kinematic structure of the HH120 region was investigated through P-V diagrams of the 1-0S(1) line at 2.12 μm and of the [FeII] line at 1.64 μm (see Figure 3.14).

The 1-0S(1) line spectral image shows the HH120 knots (identified by the nomen-

clature A, B and K) and the presence of a faint counterjet located symmetrically with respect to the IRS4 source. The [Fe II]1.64μm line image shows only the

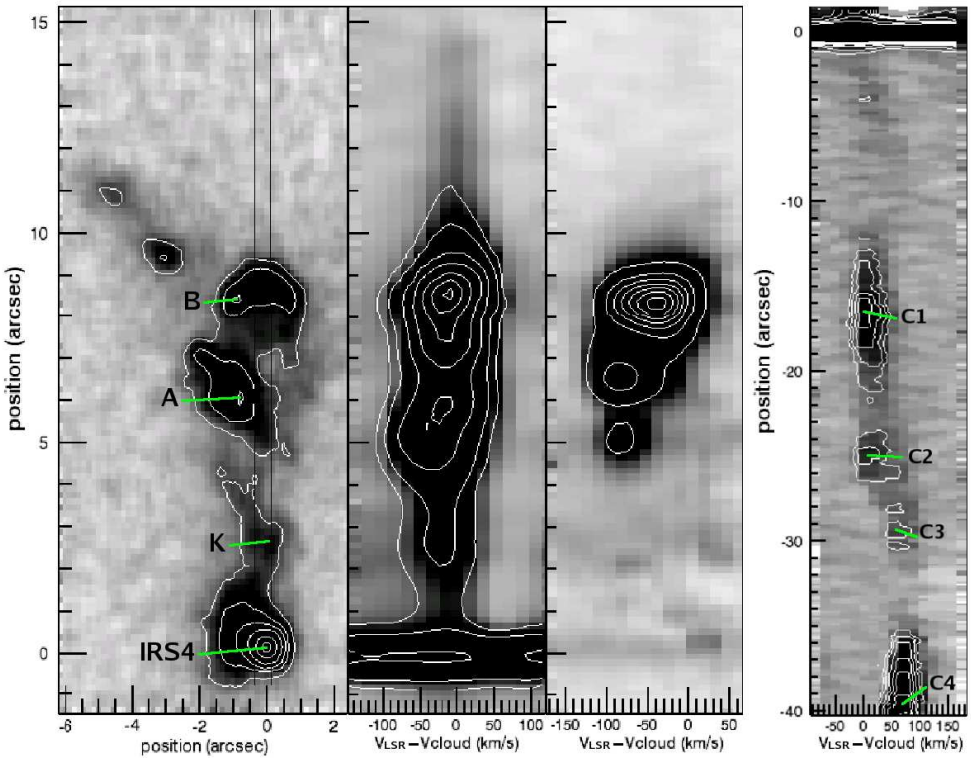

Figure 3.14: Left figure: a H_2 continuum-subtracted narrow band image (left panel), a spectral image of the 1-0S(1) line at 2.12 μm (central panel) and a spectral image of the [FeII] line at 1.64 μm (right panel) are spatially aligned. The slit position is reported along the three knots (A and B, according to the nomenclature of Schwartz & Greene 2003, and knot K identified in this analysis) and the infrared source IRS4. Right figure: spectral image of the 1-0S(1) line in the symmetric region with respect to the exciting source IRS4 (counterjet). The spatial positions are with respect to IRS4 and the radial velocities are with respect to the velocity of the ambient cloud (V_{cloud} = 22.3 km s^{-1}, Pettersson 1984).

bright emissions at the A and B knot positions.

In these positions, a comparison between the [Fe II] and H_2 P-V diagrams points out that the two lines do not trace the same region, since a displacement in their emission peaks is observed. This suggests that the molecular and atomic emissions are generated from different and spatially distinct shock events.

For the analysis of the H_2 emission, 8 different apertures (corresponding to the individual knots) were selected at the positions of the emission peaks along the slit; the knots are reported in Table 3.5, together with the relative radial velocity and velocity dispersion (ΔV). The velocity spread was obtained as the gaussian FWHM of the line profile once corrected by instrumental broadening (see Section 2.2.1).

Figure 3.14 and the radial velocity values reported in Table 3.5 show that the knots

Table 3.5: Radial velocity and de-convolved velocity dispertion (ΔV) of the 1-0S(1) line in several HH120 knots. The radial velocity is with respect to the local cloud ($V_{cloud} = 22.3$ km s^{-1}, Pettersson 1984). In the C2 knot, two velocity components are identified. The peak positions are with respect to the position of exciting source IRS4.

Knot	Peak posotion (arcsec)	V_{LSR} - V_{cloud} [1] (km s^{-1})	ΔV [1] (km s^{-1})
C4	-38.7	66.3	27.8
C3	-29.8	63.5	< 14
C2	-24.9	4.1 (49.4)	< 14 (20.8)
C1	-16.9	7.0	31.3
IRS4	0	-17.1	22.8
K	2.4	-21.3	43.1
A	5.8	-28.4	57.1
B	8.6	-12.8	27.8

[1]The uncertainty on the radial velocity and the velocity spread is estimated around 3 km s^{-1}.

C1, C2, C3 and C4 are redshifted, while the K, A and B knots are blueshifted: this finding supports the hypothesis that IRS4 is the exciting source of the outflow (Pettersson 1984).

However we note that the kinematic behaviour of the blue-shifted and red-shifted knots is very different: in particular, we do not observe any symmetry both in the locations and in the radial velocities between the jet and the counterjet. Knots K, A and B are located within 10 arcsec from the driving source, while knots C extend up to 40 arcsec from IRS4. The radial velocity in the blue-shifted jet follows a pattern very similar to that observed in the H_2 jet of HH26IRS, i.e. the velocity firstly increases (up to 28 km s^{-1} in knot A) and then has a rapid deceleration down to 13 km s^{-1} at knot B. This rapid deceleration may represent a region of strong interaction with the surrounding medium, where the jet kinetic energy is converted to thermal energy, as also testified by an increase of the H_2 temperature (measured from the 2-1S(1)/1-0S(1) ratio) of $\sim$ 300 K going from knot K to knot B.

Knots C, on the contrary, show a different pattern: the jet starts at a low radial velocity (knot C1, $V \sim 7$ km/s) while in knot C2 an abrupt change in velocity is observed, with the appearance of a high velocity component ($V \sim$50 km/s) which is maintained also in knots C3 and C4 (see Figure 3.15). In addition, the higher velocity dispersion measured in the blue-shifted jet with respect to the red-shifted knots, suggest that the red-shifted knots experience a weaker interaction with the surrounding medium.

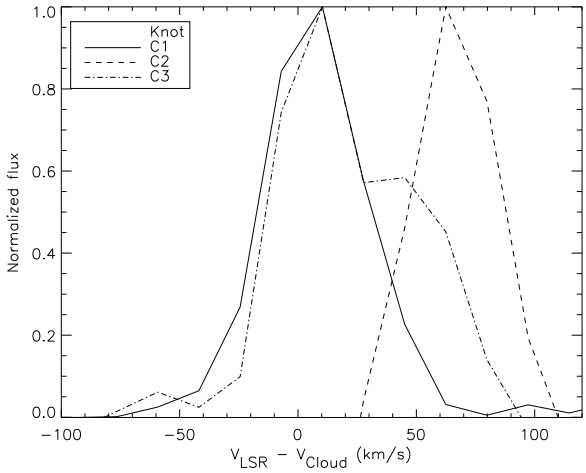

Figure 3.15: Comparison between the 1-0S(1) high resolution line profiles obtained for knot C1 (full line), C2 (dashed line) and C3 (dashed-dot line).

Given the complexity of the region where several H_2 jets are present with different orientations (see Figure 3.13), a possibility that cannot be ruled out is that the C redshifted knots are actually part of different flows, not related to the IRS4 source. Our single slit spectroscopy is not sufficient to disentangle this point.
At variance with the H_2 lines, the [Fe II] lines show a different, asymmetrical velocity profile, as can be seen in Figures 3.16. In both knots A and B two velocity

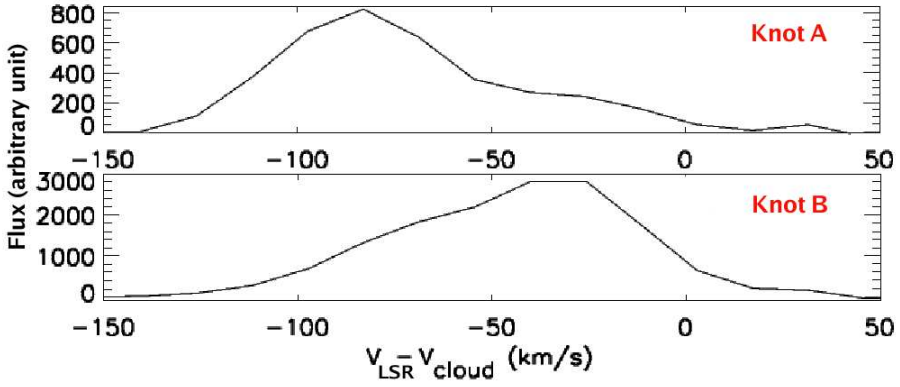

Figure 3.16: High resolution spectral line profile of the [FeII]1.644 μm transition observed in knot A (upper plot) and in knot B.

components can be identified, corresponding to the peak velocities V∼-83 km s^{-1} and V∼-40 km s^{-1}; in knot A, the intensity peak is at a higher velocity component, while the opposite is observed in knot B. This behaviour is consistent with the H_2 kinematic analysis, since the deceleration of the ionized component of the gas, which occurs between knots A and B, indicates the presence of a zone of strong interaction between jet and surrounding medium.

Shock velocity and electron density

The velocity resolved line profile of [Fe II] transitions at 1.64 μm and at 1.67 μm can be used to estimate the shock velocity and to measure the behaviour of the electron density (n_e) as a function of the observed radial velocities (see Sections 2.2 and Section 2.3.3).
If the emission from knots A and B is interpreted as a bow shock (see below) we can measure the bow head velocity (i.e. the shock velocity at the apex of the bow, see Section 2.2) from a direct measure of the FWZI of the line profile: this leads to $V_s \simeq 105$ km s^{-1}. Such a velocity is consistent with the bright observed [Fe II] lines, which imply the presence of high velocity dissociative shocks able to release most of the iron locked on grains in gaseous form.
The high resolution spectral profile of the 1.64μm and at 1.67μm lines allow us to perform a measure of the electron density for knots A and B in each velocity channel (see Section 2.3.3). The result is shown in Figure 3.17: each point

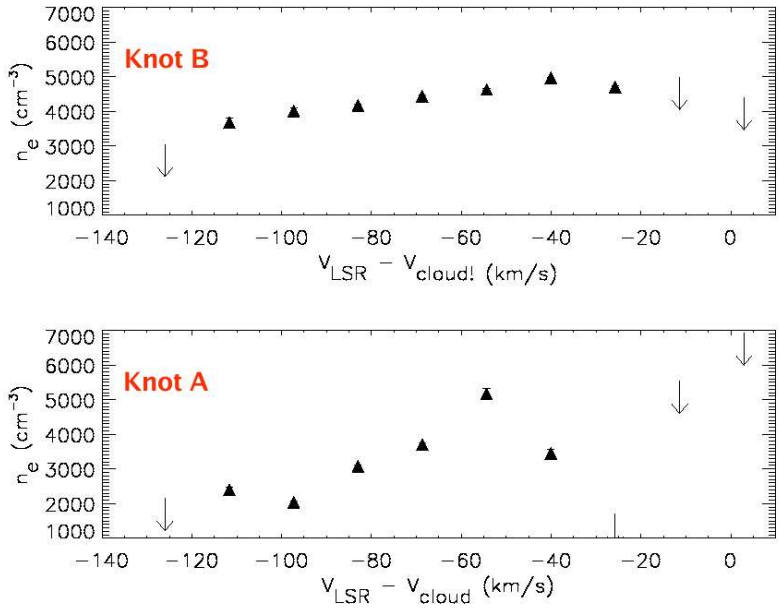

Figure 3.17: 1.67/1.64 [Fe II] line ratio, in each velocity channel, for the A and B knots in the HH120 region. The triangles are obtained by selecting data with S/N > 3, while arrows are upper limits. The errors of significant data points are within the triangle dimension.

represents the electron density obtained as the value averaged inside the velocity instrumental dispersion ($\Delta V = 18$ km s^{-1}) and the significant points (triangles) are those obtained by selecting data with S/N > 3.

The plots show how the n_e values decrease going from low to high velocity channels in both the investigated regions; this trend is more accentuated in knot A, where the density varies from $\sim 5\,10^3$ cm^{-3} at -50 km/s, to $\sim 2\,10^3$ cm^{-3} at -100 km/s.
This result is difficult to reconcile with a model of bow shock approaching the observer. In such a framework, and assuming a constant total density across the bow, the higher value of the electron density should be observed at the high velocity channels, where the most energetic shocks, corresponding to the bow head region, occur.
A different interpretation is given assuming that the high velocity components come from the jet axis and the low velocity component from the oblique shocks in the wings of the bow shock. In this case, the jet should be travelling in a region having a lower total density, while the oblique shock is impacting a high density region.
Again, this result points out how a single long-slit spectroscopy proves to be unsuited to describe a complex shock region such as a bow shock.

Bow shock morphology

In order to compare the 1-0S(1) line profile with the paraboloid model described in Section 2.2, we have integrated the emission of knots A and B intercepted by our slit obtaining the line profile shown in Figure 3.18.
The analysis, which is similar to the one exposed for the HH26A case, suggests that the overall symmetry of the profile is consistent with a parabolic bow shape shock, while the emission excess in the blue wing can be introduced by the long-slit observational setup which collects more emissions from regions close to the bow head.
Nevertheless, in this case the asymmetry is less accentuated with respect to the HH26 case, because of the higher bow velocity (105 km s^{-1}) measured in HH120 which is capable of dissociating the molecular hydrogen in the region close to the bow apex.

3.2.3 HH240

HH240/HH241 is a powerful bipolar outflow located in the dark cloud L1634 at a distance $\sim$ 460 pc (Bohigas et al. 1993)). It is emanated by the source IRAS 05173-0555 (α_{2000}=$05^h19^m48.9^s$, δ_{2000}=-05°52′05.0″) (Davis et al. 1997) . The blue-shifted lobe, namely HH240A, is shown in Figure 3.19, where the H_2 2.12

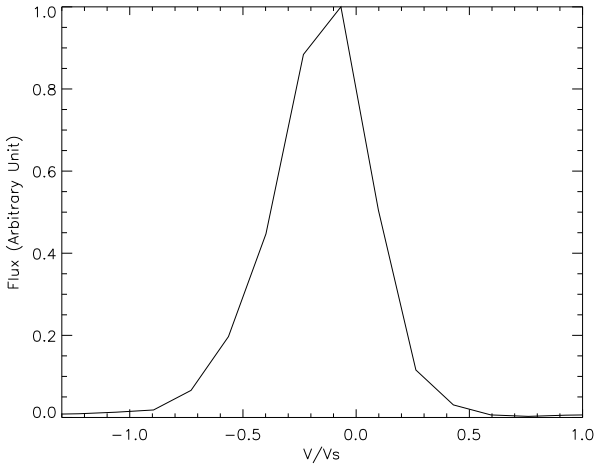

Figure 3.18: High resolution line profile of 2-1S(1) line at 2.12μm integrated in the A and B knots of the HH120 region. The observed radial velocities are normalized with respect to the bow velocity ($V_s = 105$ km s^{-1}), while the flux is normalized to the peak intensity.

μm image taken with SofI is depicted along with the ISAAC slit position adopted in our observation. Several extended bow shocks, which are labelled following the nomenclature of Davis et al. (1997), are displaced along the outflow axis and simmetrically distributed with respect to the driving source. Near-infrared imaging and spectroscopy of HH240A are reported by Nisini et al. (2002) and O'Connell et al. (2004) who have derived physical parameters of the shocked gas and interpreted the observed lines in the framework of a non-dissociative C-type shock.

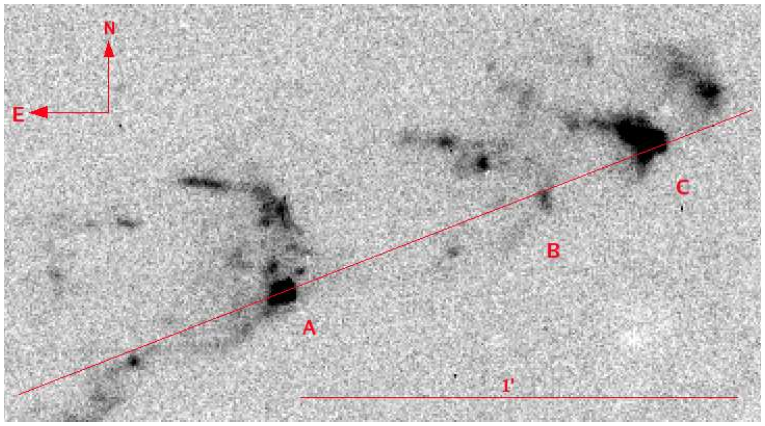

Figure 3.19: H_2 2.122μm image of the HH240 region taken with SofI-NTT (Nisini et al. 2002), superimposed with the ISAAC slit adpoted in our observations .

Observed lines

The HH240A spectra obtained in the low resolution mode both in J and H bands are displayed in Figures 3.20 and 3.21, where the spectral identification of the observed lines is indicated. Only this source was observed in the low resolution mode, providing a wide range of observed wavelengths which allows a large number of molecular hydrogen and atomic lines to be detected.
These lines are summarized in Table 3.6, where the spectral identification, the vacuum wavelength, the excitation energy and the integrated flux are reported. The latter was obtained by fitting the line shape with a single (or double in case of blended lines) Gaussian profile and the reported uncertainty derives from the root mean squared (rms) noise of the baseline multiplied by the width of the line profile.
The observed transitions are dominated by H_2 ro-vibrational lines (68 lines), including transitions coming from levels with $v \leq 7$ and E_{up} up to $\sim 45\,000$ K, many of them never yet observed in HH objects. A large number of atomic lines were detected: the majority are [Fe II] lines (20 lines) emitted from levels with E_{up} up to $\sim 30\,000$ K, while two hydrogen recombination lines and one [P II] line were observed.

H_2 emission

The high number of molecular hydrogen lines observed in HH240A in low resolution mode allows to investigate the excitation conditions of the molecular gas by the construction of the Boltzmann diagram (see Section 2.3.4) shown in Figure 3.22.
Such a diagram extends up to excitation energies of $\sim 35\,000$ K, thus substantially improving the one presented by Nisini et al. (2002), where E_{up} does not exceed 26 000 K. As in that case, the observed emission is well represented by a single straight line, but the fitted kinetic temperature ($T = 4\,190 \pm 130$ K) is noticeably higher (Nisini et al. 2002, measured $T=3\,400 \pm 200$ K). Hence, as in the case of HH26, our measurements demonstrate that H_2 can survive against dissociation at temperatures higher than those predicted in pure non-dissociative C-type shocks (see Section 2.1.3). We also note that, even if a single temperature can be inferred, a significant departure from the straight line is present among the data corresponding to the highest excited lines (E>25 000 K). This circumstance is predicted in C-type shocks in case of very strong magnetic fields (see Section 2.3.4). Indeed, the presence of a magnetic field acts to dampen and broaden the

Table 3.6: HH240A lines obseved in low resolution mode.

Line	λ_{vac} (μm)	E_{up} (K)	F $\pm\Delta$F (10^{-15} erg cm^{-2} s^{-1})	Line	λ_{vac} (μm)	E_{up} (K)	F $\pm\Delta$F (10^{-15} erg cm^{-2} s^{-1})
			H_2 lines				
1-0S(6)	1.7879	11522	5.58 ± 0.06	1-0S(9)	1.6877	15723	2.38 ± 0.05
1-0S(7)	1.7480	12818	9.04 ± 0.06	1-0S(10)	1.6665	17312	0.23 ± 0.05
1-0S(8)	1.7147	14221	1.76 ± 0.07	1-0S(11)	1.6504	18980	0.41 ± 0.05
2-0S(0)	1.1896	12095	2.73 ± 0.04	2-0Q(6)	1.2745	14764	0.71 ± 0.07
2-0S(1)	1.1622	12551	1.38 ± 0.15	2-0Q(7)	1.2873	15764	1.25 ± 0.1
2-0S(2)	1.1382	13151	0.97 ± 0.11	2-0Q(8)	1.3020	16881	0.47 ± 0.05
2-0S(3)	1.1175	13891	2.96 ± 0.12	2-0Q(10)	1.3375	19435	0.27 ± 0.10
2-0Q(1)	1.2383	11790	1.48 ± 0.06	2-0O(3)	1.3354	11790	1.38 ± 0.06
2-0Q(2)[1]	1.2419	12095	0.86 ± 0.06	2-0O(6)	1.4870	13151	0.25 ± 0.07
2-0Q(3)	1.2473	12551	1.52 ± 0.06	2-0O(7)	1.5464	13891	0.47 ± 0.09
2-0Q(4)	1.2545	13151	1.40 ± 0.09	2-0O(9)	1.6796	15764	0.28 ± 0.05
2-0Q(5)	1.2636	13891	1.90 ± 0.14				
3-1S(0)[2]	1.2621	17388	0.53 ± 0.06	3-1S(11)	1.1211	28558	0.43 ± 0.13
3-1S(1)	1.2330	17819	1.25 ± 0.06	3-1Q(1)	1.3141	17099	0.68 ± 0.05
3-1S(2)	1.2076	18387	0.66 ± 0.08	3-1Q(2)	1.3181	17388	1.00 ± 0.05
3-1S(3)	1.1857	19913	1.58 ± 0.04	3-1Q(3)	1.3240	17819	0.91 ± 0.05
3-1S(4)	1.1672	19913	0.98 ± 0.19	3-1Q(4)	1.3320	18387	0.41 ± 0.06
3-1S(5)	1.1519	20857	0.85 ± 0.14	3-1Q(6)	1.3541	19913	2.42 ± 0.14
3-1S(6)	1.1397	21912	0.49 ± 0.12	3-1Q(7)	1.3684	20857	1.26 ± 0.14
3-1S(7)	1.1304	23071	1.69 ± 0.16	3-1Q(11)	1.4479	25661	0.59 ± 0.29
3-1S(8)	1.1241	24323	0.46 ± 0.18	3-1O(5)	1.5220	17819	0.45 ± 0.07
3-1S(9)	1.1204	25661	0.75 ± 0.14				
4-2S(0)	1.3425	22354	0.96 ± 0.07	4-2S(7)	1.2047	27708	0.64 ± 0.08
4-2S(1)	1.3116	22760	0.61 ± 0.05	4-2S(8)	1.1987	28885	0.28 ± 0.05
4-2S(2)	1.2846	23296	0.11 ± 0.10	4-2S(9)	1.1958	30141	0.45 ± 0.08
4-2S(3)[3]	1.2615	23956	0.53 ± 0.06	4-2Q(6)	1.4432	24735	0.45 ± 0.10
4-2S(4)[4]	1.2422	24735	0.86 ± 0.06	4-2Q(7)	1.4592	25625	0.30 ± 0.07
4-2S(5)	1.2263	25625	0.70 ± 0.06	4-2O(3)	1.5099	22081	0.18 ± 0.04
4-2S(6)	1.2139	26618	0.82 ± 0.06	4-2O(7)	1.7563	23956	0.19 ± 0.06
5-3S(3)	1.3472	28500	0.49 ± 0.07	5-3Q(3)	1.5056	27376	0.31 ± 0.05
5-3S(5)	1.3107	30066	0.31 ± 0.05	5-3Q(5)	1.5286	28500	0.34 ± 0.06
5-3S(6)	1.2982	30997	2.39 ± 0.13	5-3Q(7)	1.5626	30065	0.37 ± 0.08
5-3S(7)	1.2894	32017	0.40 ± 0.13				
6-4Q(3)	1.6162	31663	0.23 ± 0.05	6-4O(3)	1.7326	31065	0.25 ± 0.06
7-3O(13)	1.1066	41561	0.33 ± 0.13	7-5S(4)	1.5400	37223	0.32 ± 0.051
7-4Q(15)	1.4146	45958	0.90 ± 0.14				
			Iron lines				
$a^4D_{7/2}$–$a^6D_{9/2}$	1.2570	11446	64.50 ± 0.06	$a^4D_{5/2}$–$a^4F_{5/2}$	1.8005	12074	3.92 ± 0.05
$a^4D_{7/2}$–$a^6D_{7/2}$	1.3209	11446	19.40 ± 0.05	**$a^4D_{3/2}$**–$a^6D_{3/2}$	1.2791	12489	5.46 ± 0.10
$a^4D_{7/2}$–$a^4F_{9/2}$	1.6440	11446	53.20 ± 0.05	$a^4D_{3/2}$–$a^4F_{7/2}$	1.5999	12489	5.10 ± 0.08
$a^4D_{7/2}$–$a^4F_{7/2}$	1.8099	11446	12.30 ± 0.07	$a^4D_{3/2}$–$a^4F_{5/2}$	1.7116	12489	1.40 ± 0.07
$a^4D_{5/2}$–$a^6D_{9/2}$	1.1916	12074	0.86 ± 0.05	$a^4D_{3/2}$–$a^4F_{3/2}$	1.7976	12489	2.51 ± 0.06
$a^4D_{5/2}$-$a^6D_{7/2}$	1.2489	12074	1.50 ±0.07	**$a^4D_{1/2}$**–$a^6D_{3/2}$	1.2525	12729	0.96 ± 0.07
$a^4D_{5/2}$–$a^6D_{5/2}$	1.2946	12074	7.75 ± 0.12	$a^4D_{1/2}$–$a^6D_{1/2}$	1.2707	12729	3.68 ± 0.10
$a^4D_{5/2}$–$a^6D_{3/2}$	1.3281	12074	3.60 ± 0.06	$a^4D_{1/2}$–$a^4F_{5/2}$	1.6642	12729	2.98 ± 0.05
$a^4D_{5/2}$–$a^4F_{9/2}$	1.5339	12074	7.63 ± 0.08	$a^4D_{1/2}$–$a^4F_{3/2}$	1.7454	12729	2.05 ± 0.08
$a^4D_{5/2}$–$a^4F_{7/2}$	1.6773	12074	5.73 ± 0.05	$b^4P_{5/2}$–$a^4P_{3/2}$	1.3971	29971	2.39 ± 0.06
			Other atomic lines				
3-5 (Paβ)	1.2822	151492	3.81 ± 0.10	[P II]$^2D_2$-$^3P_1$	1.1471	12764	0.85 ± 0.161
3-6 (Paγ)	1.0941	153420	1.29 ± 0.14				

[1] blends with 4-2S(4)
[2] blends with 4-2S(3)
[3] blends with 2-1S(0)
[4] blends with 2-QS(2)

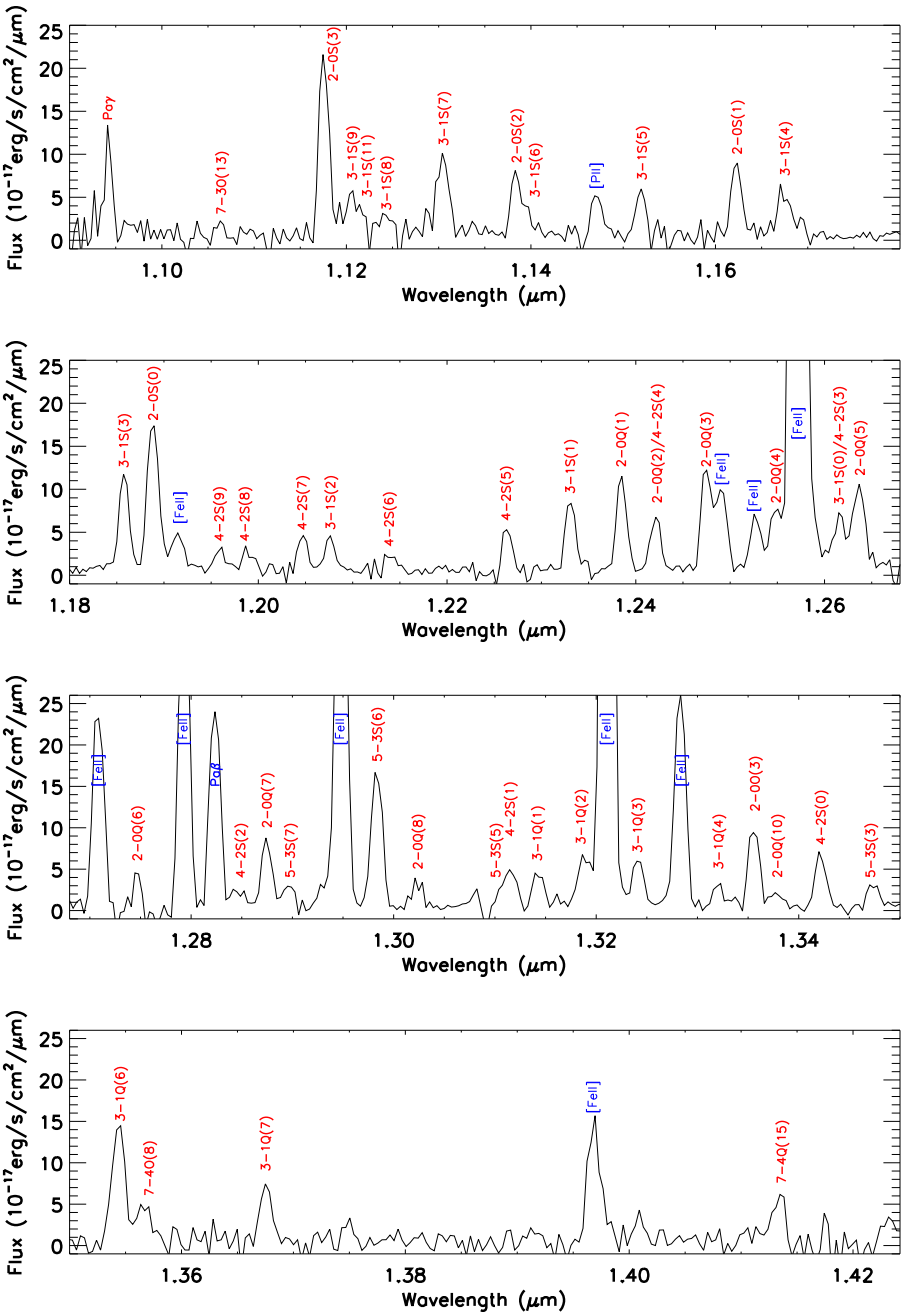

Figure 3.20: Low resolution spectra of HH240A: J band.

shock wave; therefore, an increased magnetic field strength enhances the departure from LTE. Thus, our Boltzmann diagram qualitatively confirms the intepretation of O'Connell et al. (2004), according to which the shock occurring in HH240A is a non-dissociative one with a magnetic field strength larger than 100 μG.

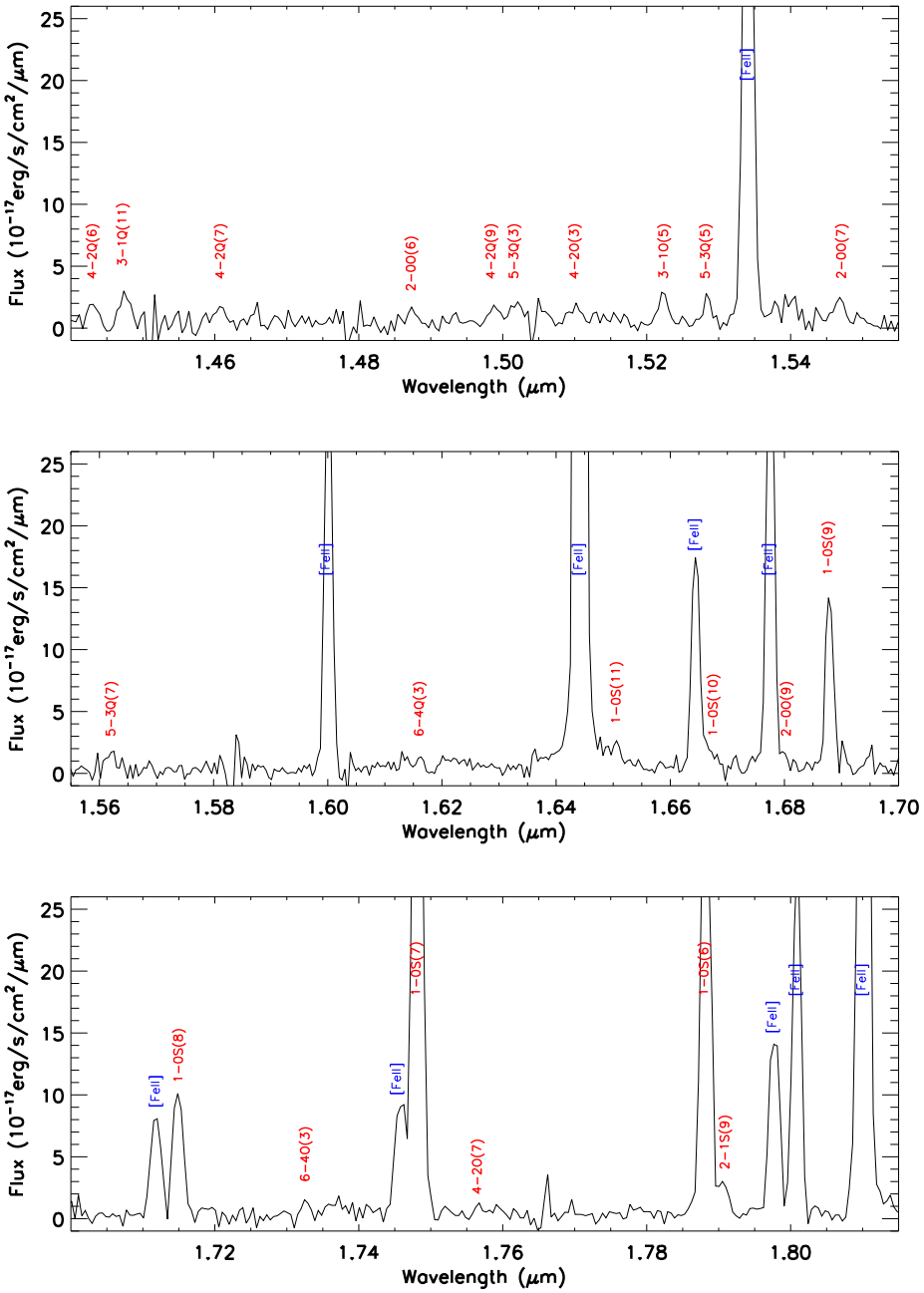

Figure 3.21: Low resolution spectra of HH240A: H band.

Atomic emission

Together with copious H_2 lines, we have detected strong ionic emission in HH240A, mainly in the form of [Fe II] lines (see Table 3.6 and Figures 3.20 and 3.21). This evidence demonstrates that the shocks occurring in the region are strong enough to efficiently disrupt the dust grains and hence to release iron in gas-phase.

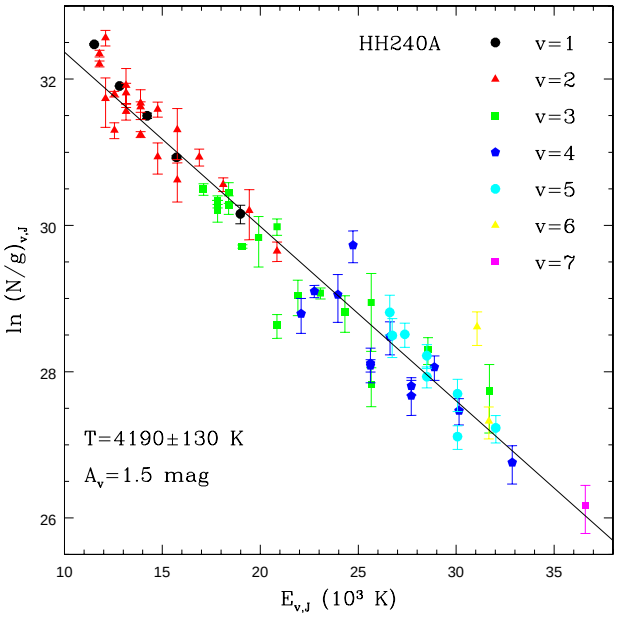

Figure 3.22: Boltzmann diagram of HH240A. Transitions coming from different vibrational levels are indicated with different symbols (from v=1 to v=7), to better represent the rotational series within the same vibrational level. The visual extinction value adopted to correct the observed line intensities is taken from Nisini et al. (2002).

To have a quantitative analysis of this effect, we have applied the method described in Section 2.3.3 to derive the percentage of the gas-phase iron (χ_{Fe}), by comparing the observed flux of a bright [Fe II] line with that of a non-refractory species. [P II] lines are well suited to this aim and the Fe/P abundance ratio can be directly derived by the following formula suggested by Oliva et al. (2001), once the fluxes have been de-reddened by extinction effects (we have assumed A$_V$=1.5 mag, as derived from the Boltzmann diagram):

$$\frac{n(\mathrm{Fe})}{n(\mathrm{P})} \simeq \frac{I([\mathrm{Fe\,II}]1.257)}{I([\mathrm{P\,II}]1.147)} \tag{3.1}$$

This method yields $\chi_{\mathrm{Fe\,II}}$ ∼0.76, a value that substantially confirms the estimate derived by Nisini et al. (2002) (χ_{Fe} ∼0.60) by using as a reference Paβ and [CI] lines. Such high efficiency is expected in violent shocks where the velocity is above 100 km s^{-1} (Jones 2000). Moreover, this result suggests that this kind of diagnostics can be successfully performed using NIR lines instead of optical lines. The obtained iron gas-phase percentage is suitable to perform a measure of the hydrogen fractional ionization x_e, by using the measured flux of the $Pa\beta$ line. In

fact, the intensity ratio between a [Fe II] line and the $Pa\beta$ is (see Section 2.3.3):

$$\frac{I_{[FeII]}}{I_{Pa\beta}} = \frac{\epsilon_{[\mathrm{Fe\,II}]}}{\epsilon_{Pa\beta}} \frac{n_{Fe^+}}{n_{H^+}} \tag{3.2}$$

and, assuming that iron is all single ionized, the ratio can be expressed as follows:

$$\frac{I_{[FeII]}}{I_{Pa\beta}} = \frac{\epsilon_{[\mathrm{Fe\,II}]}}{\epsilon_{Pa\beta}} \frac{\chi_{Fe}}{x_e} (Fe/H)_{\odot} \tag{3.3}$$

where $x_e = n_e/n_H$ and χ_{Fe} is the gas-phase iron fraction with respect to the solar Fe abundance.
Thus, considering the [Fe II] transition at 1.257 μm, the fractional ionization can be expressed from the Formula 3.3 as:

$$x_e = \chi_{Fe} (\mathrm{Fe/H})_{\odot} [\frac{[\mathrm{Fe\,II}]1.257}{Pa\beta}]^{-1} \frac{\epsilon_{[\mathrm{Fe\,II}]1.257}}{\epsilon_{Pa\beta}} \tag{3.4}$$

where $\epsilon_{Pa\beta}$ is taken from Storey & Hummer (1995), $\epsilon_{[\mathrm{Fe\,II}]1.257}$ is computed with a NLTE model assuming T=10 000 K and n_e=3 000 cm^{-3}, $(\mathrm{Fe/H})_{\odot}$ is taken from Asplund et al. (2005) and, finally, χ_{Fe} was estimated as $\delta_{\mathrm{Fe\,II}} \times (\mathrm{Fe/H})_{\odot}$.
We obtain x_e=0.45, a value consistent with those measured in Herbig-Haro objects where strong ionic emission is produced (x_e=0.03-0.6, Podio et al. 2006; Nisini et al. 2005).

3.3 Concluding remarks

In this Chapter we have presented long-slit NIR infrared spectra acquired in low and high resolution mode of a sample of HH objects. The high resolution profiles of molecular hydrogen and ionized iron lines and the detection of new molecular hydrogen lines, expecially with high excitation energies, and atomic lines, allow us to perform a deep analysis of these objects.
For every source, here we summarize the main results:

- HH26 is a low excitation region, as the faint detection of the [Fe II] line at 1.64 μm and the possible identification of a [SiI] line testify.
  A bow velocity of $\sim$ 60 km s^{-1} was measured from the line profile of the [Fe II] transition at 1.64 μm and the molecular gas shows a temperature stratification with the higher value of $\sim$ 4 700 K. These parameters are consistent with the J-type model with magnetic precursor developed by Giannini et al. (2004), showing as well that molecular hydrogen can survive at

temperatures greater than 3 000 K.
The high resolution H_2 lines reveal that HH26 jet represents an excellent example of the kinematic evolution of the flow from the exciting source (HH26IRS) up to the extended bow shock (HH26A). The observed knots belong to the blue-shifted lobe of the bipolar outflow generated by HH26IRS and are constituted by an accelerating microjet, which is located in a dense environment ($A_V = 15$ mag), followed by several decelerating knots, which end in a region with a small extinction value ($A_V \leq 2$ mag). Such deceleration corresponds to an enhancement of the gas temperature, which rises by ~ 600 K from the microjet to the external shock surface (HH26A).

- The morphology of H_2 and [Fe II] emission present in HH120 reveals the complexity of the region. The P-V diagrams show that molecular and atomic lines do not trace the same regions, suggesting that they are generated from different and spatially distinct shocks. The presence of bright [Fe II] lines and a measured shock velocity of ~ 105 km s^{-1} reveal that HH120 represents a region of strong interaction between the jet and the interstellar medium.
The analysis of the 1-0S(1) line shows blue-shifted (jet) and red-shifted (counterjet) knots distribuited with respect to the IRS4 source, which is considered the driving source of the outflow (Pettersson 1984). Nevertheless, the kinematic study does not show any symmetry both in the locations and in the radial velocities between jet and counterjet, suggesting that IRS4 may not be the source of the counterjet.
The electron density was measured in the observed velocity channels (n_e ranges from 2 to $5 \cdot 10^3$ cm^{-3}) showing a behaviour (higher at the low velocity component and lower at the high velocity component) that is difficult to reconcile with a model of a bow shock approaching the observer. A possible interpretation assumes that the high velocity component comes from the lower density region close to the jet axis, while the low velocity component comes from the oblique shock that, on the bow surface, impacts a higher density region.

- The low resolution spectra of HH240 show a high number of H_2 and [Fe II] lines. A single temperature of $\sim$4 200 K was measured for the molecular gas, intepreting the behaviour of the Boltzmann diagram in the framework of a fast C-type shock with a quite high magnetic field ($\sim 100\mu$G). Moreover the detection of a [PII] line and the hydrogen recombination lines allow to estimate the percentage of iron gas-phase (76%) and the hydrogen ionization

fraction (0.45); these values are consistent with HH objects where strong ionic emission is produced in violent shocks ($V_s > 100$km s^{-1})

As final consideration, the analysis of this sample of HH objects highlights a common result: slit spectroscopy of HH surces, because of its limitation of simultaneously reproducing the spectral behaviour of an extended region, provide several limitations in describing a complex shock region, such as a bow shock.
Therefore, in the next Chapter will be discussed the study of a bow shock observed with an innovative technique of investigation, which is able of dispersing radiation from each point of the observed field.

Chapter 4

IFU spectroscopy of HH99

In this Chapter we present the first deep near-infrared analysis of a prototype bow shock (HH99B) performed with the Integral Field Unit spectrograph SINFONI. This intrument offers a new and revolutionary way of studing protostellar shocks, since it is able to sample, at the same time, the physical conditions occurring along the entire bow shock surface. The study of HH99 was performed by inferring the physical and kinematic parameters of the bow shock, according to the methods exposed in Chapter 2.
The final aim of this study is to provide maps of physical parameters of a bow shock region and observational results able of constraining the development of new bi-dimensional models of bow shocks.

4.1 IFU spectroscopy with SINFONI

SINFONI, the acronym for Spectrograph for INtegral Observations in the Near Infrared (Eisenhauer et al. 2003; Bonnet et al. 2004), is a near-infrared integral field spectrograph fitted by an adaptive optics module located at the ESO Very Large Telescope at Cerro Paranal (Chile) (European Southern Observatory 1998). It is mounted on the Unit Telescope 4 (UT4), whose primary mirror has a diameter of 8 meters.
The spectrograph operates with four gratings which select the radiation in J, H, K, H+K bands, providing a spectral resolution of around 2 000, 3 000, 4 000 and 1 500 respectively, each wavelength band fitting on the 2048 pixels of an Hawaii detector in the dispersion direction.
SINFONI is the result of the coupling of two sub-modules: the SINFONI Adaptive Optics module (SINFONI AO) and the Integral Field Unit (IFU) SPIFFI (the acronym for SPectrometer for Infrared Faint Field Imaging).

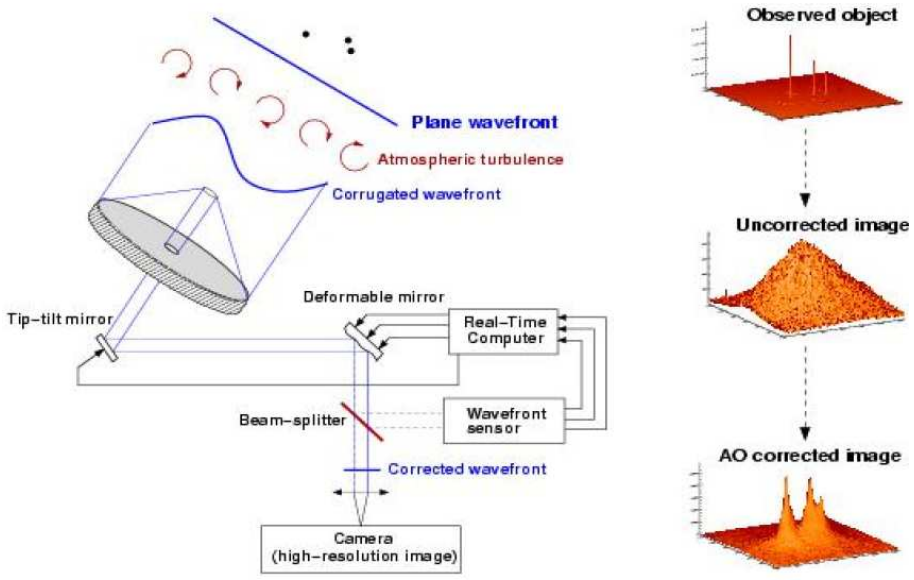

Figure 4.1: Schematic representation of adaptive optics: the wavefront sensor detects the wavefront distortions which are processed by a real time computer. This latter controls the piezoelectric actuators that push and pull on the back of the deformable mirror to compensate for the wavefront distortions (SINFONI User's Manual).

The SINFONI AO module is a Multi-Application Curvature Adaptive Optics (MACAO) system which overcomes the degrading effects of atmospheric turbulence by a feed back mechanism (see Figure 4.1): a real time measure of wavefront distortions allows for a real time adjustment of the deformable mirror to be performed, which compensates the wavefront distortions, providing images close to the diffraction limit of the telescope[1]. The IFU is a unit that splits the bidimensional field of view into a certain number of strips and recombines them into a one-dimensional pseudo-longslit, which is then passed through a spectrograph. In this way, the light of each pixel in the two-dimensional field of view is dispersed at the same time. Consequently, the two-dimensional spatial information, together with spectral information, is used to create a 3D data cube, which represents the dispersion of the whole field of view along the spectral domain (see Figure 4.2). Moreover the IFU spectroscopy allows the extraction of classical 2D spectra at a given point in the field of view.

In the SPIFFI instrument, the IFU spectrometry is performed by an image-slicer, a system consisting of two sets of plane mirrors (see Figure 4.3). The first set of mirrors, called Small Slicer, is located at the focus of the pre-optics and it consists of a stack of 32 mirrors which slice the image into 32 slitlets in different directions (see the sub-panel in Figure 4.3). The second set of mirrors, called Big Slicer,

[1]The angular size of the diffraction image of a common telescope in given by $\theta = 1.22\,\lambda/D$, where D is the telescope diameter.

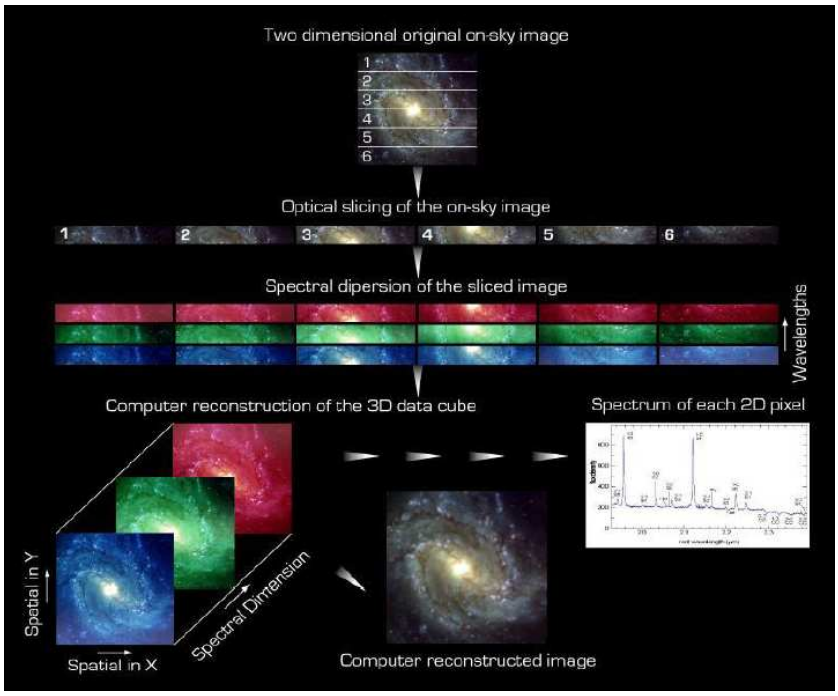

Figure 4.2: IFU spectroscopy. The field of view is split into slices which are recombined into a pseudo slit before being dispersed. During the data reduction the two-dimensional spatial information, together with the spectral information, are used to create a 3D data cube. Moreover a 2D spectrum can be extracted at a given position of the field of view (SINFONI User's Manual).

collects the light of 32 slitlets coming from the Small Slicer and rearranges them forming the pseudo long-slit.

Figure 4.4 shows how the 32 slitlets are imaged on the 2048 × 2048 pixels detector; each slitlet is imaged into 64 pixels, providing a simultaneous spectroscopy of $32 \times 64 = 2048$ spatial pixels (called "spaxels") of the considered field of view.

The pre-optics configuration allows to select the angular size of the slices on the sky; the choices are 250 mas, 100 mas and 25 mas, yielding a field of view of $8'' \times 8''$, $3.2'' \times 3.2''$, $0.8'' \times 0.8''$ respectively. The angular dimensions of the spaxels, which are rectangular, are determined by the chosen plate-scale (125 mas×250 mas, 50 mas×100 mas, 12.5 mas×25 mas, respectively for the reported fields of view) and they represent the spatial resolution elements of the system.

4.2 The region

Here we present the spectral images obtained with the IFU facility SINFONI of a prototype bow shock, namely the Herbig-Haro object HH99B, located in the RCrA molecular core at d∼130 pc (Marraco & Rydgren 1981). It was first discovered in the optical bands by Hartigan & Graham (1987), suggesting that it is

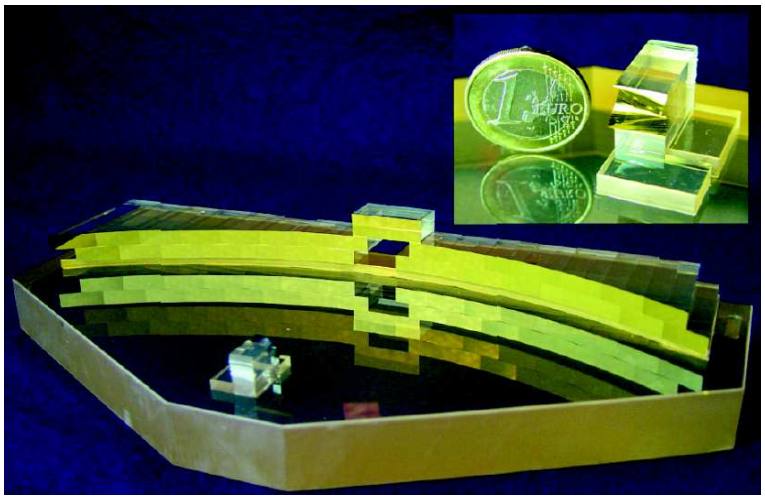

Figure 4.3: SPIFFI image slicer. The light is focused on the Small Slicer (sub-panel) entering through the hole located in the Big Slicer. The stack of 32 mirrors on the Small Slicer slices the image and reflects the light toward the 32 mirrors located on the Big Slicer, which re-arranges the slitlets into a single long pseudo slit (SINFONI User's Manual).

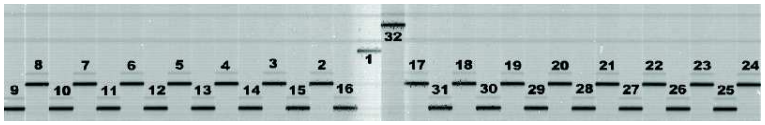

Figure 4.4: Positions of the slitlets on a raw SPIFFI frame. The spatial dimension of the pseudo slit lies on the horizontal direction, whereas on the vertical direction is the spectral dimension. Each slitlet is imaged into 64 pixels, thus simultaneous spectroscopy of 32×64 spatial elements (spaxels) is provided (SINFONI User's Manual).

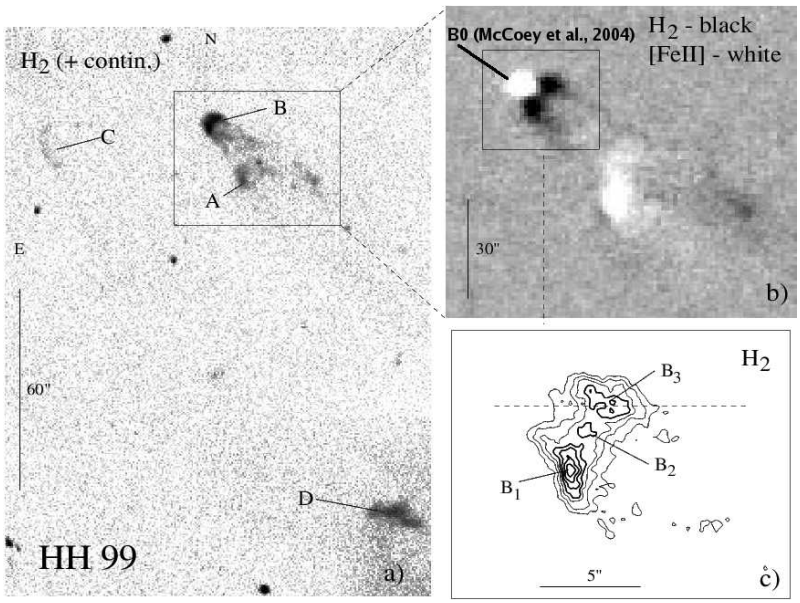

Figure 4.5: Panel a: H_2 (2.122 μm) + continuum image of HH99A and HH99B. The bow shock morphology is evident. Moreover, knots C and D are reported. Panel b: combined H_2 2.122μm and [Fe II] 1.644μm of HH99A and HH99B. The B0 knot identified by McCoey et al. (2004) is reported. Panel c: identification of knots B1, B2, B3 of HH99B bow shock on the 2.122 μm contour plot (Davis et al. 1999).

the red-shifted lobe of the outflow powered by the HH100-IR source.
HH99B was first imaged in the near-infrared bands by Davis et al. (1999) (see Figure 4.5) who identified three different emission zones: one at the head of the bow (subsequently named B0 by McCoey et al. 2004) where the bulk of the emission comes from ionized gas, and two bow-flanks (knots B1 and B3), which emit mainly in H_2 lines. A further H_2 knot, immediately behind the bow apex, was identified as knot B2.
HH99B was observed in near-infrared bands (J, H, K) during four different runs between May and July 2006. The total integration time is 2400 s, 1500 s and 1800 s in J, H and K bands, respectively. The spatial resolution was selected at $0.25''$ per image slice, which corresponds to a field of view of $8'' \times 8''$. No adaptive optics are supported in this configuration.

4.3 Reduction and results

4.3.1 Data reduction

SINFONI data reduction pipeline (Modigliani, Ballester & Peron 2007) has been applied to subtract the sky emission, to construct dark and bad pixel maps and flat field images, to correct for optical distortions and to measure wavelength

calibration by means of Xenon-Argon lamp images. Further analysis has been carried out with IRAF packages and IDL scripts, that were used to remove telluric absorption features and to perform photometric calibration (see SINFONI User's Manual: www.eso.org/instruments/sinfoni/doc/).
Atmospheric OH lines were used to refine wavelength calibration and measure the effective spectral resolution: this yields $R\sim$ 1 900, 2 700, 3 500 in J, H and K bands, that correspond to 160, 110, 85 km s^{-1}, respectively. At these spectral resolutions, we are able to resolve the brightest lines (e.g. H_2 2.122μm and [Fe II] 1.257μm), which are observed at S/N ratio of $\sim 10^2 - 10^3$.
As a final step, the brightest lines observed in each individual band ([Fe II]1.257μm and 1.644μm in J and H bands and H_2 2.122μm in K band) were used to re-align the images acquired in different dates.

4.3.2 HH99B line images and spectra

As a result, a 3D data cube was obtained, containing the HH99B image in more than 170 lines.
Furthermore, bi-dimensional spectra were obtained at the positions of B0 and B3 knots, that is integrating the signal in the areas reported in Figure 4.7 (A and C panels). Bi-dimensional spectra in the J, H and K bands are reported in Figure 4.6, where the behaviours of the spectra obtained in a flank region (B3 knot, black specta) and in the head region (B0 knot, red spectra) are compared.
The large majority of the detected lines are H_2 ro-vibrational lines (121 lines). For these, the spectral identification, vacuum wavelength, excitation energy (in K) and maximum signal-to-noise ratio (S/N) registered in the correspondig image are listed in Table 4.1.
The detected H_2 ro-vibrational transitions come from levels with $v \leq 6$ and E_{up} up to $\sim$ 38 000 K, many of them never observed before in HH objects. In particular, as shown in Figure 4.7 (upper panels), emission of lines with $E_{up} \leq$ 30 000 K is present only along the bow flanks, while lines with $E_{up} \geq$ 30 000 K are observed in the whole shock, reaching a peak at the bow head.
Therefore, two main results emerge:
(i) molecular hydrogen also survives where ionic emission is strong (see below) and,
(ii) temperature gradients do exist along the shock, with the highest values being reached at the bow head, where stronger excitation conditions are expected to occur.
Atomic lines are listed in Table 4.2 and some examples of the observations are

shown in Figure 4.7 (middle and bottom panels). Plenty of [Fe II] lines are detected (34 lines), emitted from levels with $E_{up} \leq 30\,000$ K. As in the case of H_2, two groups of lines are highlighted: those with $E_{up} \leq 13\,000$ K, which come from the a^4D level, are observed in the entire region, while those at a higher excitation energy are emitted only at the bow head.

In this same area, emission of hydrogen and helium recombination lines (8 and 4 lines, respectively, see Figure 4.7, bottom panels) along with fine structure lines of [P II],[Co II] and [Ti II], are detected.

Other fine structure lines commonly observed in Herbig-Haro objects (e.g. lines of [C I],[N I],[S II], e.g. Nisini et al. 2002) are not observable because of the shorter wavelength coverage of SINFONI compared with that of other infrared spectrographs (e.g. ISAAC and SofI at ESO).

Table 4.1: H_2 lines observed in HH99B *(to be continued).*

H_2 lines											
Line id.	λ_{vac} (μm)	E_{up} (K)	S/N[a]	Line id.	λ_{vac} (μm)	E_{up} (K)	S/N	Line id.	λ_{vac} (μm)	E_{up} (K)	S/N
					v=1						
1-0S(0)[1]	2.2233	6471	44	1-0S(7)	1.7480	12818	65	1-0S(21)[3]	1.7195	38136	7
1-0S(1)	2.1218	6951	650	1-0S(8)	1.7147	14221	70	1-0S(23)	1.7801	42122	4
1-0S(2)	2.0338	7584	48	1-0S(9)	1.6877	15723	46	1-0Q(1)	2.4066	6149	44
1-0S(3)	1.9576	8365	46	1-0S(10)	1.6665	17312	9	1-0Q(2)	2.4134	6471	30
1-0S(5)[2]	1.8358	10342	5	1-0S(18)[3]	1.6586	32136	3	1-0Q(3)	2.4237	6951	50
1-0S(6)	1.7879	11522	30	1-0S(19)[3]	1.6750	34131	8	1-0Q(4)	2.4375	7584	18
					v=2						
2-0S(0)	1.1896	12095	6	2-0Q(8)	1.3020	16881	9	2-1S(1)	2.2477	12551	44
2-0S(1)	1.1622	12551	48	2-0Q(9)[5]	1.3188	18108	12	2-1S(2)	2.1542	13151	22
2-0S(2)	1.1382	13151	7	2-0Q(10)	1.3375	19436	3	2-1S(3)	2.0735	13891	40
2-0S(3)	1.1175	13891	6	2-0Q(15)	1.4648	27267	3	2-1S(4)	2.0041	14764	21
2-0S(4)	1.0998	14764	6	2-0Q(19)[3]	1.6156	34447	3	2-1S(5)	1.9448	15764	30
2-0Q(1)	1.2383	11790	14	2-0O(2)	1.2932	11636	7	2-1S(8)[6]	1.8183	19435	7
2-0Q(2)[4]	1.2419	12095	9	2-0O(3)	1.3354	11790	16	2-1S(9)[7]	1.7904	20855	22
2-0Q(3)	1.2473	12551	22	2-0O(6)	1.4870	13151	5	2-1S(10)	1.7688	22356	3
2-0Q(4)	1.2545	13151	7	2-0O(7)	1.5464	13891	8	2-1S(15)[8]	1.7387	30794	6
2-0Q(5)	1.2636	13891	11	2-0O(9)	1.6796	15764	5	2-1S(17)[3]	1.7587	34446	4
2-0Q(6)	1.2745	14764	7	2-0O(11)	1.8349	18108	3	2-1S(18)[3]	1.7753	36301	3
2-0Q(7)	1.2873	15764	9	2-1S(0)	2.3556	12095	10	2-1S(19)[3,9]	1.7962	38166	8
					v=3						
3-1S(0)[10]	1.2621	17388	9	3-1S(9)	1.1204	25661	22	3-1O(5)	1.5220	17819	10
3-1S(1)	1.2330	17819	10	3-1Q(1)	1.3141	17099	8	3-1O(7)[14]	1.6453	19087	9
3-1S(2)	1.2077	18387	8	3-1Q(2)[12]	1.3181	17388	12	3-1O(9)[11]	1.7898	25661	10
3-1S(3)	1.1857	19087	9	3-1Q(3)	1.3240	17819	8	3-2S(1)	2.3864	17819	8
3-1S(4)	1.1672	19913	8	3-1Q(5)[13]	1.3420	19087	9	3-2S(2)	2.2870	18387	9
3-1S(5)	1.1520	20857	10	3-1Q(11)	1.4479	25661	8	3-2S(3)	2.2014	19087	25
3-1S(6)	1.1397	21912	5	3-1Q(13)	1.5024	28558	6	3-2S(4)	2.1280	19913	11
3-1S(7)	1.1304	23071	7	3-1Q(15)[3]	1.5685	31691	6	3-2S(5)	2.0656	20857	17
3-1S(8)	1.1241	24323	5	3-1O(4)	1.4677	17388	6	3-2S(7)	1.9692	23071	14

Table 4.1: H_2 lines observed in HH99B *(continued)*.

H_2 lines										
Line id.	λ_{vac} (μm)	E_{up} (K)	S/N[a]	Line id.	λ_{vac} (μm)	E_{up} (K)	S/N	Line id.	λ_{vac} (μm)	E_{up} (K)	S/N
					v=4						
4-2S(0)[15]	1.3425	22354	9	4-2S(8)	1.1987	28885	7	4-2O(4)[18]	1.5635	22354	6
4-2S(1)	1.3116	22760	14	4-2S(9)	1.1958	30141	6	4-2O(5)	1.6223	22760	7
4-2S(2)	1.2846	23296	21	4-2Q(7)	1.4592	25625	6	4-2O(6)	1.6865	23297	4
4-2S(3)[16]	1.2615	23956	9	4-2Q(9)	1.4989	27708	7	4-2O(7)	1.7563	23956	7
4-2S(4)[17]	1.2422	24735	9	4-2Q(11)[3]	1.5495	30141	3	4-3S(3)	2.3445	23956	6
4-2S(5)	1.2263	25625	12	4-2Q(13)[3]	1.6123	32857	6	4-3S(4)	2.2667	24735	3
4-2S(6)	1.2139	26618	5	4-2Q(15)[3]	1.6892	35786	6				
4-2S(7)	1.2047	27708	10	4-2O(3)	1.5099	22081	6				
					v=5						
5-3S(3)	1.3472	28500	4	5-3Q(1)	1.4929	26737	3	5-3Q(7)[3,19]	1.5626	30065	6
5-3S(4)	1.3270	29231	3	5-3Q(2)	1.4980	26994	9	5-3Q(11)[3]	1.6673	34291	4
5-3S(5)	1.3107[3]	30066	4	5-3Q(4)	1.5158	27880	5	5-3Q(12)[3]	1.7021	35529	4
5-3S(7)	1.2894[3]	32017	7	5-3Q(6)	1.5443	29230	3	5-3Q(13)[3]	1.7412	36821	5
					v=6						
6-4S(1)[3]	1.5015	31664	3	6-4Q(7)[3]	1.6829	34175	5	6-4O(4)[3,21]	1.7965	31306	8
6-4Q(3)[3]	1.6162	31664	5	6-4Q(9)[3,20]	1.7369	35992	6				
					v=7						
7-5Q(5)[3]	1.7784	36591	3								

Notes: [a]maximum signal-to-noise ratio in the line image. In case of blends the reported number refers to the sum of the blended lines (unless the emission comes from different zones of the bow).

[1] blends with [Fe II] $a^2H_{11/2}$-$a^2G_{9/2}$
[2] contaminated by atmospheric absorption
[3] detected in the whole bow
[4] blends with 4-2S(4)
[5] blends with 3-1Q(2)
[6] blends with HI 4-9
[7] blends with 3-1O(9)
[8] blends with 6-4Q(9), HI4-10
[9] blends with 6-4O(4)
[10] blends with 4-2S(3
[11] blends with 2-1S(9)
[12] blends with 2-0Q(9)
[13] blends with 4-2S(0)
[14] blends with [Fe II] $a^4D_{7/2}$−$a^4F_{9/2}$
[15] blends with 3-1Q(5)
[16] blends with 3-1S(0)
[17] blends with 2-0Q(2)
[18] blends with 5-3Q(7)
[19] blends with 4-2O(4)
[20] blends with 2-1S(15), HI 4-10
[21] blends with 2-1S(19)

Table 4.2: Ionic lines observed in HH99B.

Ionic lines							
Line id.	λ_{vac} (μm)	E_{up} (K)	S/N[a]	Line id.	λ_{vac} (μm)	E_{up} (K)	S/N
[FeII] lines[b]							
$a^4D_{7/2}$−$a^6D_{9/2}$	1.2570	11446	700	**$a^4D_{1/2}$**−$a^6D_{3/2}$	1.2525	12729	20
$a^4D_{7/2}$−$a^6D_{7/2}$	1.3209	11446	130	$a^4D_{1/2}$−$a^6D_{1/2}$	1.2707	12729	24
$a^4D_{7/2}$−$a^4F_{5/2}$	1.9541	11446	7	$a^4D_{1/2}$−$a^4F_{5/2}$	1.6642	12729	18
$a^4D_{7/2}$−$a^4F_{9/2}$ [1]	1.6440	11446	720	$a^4D_{1/2}$−$a^4F_{3/2}$	1.7454	12729	21
$a^4D_{7/2}$−$a^4F_{7/2}$	1.8099	11446	99	**$a^4P_{5/2}$**−$a^4D_{5/2}$	1.9675	19387	20
$a^4D_{5/2}$−$a^6D_{9/2}$	1.1916	12074	7	$a^4P_{5/2}$−$a^4D_{1/2}$ [2]	2.1609	19387	5
$a^4D_{5/2}$−$a^6D_{7/2}$	1.2489	12074	17	**$a^4P_{3/2}$**−$a^4D_{7/2}$	1.7489	19673	9
$a^4D_{5/2}$−$a^6D_{5/2}$	1.2946	12074	70	**$a^4P_{1/2}$**−$a^4D_{5/2}$	1.8139	20006	62
$a^4D_{5/2}$−$a^6D_{3/2}$	1.3281	12074	42	**$a^2G_{9/2}$**−$a^4D_{7/2}$ [3]	1.2675	22797	7
$a^4D_{5/2}$−$a^4F_{9/2}$	1.5339	12074	30	**$a^2G_{7/2}$**−$a^4D_{7/2}$ [3]	1.1885	23552	16
$a^4D_{5/2}$−$a^4F_{7/2}$	1.6773	12074	157	**$a^2P_{3/2}$**−$a^4P_{5/2}$	2.0466	26417	4
$a^4D_{5/2}$−$a^4F_{5/2}$	1.8005	12074	35	$a^2P_{3/2}$−$a^4P_{3/2}$	2.1334	26417	5
$a^4D_{3/2}$−$a^6D_{3/2}$	1.2791	12489	41	$a^2P_{3/2}$−$a^4P_{1/2}$	2.2442	26417	4
$a^4D_{3/2}$−$a^6D_{1/2}$	1.2981	12489	23	**$a^2H_{11/2}$**−$a^2G_{9/2}$ [4]	2.2244	29265	21
$a^4D_{3/2}$−$a^4F_{7/2}$	1.5999	12489	46	**$a^2H_{9/2}$**−$a^2G_{9/2}$	2.0157	29934	10
$a^4D_{3/2}$−$a^4F_{5/2}$	1.7116	12489	13	$a^2H_{9/2}$−$a^2G_{7/2}$	2.2541	29934	5
$a^4D_{3/2}$−$a^4F_{3/2}$	1.7976	12489	36	**$b^4P_{1/2}$**−$a^4P_{3/2}$	1.1446	32242	4
H lines							
3-5 (Paβ)	1.2822	151492	21	4-11	1.6811	156499	6
4-14	1.5884	156999	3	4-10[5]	1.7367	156226	6
4-13	1.6114	156870	4	4-9[6]	1.8179	155855	6
4-12	1.6412	156708	6	4-7 (Brγ)	2.1661	154583	12
Other lines							
He I $^1S_0 - ^1P_1$	2.0587	246226	3	[Ti II]$a^2F_{5/2}$-$a^4F_{3/2}$ [10]	2.1605	6652	5
He I $^3D - ^3P$ [7]	2.0607	282101	8	[Ti II]$a^2F_{7/2}$-$a^4F_{9/2}$	2.2201	7040	5
He I $^3P_0 - ^3D$ [7]	1.9522	289992	5	[Ti II]$a^2D_{5/2}$-$a^4F_{5/2}$	1.1560	12570	3
He I $^1P_1 - ^1S_0$	2.0586	245901	3	[Ti II]$a^4P_{3/2}$-$b^4F_{7/2}$	1.2036	13506	3
[P II]$^2D_2$-$^3P_1$	1.1471	12764	5	[Ti II]$a^2P_{3/2}$-$b^4F_{3/2}$	1.1028	14340	3
[P II]$^2D_2$-$^3P_2$ [8]	1.1886	12764	16	[Ti II]$a^2H_{11/2}$-$a^2F_{/2}$	1.2695	17729	5
[Co II] b^3F_4-a^5F_5 [9]	1.5474	14119	5				

Notes: [a] maximum signal-to-noise ratio in the line image. In case of blends the reported number refers to the sum of the blended lines (unless the emission comes from different zones of the bow).
[b] Lines coming from the same upper level are grouped, and the first term of each group is evidenced with bold-face characters.

[1] blends with 3-1O(7)
[2] blends with [Ti II]$a^2F_{5/2}$-$a^4F_{3/2}$ (fundamental transition)
[3] blends with [P II]$^1D_2$-$^3P_2$
[4] blends with 1-0S(0)
[5] blends with 2-1S(15), 6-4Q(9)
[6] blends with 2-1S(8)
[7] multiplet
[8] blends with [Fe II] $a^2G_{7/2}$-$a^4D_{7/2}$
[9] tentative identification
[10] blends with [Fe II] $a^4P_{5/2}$−$a^4D_{1/2}$

4.4 Derivation of physical parameters

4.4.1 Fe analysis

[Fe II] Einstein coefficients

The large number of [Fe II] lines detected in HH99B (see Table 4.2), observed with a high signal-to-noise (S/N) ratio in a remarkably large fraction of pixels,

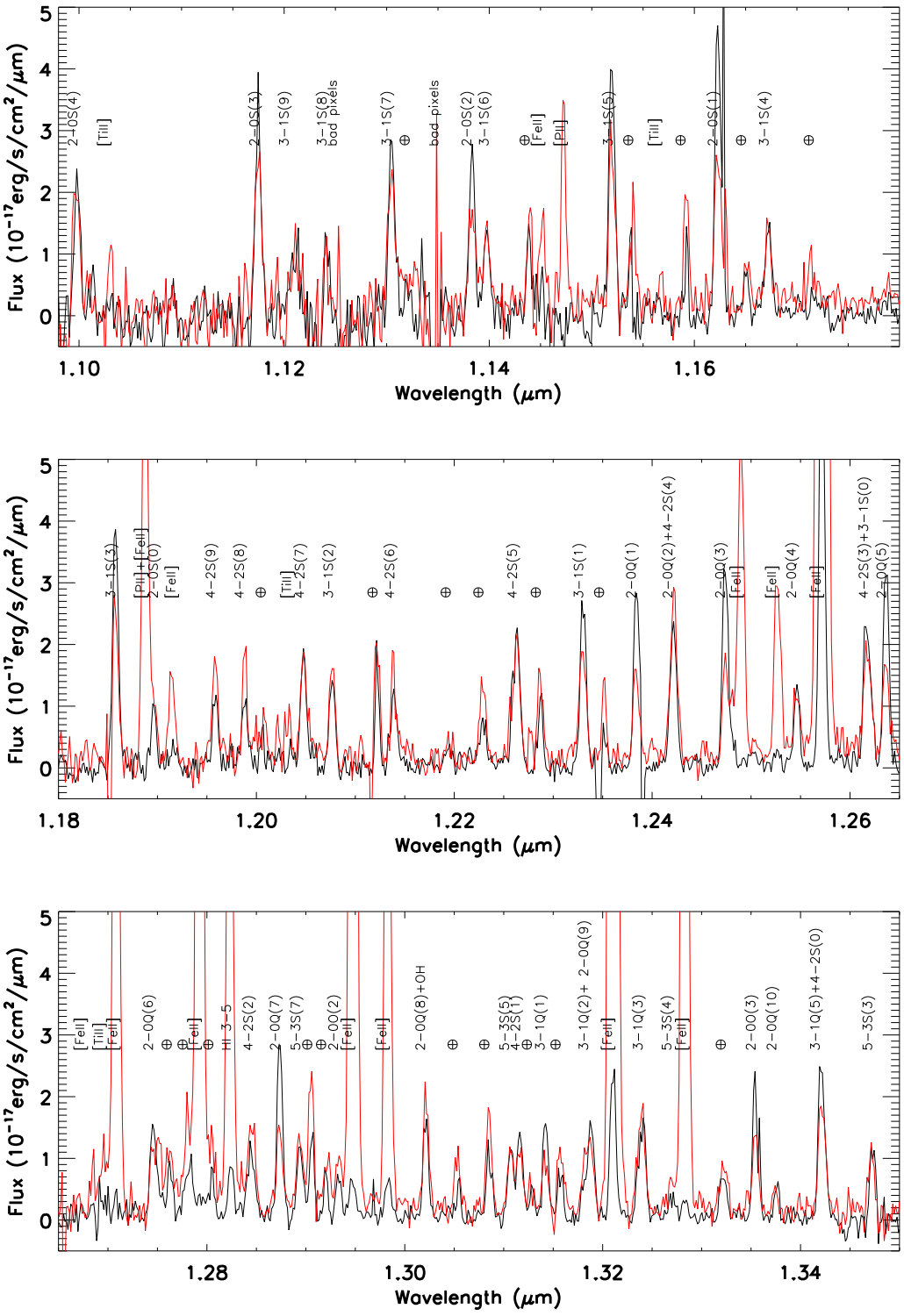

Figure 4.6: Bi-dimensional spectra of knot B3 (black lines) and knot B0 (red lines) acquired in J band. The regions selected for the spectral extraction are reported in Figure 4.7 (A and C panels). The $\oplus$ symbols mark the remnants of atmospherical OH lines

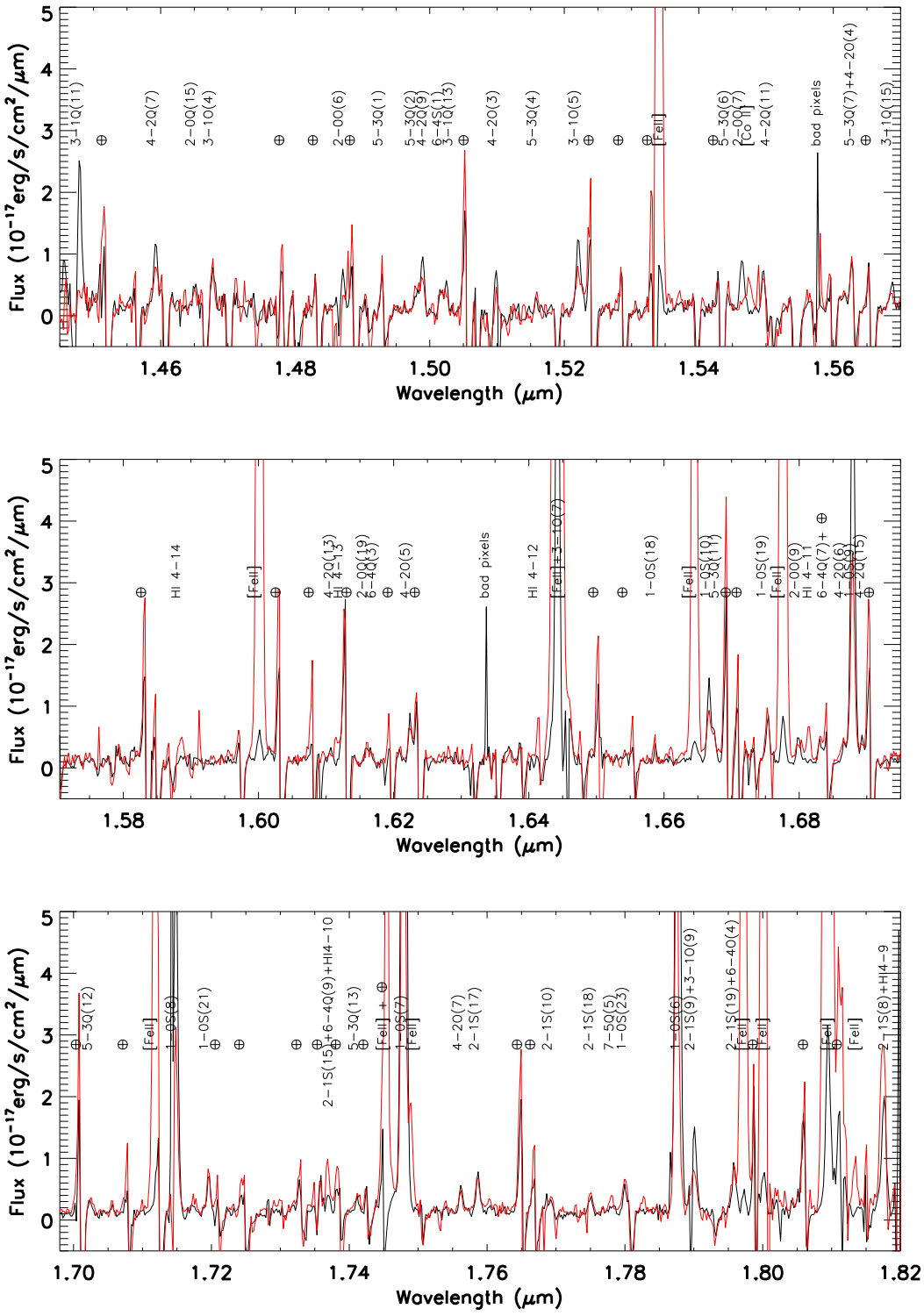

Figure 4.6: (b). As in Figure 4.7a for the H band.

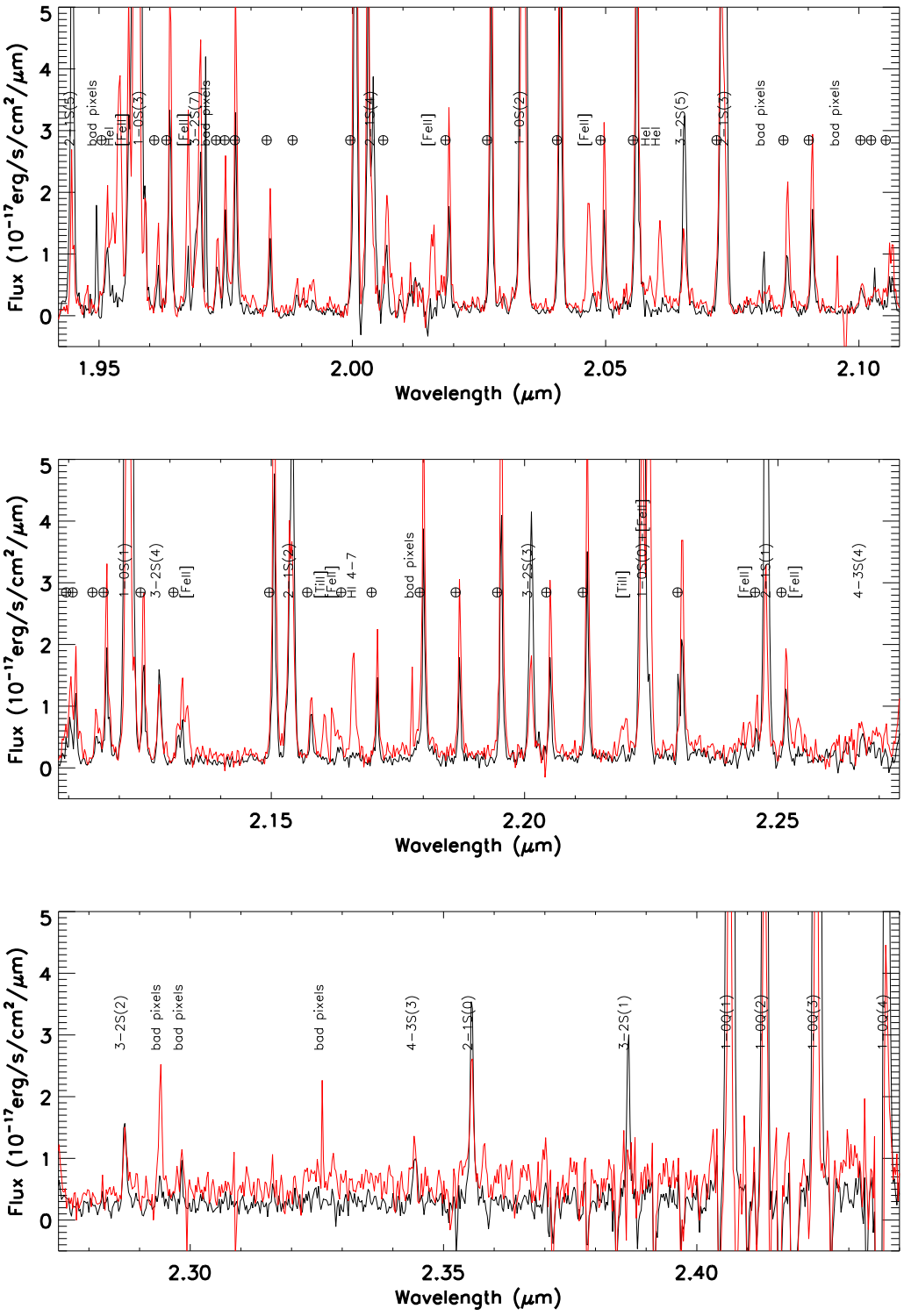

Figure 4.6: (c) As in Figure 4.7a for the K band.

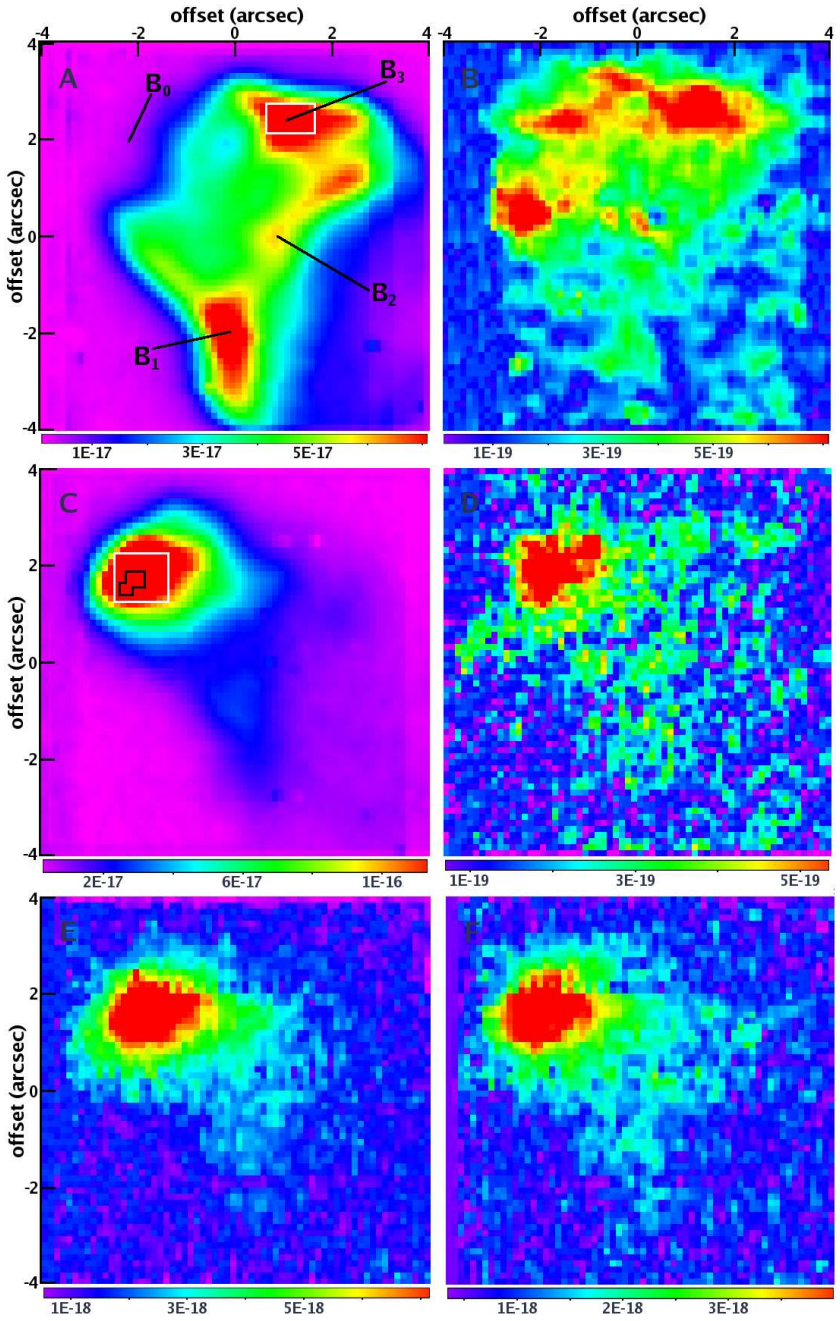

Figure 4.7: Examples of lines observed in HH99B. Intensities are given in colour scale. Offsets are respect to α_{2000}=$19^h02^m05.4^s$, δ_{2000}=-36°54′39″. A) H_2: 1-0 S(1) at 2.122μm; B) H_2: 2-1S(17) at 1.758μm; C) [Fe II]: 1.644μm ; D) [Fe II]: 1.749μm; E) H: Paβ; F) [P II]: 1.188μm. In panel A) the locations of the knots labelled by Davis et al. (1999) (B1, B2 and B3) and McCoey et al. (2004) (B0) and the area ($1'' \times 0.5''$) used to extract bi-dimensional spectra in the bow flank regions (white line) are indicated. In panel C) black line delimits the area where [Fe II] lines at S/N > 100 are detected and used to construct the plot of Figure 4.8, while the white line delimits the area used to extract bi-dimensional spectra in the bow head region ($1.125'' \times 1''$).

provides the opportunity to compare theoretical predictions on the spontaneous emission rates (Einstein A coefficients) with a significant sample of observational

points.
As discussed in Section 2.3.5, this issue is particularly important since a good determination of A values allows us to know the extinction properties of the observed region, and then to exactly correct the flux of the observed lines.
Among the numerous [Fe II] lines coming from the same level observed in HH99B, the ratios I(1.25μm)/I(1.64μm) vs I(1.32μm)/I(1.64μm) (all coming from the upper level $a^4D_{7/2}$) are plotted in Figure 4.8, since these are observed at very high S/N (larger than 100, red filled squares). In the same Figure, green dashed curves represent the Rieke & Lebofsky (1985) extinction law applied to the intrinsic ratios expected for the four sets of A coefficients (Quinet et al. 1996; Nussbaumer & Storey 1988; Smith & Hartigan 2006, see Section 2.3.5 or caption of Figure 4.8). Squares along these "extinction curves" indicate $A_V = 0$, 5, 10 mag.
First of all, all HH99B data lie definitively to the right of any of the plotted extinction curves. Since different A_V can move the points only *along* the extinction vectors, no theoretical intrinsic ratio is consistent with the observed points.
This result was already pointed out by Nisini et al. (2005), who discussed how the extinction along the knots of the HH1 jet determined from the 1.32μm/1.64μm ratio is always smaller than that derived from the 1.25μm/1.64μm ratio, irrespective of the adopted theoretical set of A coefficients.
HH99B data are also inconsistent with the P Cygni observational point (green triangle in Figure 4.8) and consequently with the A coefficients extrapolated from this point.
To check whether the SINFONI HH99B data set suffer from some observational or data reducing bias (e.g. unfavourable observational conditions, flat-fielding, removal of telluric features, intercalibration of lines lying in different bands), we searched in the literature for other observations of the considered lines obtained with different instruments. To minimize the uncertainties, only line ratios observed with a S/N $\geq$ 30 were considered, which are shown with different colours/symbols in Figure 4.8 (references are given in the Figure caption).
Noticeably, all of them occupy the right side of the plot, in agreement with the HH99B points. This result, which reinforces the reliability of the SINFONI observations, in principle allows to derive new A coefficients from SINFONI observational points, provided that these are accurately corrected for the visual extinction value.
In this respect, two facts have to be noted:
(i) although the sky area considered is a few arcsec^2 (marked in black in Figure 4.7, C panel), an extinction gradient of $\sim$ 1 mag occurs in this zone, as evidenced by the scatter among the data points (red squares) of Figure 4.8;

(ii) in the same area, a gross estimate of A_V (1.8±1.9 mag) can be obtained from the observed ratio Pα/Brγ (see Section 4.4.3).
Both these circumstances in practice prevent an accurate measure of the A ratios to be determined; however, for comparison with previous determinations, we have de-reddened the average of the HH99B data (black cross) for $A_V \sim 1.8$ mag, obtaining $A_{1.32}/A_{1.64} \sim 0.38$ and $A_{1.25}/A_{1.64} \sim 1.24$.
In conclusion, from a pure observational point of view, the following can be summarized:
(i) all the theoretically derived A values fail to reproduce the large majority of the observed line ratios, irrespective of the extinction values;
(ii) the best 'recipe' to derive a reliable extinction estimate from [Fe II] lines is (at least when only the three considered lines are detected) to use the NS coefficients for the I(1.32μm)/I(1.64μm) ratio and the Q-HFR coefficients for the I(1.25μm)/I(1.64μm) ratio, that are 8% and 5% respectively lower than the SINFONI determinations;
(iii) dedicated observations of objects with well known visual extinction should be performed to derive the [Fe II] Einstein A coefficients with sufficient accuracy.

Extinction map

Given the problems with A coefficients previously outlined, we have applied the following procedure to construct an extinction map along the HH99B bow from the observed [Fe II] lines (see Section 2.3.5): to minimize the effects of the uncertainties, a number of line ratios involving bright lines from four energy levels (i.e. $a^4D_{7/2}$, $a^4D_{5/2}$, $a^4D_{3/2}$, $a^4P_{5/2}$) and with wavelengths which are rather far apart from each other were selected.
With this set of ratios and, as a first attempt, adopting the Nussbaumer & Storey (1988) coefficients, the extinction in a very small region at the bow-head (where all the lines are detected with S/N ratio larger than 30) was determined. This value was then used to calibrate the extinction map obtained from the 1.25μm/1.64μm ratio only, which is the only one detected well above the noise level (at least at 5σ) also in the bow flanks.
Contours of the final map are shown in Figure 4.9: in a total area of $\sim 10\,\mathrm{arcsec}^2$ variations of A_V up to 4 mag are recognized. The highest A_V values (4-5 mag) are found close to the bow-head: if we correct the observed [Fe II] lines for these A_V values, the emission peak (see Figure 4.10) moves about 0.6 arcsec towards the NE direction.

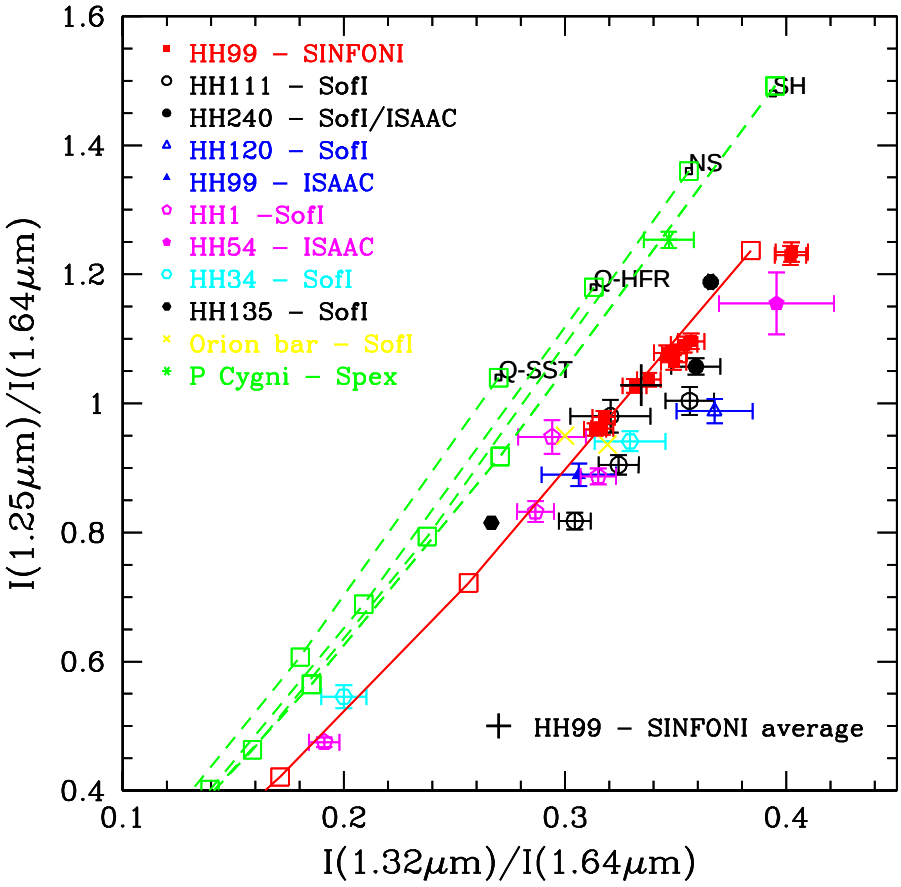

Figure 4.8: I(1.25μm)/I(1.64μm) vs I(1.32μm)/I(1.64μm) ratios measured in different objects (depicted with different symbols/colors). The HH99B-SINFONI data (red squares) have been computed in pixels where the S/N of each of the three lines is larger than 100, while other data are observations taken from existing literature where S/N $\geq$ 30. Intrinsic line ratios predicted theoretically (Q-SST = Quinet et al. (1996) - SuperStructure; Q-HFR = Quinet et al. (1996) - Relativistic Hartree-Fock; NS = Nussbaumer & Storey (1988)), along with the observational point (SH) by Smith & Hartigan (2006), are labelled. Green dashed curves represent the extinction law by Rieke & Lebofsky (1985), starting from different theoretical points; open squares refer to $A_V = 0, 5, 10$. The same extinction law (in red) has been applied to the $A_V = 0$ point derived from SINFONI data. This latter has been derived by applying to the average of the HH99B data (black cross) a visual extinction of 1.8 mag, as estimated from the Pα/Brγ ratio (see text). References: HH99B - SINFONI: this work; HH111-, HH240-, HH120-SofI: Nisini et al. (2002); HH240- ISAAC: Calzoletti et al. (2007) ; HH99B - ISAAC : McCoey et al. (2004) ; HH1 - SofI: Nisini et al. (2005) ; HH54 - ISAAC: Giannini et al. (2006) ; HH34 - SofI: Podio et al. (2006) ; HH135 - SofI: Gredel (2006) ; Orion bar - SofI: Walmsley et al. (2000) ; P Cygni - Spex: Smith & Hartigan (2006).

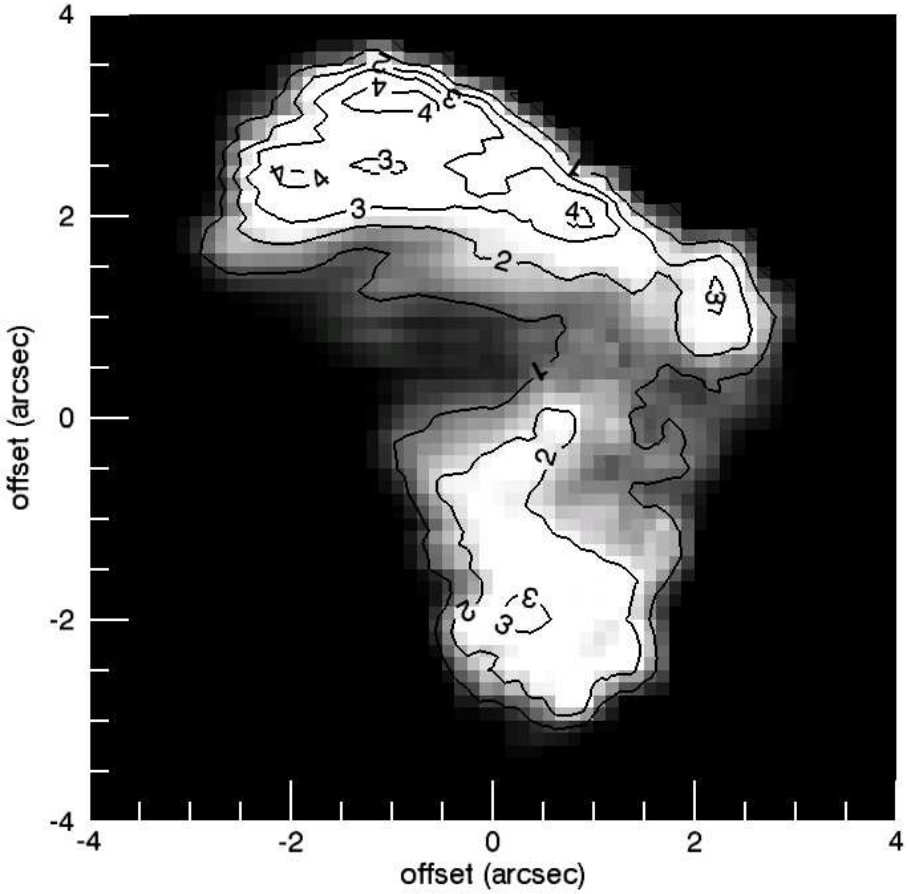

Figure 4.9: Extinction map obtained from [Fe II] lines where contours from A_V=1 mag to A_V=4 mag are shown.

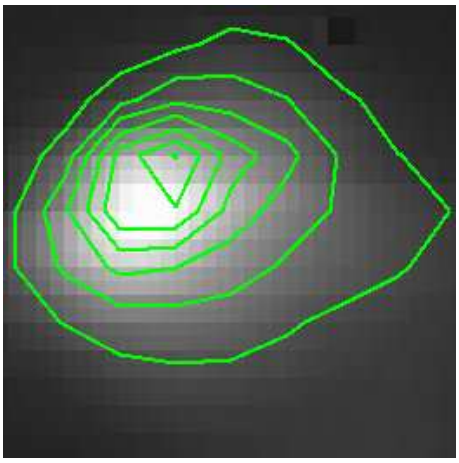

Figure 4.10: . De-reddened intensity contours of the [Fe II] line at 1.25μm, overlaid with the image acquired in the same line. Noticeably, the emission peak moves about 0.6 arcsec towards the NE direction.

Along the flanks, A_V is generally lower (up to 2-3 mag): thus, the progressive fading of the [Fe II] emission cannot be ascribed to an increasing extinction, but rather reflects low excitation conditions and low abundances in these zones of the gas-phase iron.
As described above, the main uncertainty on the extinction map arises from the adopted A values. We thus re-derived the same map from the 1.25μm/1.64μm ratio, now using the Einstein coefficients ratio of 1.24 previously computed. The largest difference between the two maps occurs at the emission peak, where it is of ~ 0.6 mag: this implies a marginal increase in intrinsic line intensities (for example I(1.64μm) increases up 10%) and does not critically affect the derivation (see below) of the physical parameters of the atomic gas. We note however that A_V estimates remain below the values inferred by McCoey et al. (2004) (A_V between 4 and 10 mag) obtained on the basis of the 1.25μm/1.64μm ratio, for which the NS coefficients were assumed.

Electron density map and temperature

To derive the electron density along the bow structure, we selected 7 intensity ratios (i.e. $I_{1.533}/I_{1.644}$, $I_{1.600}/I_{1.644}$, $I_{1.677}/I_{1.644}$, $I_{1.664}/I_{1.644}$, $I_{1.271}/I_{1.257}$, $I_{1.279}/I_{1.257}$, $I_{1.328}/I_{1.257}$), involving lines close in wavelength (their differential extinction is negligible) and coming from levels with different critical densities (from $\sim 8\ 10^2$ cm^{-3} to $3\ 10^5$ cm^{-3}) and similar excitation energy ($E_{up} \sim$ 11 000-12 000 K), so that the dependence on the temperature is very weak (see Sections 2.3.3).
All these line ratios were simultaneously fitted with a NLTE developed by Nisini et al. (2002) and described in Section 2.3.3, having assumed T=10 000 K.
As a result, we obtained the electron density map shown in Figure 4.11; n_e is typically of the order of 2-4 10^3 cm^{-3}, with a peak up to $6\,10^3$ cm^{-3} at the bow head; these values are in the range of those commonly found in HH objects (e.g. Nisini et al. 2005; Podio et al. 2006). This result shows that the most violent shocks, able to more efficiently ionize atoms, occur at the bow head region.
In a restricted area at the bow head of about 1 arcsec^2 (see Figure 4.7, middle right panel), 9 lines at high excitation (E_{up} between 20 000 and 30 000 K) were detected, that could be very suitable for evaluating the local electronic temperature. Of these, just four lines coming from the term a^{4}P (i.e. 1.749μm, 1.814μm, 1.967μm, 2.161μm[2]) can be modelled, since for the remaining five lines the collisional rates are unknown. To this aim, it was necessary to enlarge the 16 levels NLTE code normally used, by including three further fine structure levels, for

[2]The 2.161μm line has been de-blended from the fundamental line of [Ti II], by using a NLTE model for this species, described in Garcia Lopez et al. (2007).

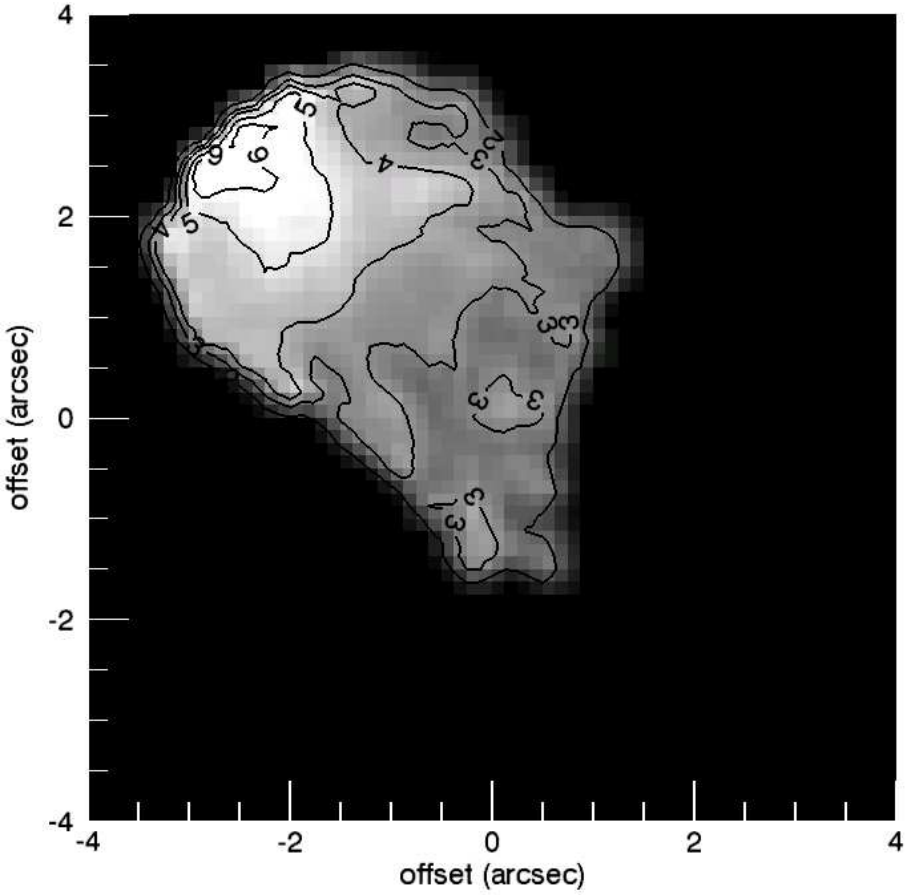

Figure 4.11: Electron density map as derived from [Fe II] line ratios. Contours are in units of 10^3 cm^{-3}.

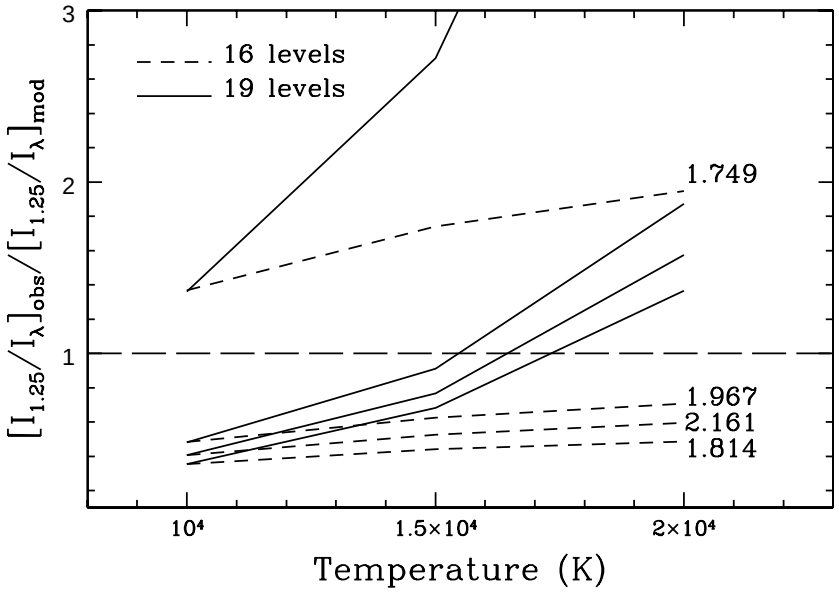

Figure 4.12: $[I_{1.25}/I_\lambda]_{obs}/[I_{1.25}/I_\lambda]_{mod}$ plotted vs the electronic temperature for four [Fe II] lines. The results for the Fe NLTE model at 16 and 19 levels are shown for comparison.

which the collisional coefficients are reported by Zhang & Pradhan (1995). Having fixed extinction and electron density from the maps of Figures 4.9 and 4.11, the observed (de-reddened) ratios were fitted with the 1.257μm line, integrated over the area where the a^4P lines were detected at S/N $\geq$5.

Results are plotted in Figure 4.12, where the observed ratios are compared with predictions of both the 16 and 19 level code and for temperatures from 10 000 to 20 000 K.

Firstly it is notable that, while at T=10 000 K the inclusion of three further levels does not change the results of the 16 level code, strong differences emerge at higher temperatures (e.g. the ratio 1.257/1.749 decreases by about 70% at T=20 000 K). Secondly, ratios with the 1.814μm, 1.967μm and 2.161μm lines well agree with T$\sim$ 16 000 - 18 000 K.

Finally, the ratio with the 1.749μm line implies T_e $\sim$8 000 K, that we do not consider to be reliable because in the same spatial region examined, bright hydrogen recombination lines are also observed (see Figure 4.7). For this line, however, neither evident mistakes in the Einstein coefficients (all the lists give similar values), nor observational biases (e.g. extinction) are able to explain the disagreement with the other ratios.

[Fe II] abundance

The gas-phase Fe abundance (n(Fe)) is a measure of the shock efficiency in disrupting the cores of the dust grains where iron is locked in quiescent conditions. A very powerful way to estimate the percentage of gas-phase iron using NIR lines, that is based on [Fe II]/[P II] line ratios, has been exposed in Section 2.3.3. In HH99B two [P II] lines are detected, at 1.1471 μm and 1.1885 μm, this latter may be blended with a [Fe II] line (see Table 4.2). According to the analysis described by Oliva et al. (2001), the Equation 2.63 can be written as follows:

$$\frac{n(\mathrm{Fe})}{n(\mathrm{P})} \lesssim 2 \times \frac{I([\mathrm{Fe\,II}]1.257)}{I([\mathrm{P\,II}]1.188)} \simeq \frac{I([\mathrm{Fe\,II}]1.257)}{I([\mathrm{P\,II}]1.147)} \tag{4.1}$$

The above Equation, as stated by the authors, is accurate to within a factor 2 for all the temperature and densities expected within the shocks.
Assuming a solar abundance ratio of ∼100 (Asplund et al. 2005), it is possible to derive the map of the percentage of gas-phase iron (see Figure 4.13). Noticeably, a strong decrease in the percentage of gas-phase iron occurs going from the bow-head (70%) towards the flanks (up to 20%). If compared to the theoretical predictions for the iron depletion degree, the measured values imply that the shock velocity should remain above 100 km s^{-1} even in the bow flanks (Jones 2000).

4.4.2 H_2 analysis

Extinction map

Since H_2 emission comes from different spatial regions from those where [Fe II] emission arises (see Figure 4.7), the derivation of the corresponding extinction map is the first step in the H_2 line analysis.
Out of 21 ratios of lines coming from the same upper level, we considered only the three ratios (i.e. 1-0S(1)/1-0Q(3), 2-0S(1)/2-1S(1), 2-0Q(3)/2-1S(1)) that consist of lines detected at S/N per pixel larger than 5 in the whole region of molecular hydrogen emission. In particular, since the one at the largest S/N (1-0S(1)/1-0Q(3)) suffers from poor atmospheric transmission at the 1-0Q(3) wavelength, the other two ratios were used as calibrators and the 1-0S(1)/1-0Q(3) ratio to probe the differential extinction along the shocked region. The Rieke & Lebofsky (1985) extinction law was adopted.
The final map is shown in Figure 4.14: the covered zone somewhat complements the Av map constructed from [Fe II] lines, with a partial spatial overlap in the areas corresponding to knots B3 and B1. The A_V values range typically from 1 to 4

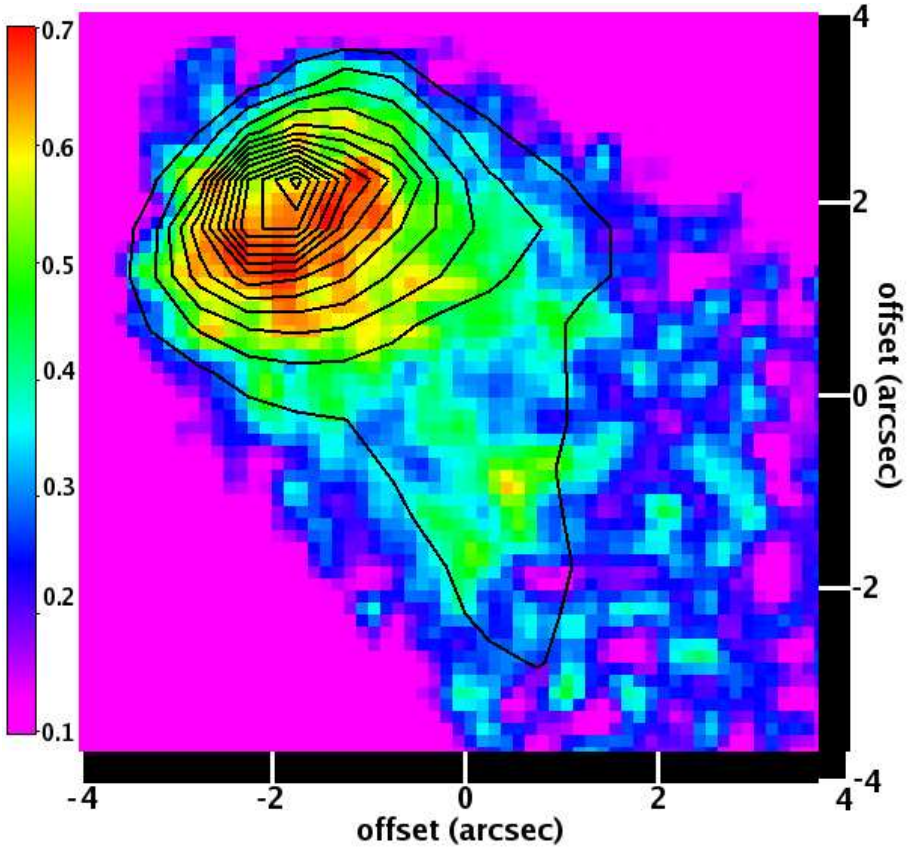

Figure 4.13: Map of the percentage of iron in gas-phase with overlaid intensity contours of the [Fe II] 1.257μm line.

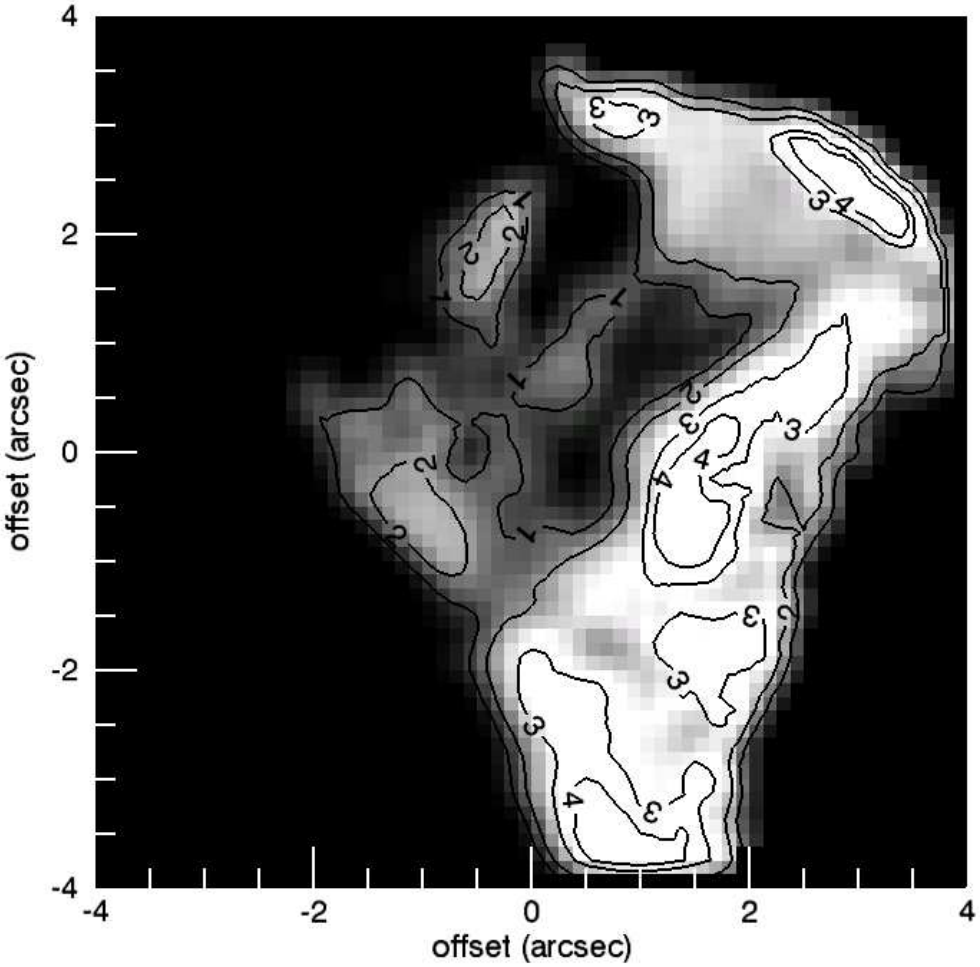

Figure 4.14: Extinction map as derived from H_2 line ratios where contours from A_V=1 to 4 mag are shown.

mag, in substantial agreement with those inferred from [Fe II] emission: therefore this result contrasts with the general trend observed both in other Herbig-Haro objects (e.g. Nisini et al. 2002; Giannini et al. 2004) and with the HH99B value itself measured by McCoey et al. (2004), where the extinction computed from [Fe II] lines is systematically higher than that probed with H_2 lines. This may be because in these cases the extinction was computed from the 1.25μm/1.64μm ratio, for which NS coefficients were used.

Temperature map

The temperature of the molecular gas can be obtained following the standard method of the Boltzmann diagram (see Section 2.3.4). This method was applied to all the pixels of the H_2 images, and the resulting map is shown in Figure 4.15, where contours of temperature are given in units of 10^3 K.
Two main aspects can be evidenced from this map:
(i) a temperature gradient from $\simeq$ 2 000 K up to 6 000 K occurs going from the receding parts of the shock towards the head. It is important to highlight that this gradient can be traced because of the very large number of H_2 lines detected, which cover the Boltzmann diagram up to excitation energies of $\sim$ 38 000 K, therefore sensitively enlarging the dynamical range of temperatures typically probed with H_2 lines;
(ii) two different behaviours in the Boltzmann diagram occur between the bow head and the flanks: as shown in the two examples given in Figure 4.15, while H_2 emission is well fitted by a single temperature (at T$\sim$ 5 000 K) at the bow-head, a curvature exists among the points in the southern flank diagram, where at least two temperature components can be evidenced. In both cases, the little scatter of the data points around the median curve reveals a high degree of thermalization of the molecular gas. Moreover, this result can be generalized to all the bow structure.
The behaviour of the Boltzmann diagram at the bow head testifies for the presence of a fast non-dissociative C-type shock which is capable of reproducing a single, high and thermalized temperature of the molecular gas. We note, however, that a further J-shock component is likely needed to justify both the atomic and molecular emissions occurring at the regions close to the bow head.
The presence of multiple temperature components at the bow flanks can be explained by considering that, given the paraboloid geometry, at least two different components are intercepted along the line of sight: a warm component along the bow surface, that rapidly cools while expanding in the colder external medium,

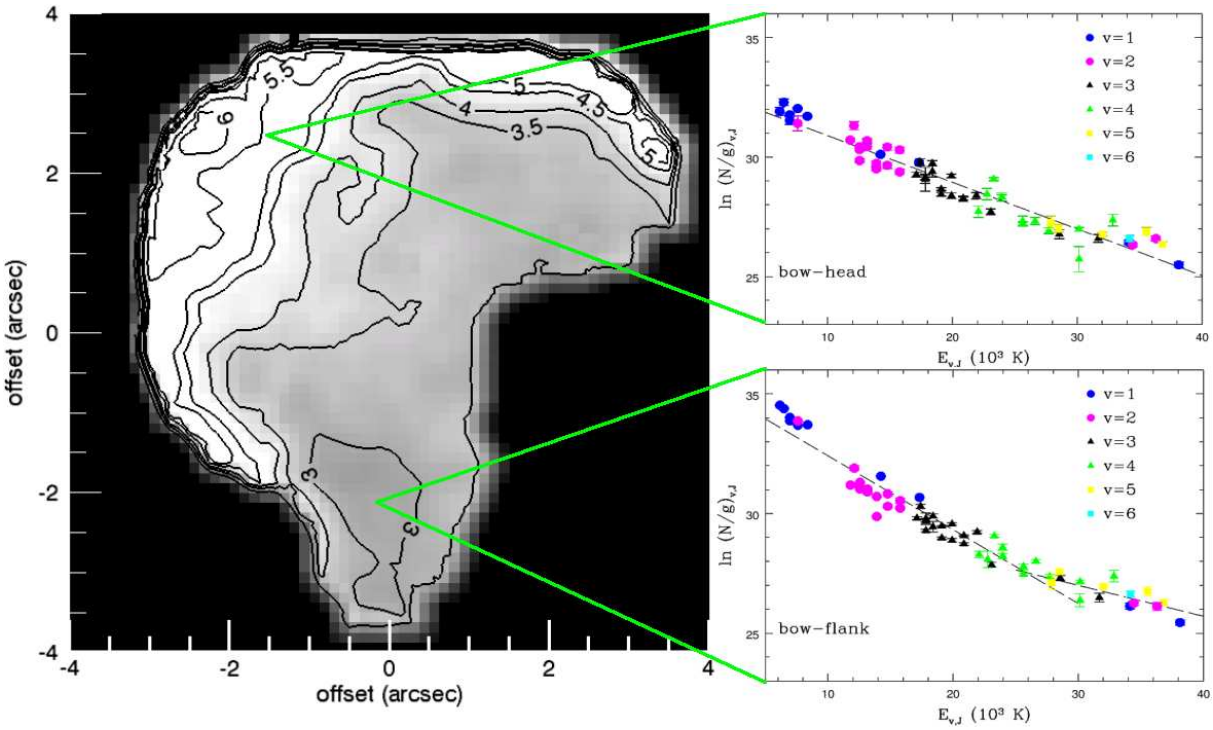

Figure 4.15: Temperature map (in 10^3 K) as derived from H_2 line ratios. As an example, we show the rotational diagrams in two points of the bow: noticeably, while at the bow-head H_2 shows a single temperature at T$\sim$ 5 000 K, in the southern flank two temperature components exist (the average temperature being $\sim$ 2 800 K.)

and a second, hotter component, close to the jet axis, whose temperature is quite similar to that probed at the head. A similar interpretation was given to explain the electron density values in HH120 (see Section 3.2.2), suggesting that the radiation coming from the inner regions is not blocked by the external layers of the bow.

4.4.3 H analysis

At the bow head, some hydrogen recombination lines of the Brackett series along with the Paβ line are observed.

The S/N ratio of these lines, apart from Brγ and Paβ, is indeed so low that a detailed modelling is prevented. Nonetheless, the Paβ/Brγ ratio has been used to derive an independent estimate of the extinction. Under the assumption of case B recombination[3], we obtain $A_V = 1.8 \pm 1.9$ mag.

More interesting parameters, i.e. the hydrogen fractional ionization, x_e and the hydrogen post-shock density, $n_H = n_e/x_e$, are obtainable from the observed inten-

[3]The case B hypothesis assumes that hydrogen recombination lines are optically thin, except for the Lyman series.

sity ratio [Fe II]1.257/Paβ. Under the assumption that iron is single ionized and recalling the Formula 3.4 adopted for the HH240 case (see Section 3.2.3), such a ratio can be expressed as follows:

$$x_e = \chi_{Fe}(\mathrm{Fe/H})_{\odot}[\frac{[\mathrm{Fe\,II}]1.257}{Pa\beta}]^{-1}\frac{\epsilon_{[\mathrm{Fe\,II}]1.257}}{\epsilon_{Pa\beta}} \quad (4.2)$$

being χ_{Fe} the gas-phase iron fraction with respect to the solar Fe abundance, $(\mathrm{Fe/H})_{\odot}$ and $\epsilon_{[\mathrm{Fe\,II}]1.257}$ and $\epsilon_{Pa\beta}$ (in erg cm^3 s^{-1}) the emissivities of the two lines, having taken $\epsilon_{Pa\beta}$ from Storey & Hummer (1995).
The above quantity was computed in the physical conditions derived at the bow head, i.e. T=16 000 K, n_e=6 10^3 cm^{-3}, $\chi_{Fe} \sim 0.7$ and having taken $(\mathrm{Fe/H})_{\odot}$ = 2.8 10^{-5} (Asplund et al. 2005). This leads to x_e = 0.4 - 0.5 and n_H between 0.8 and 1.4 10^4 cm^{-3}. In the receding parts of the shocks, the fractional ionization cannot be computed directly, since there is not estimate for the electron temperature. However, under reasonable assumptions that T $\leq$ 10 000 K a sharp decrease of x_e is expected: for example, for the region where δ_{Fe}=0.3 - 0.4, it follows that x_e = 0.2 - 0.3, estimates that are in agreement with those inferred along other Herbig-Haro objects through optical line diagnostics (e.g. Hartigan & Morse 2007; Bacciotti & Eislöffel 1999) or with those between 0.03 and 0.6 inferred in a number of jets by combining optical and infrared observations (Podio et al. 2006; Nisini et al. 2005).

4.5 Kinematic properties

4.5.1 H_2

In this Section, we intend to characterize the kinematic parameters of the shock(s) occurring in HH99B.
This topic was already discussed by Davis et al. (1999), which we will use for comparison to the results found in our work. The higher spectral resolution (R$\sim$ 15 kms^{-1}) of the observations of Davis et al. (1999), obtained with echelle spectroscopy, have revealed that the peak velocity of the H_2 2.12μm line moves progressively from slightly blue-shifted values near the shock front towards red-shifted values in the flanks, and has been interpreted in the framework of a receding bow shock orientated with respect to the line of sight of about 45°.
Nominally, the spectral resolution of SINFONI K band observations (R$\sim$85 km s^{-1}) does not reveal variations of the order of those measured by Davis et al. (1999); this limitation, however, is partially compensated by the very high S/N

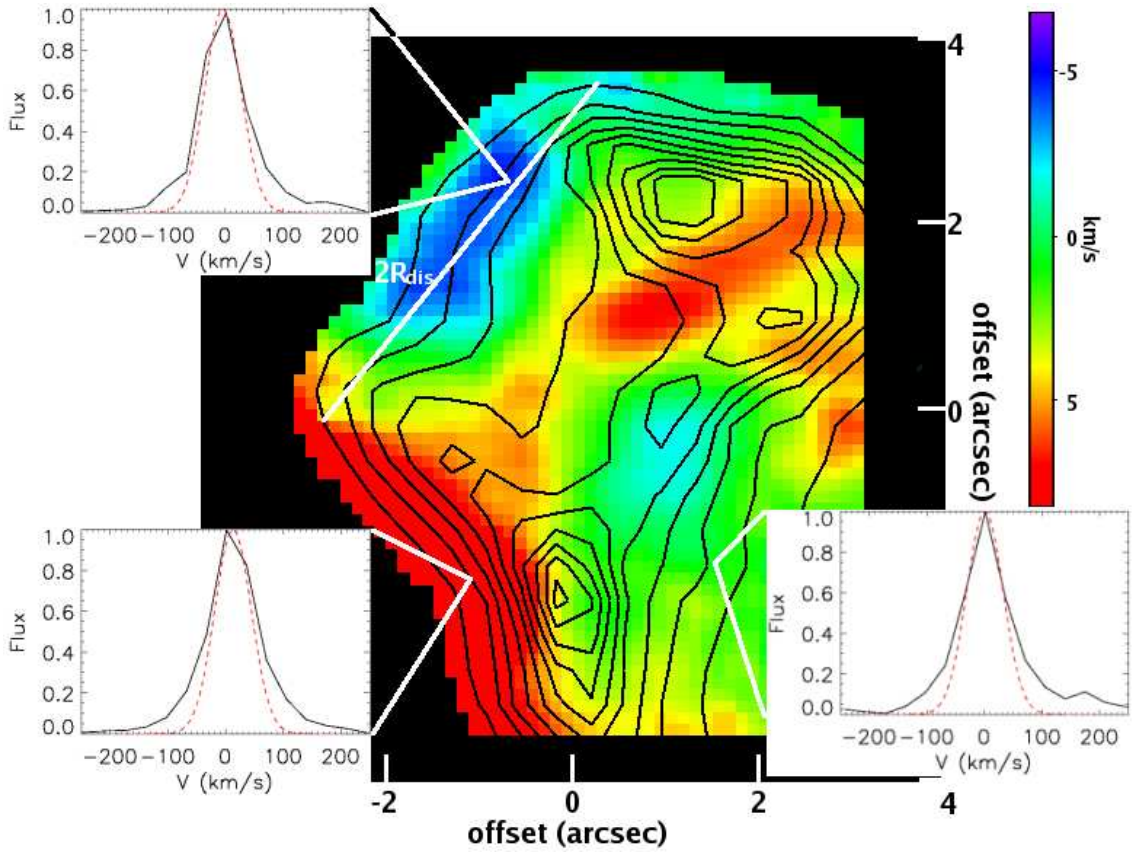

Figure 4.16: Local standard of rest (LSR) velocity map of the 2.122μm line peak, with superimposed line intensity contours. The diameter $2R_{dis}$ of the last cap beyond which the bulk of H_2 is dissociated is indicated with a white line (see Section 2.2). Insets show the line profile observed at the bow head (top left), in the southern flank (bottom left) and at the bow centre (bottom right). Blue and red asymmetries are visible at the bow head and along the flanks, while the line is symmetric toward the centre. The instrumental profile, measured on OH atmospheric lines, is shown for comparison (red dashed line).

ratio at which we detect the 2.12μm line. In practice, although we cannot give numerical estimates on the line parameters (v_{peak}, FWHM, see Section 2.2.1), a trend on both the peak velocity and on the profile shape can be seen along the bow structure.

Figure 4.16 represents the v_{peak} map obtained from the 2.12μm line, where the contours of the intensity (de-reddened) of the 2.12μm itself have been superposed. Overall, our results confirm those of Davis et al. (1999): the line profile presents a blue-shifted component towards the shock front at the bow head (B0), while the opposite occurs along the two flanks and especially along the edge of the B1 flank (not covered by the echelle spectra in Davis et al. 1999), where the line peak is shifted by $\sim +15$ km s^{-1} with respect to the line profile at the head. Analogous to the spectra of Davis et al. (1999), the 2.12μm profile does not show double peaked components, as generally expected for a parabolic bow structure (see Section 2.2)

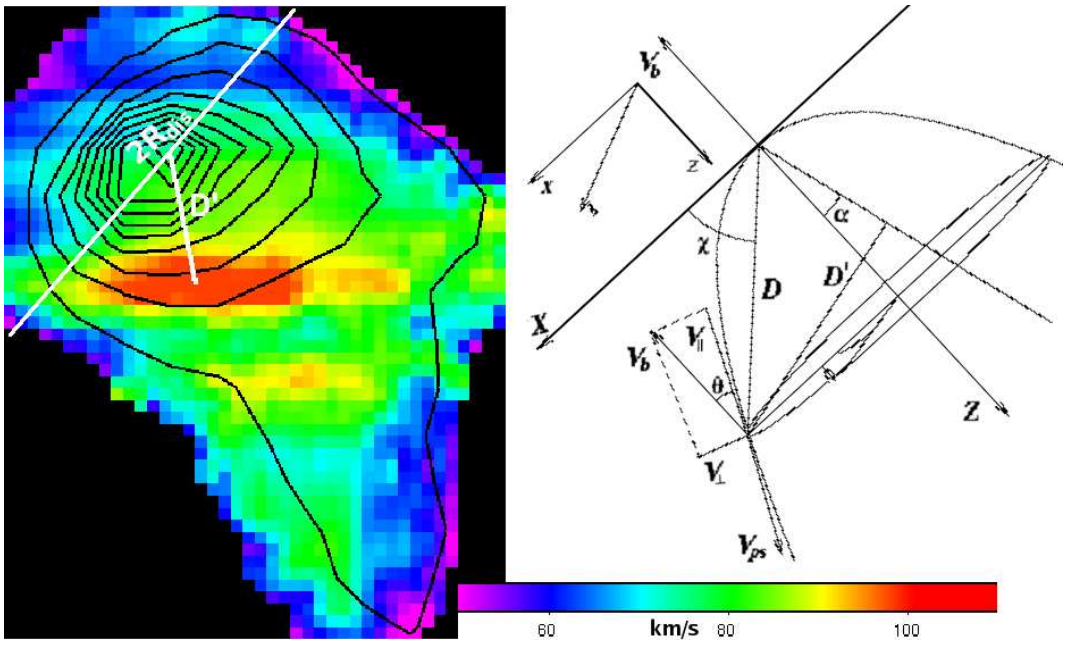

Figure 4.17: The local standard of rest (LSR) velocity map of the 1.257μm line peak, with superimposed line intensity contours, is compared with the bow shock model described in Section 2.2. The line is red-shifted all along the bow-structure, with a peak at about +70 km s^{-1}. The projection D' along the line of sight of the distance between the line emission peak and the maximum radial velocity is shown, along with the diameter 2R$_{dis}$ of the last cap beyond which H_2 is dissociated (see Figure 4.16).

though it does become wider near the centre of the bow, where the opposite sides are seen in projection. Here the observed FHWM$_{obs}$ is 85-105 km s^{-1}, that, once deconvolved with the instrumental profile width (see Equation 2.40), measured on atmospheric OH lines, roughly gives an intrinsic line width, of $\sim$ 20-40 km s^{-1}. The consistence with previous observations is also maintained along the bow flanks, where the profile width becomes narrower decreasing toward the spectral resolution limit on the intrinsic width of $\sim$ 20 km s^{-1}.
However, a sudden increase of the line width (FHWM$_{obs}$) is seen at the edge of the southern flank, where we measure up to $\sim$ 115 km s^{-1}, i.e. an intrinsic width of $\sim$ 70 km s^{-1}, which is close to the maximum shock velocity ($\sim$ 80 km s^{-1}) at which H_2 can survive against dissociation, predicted by the C-shock model by Le Bourlot et al. (2002) (see Section 2.2). This last topic will be treated more extensively in the next Section.

4.5.2 [Fe II]

The kinematic analysis of the ionic gas component was performed on the two brightest [Fe II] lines at 1.257 and 1.644 μm.

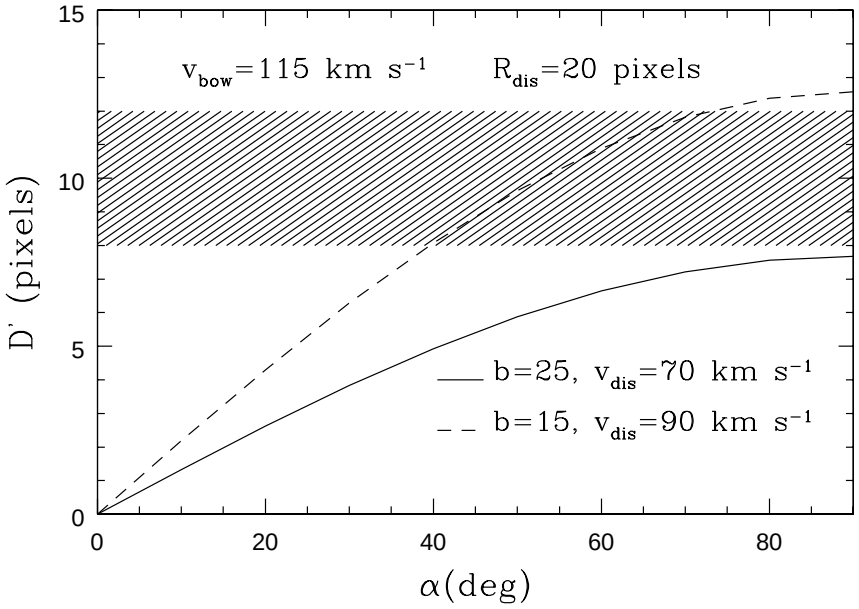

Figure 4.18: Projection over the sky plane of the distance between the line emission peak and the maximum radial velocity plotted against the bow inclination angle.

Both appear resolved in velocity and give similar results for the line profile shape (which is Gaussian across the whole bow), the intrinsic line width, the peak position and the FWZI. This last result, in particular, gives a direct measure of the shock speed at the bow apex (see Section 2.2): we obtain $V_{bow} \sim 115$ km s^{-1}, which agrees well with the prediction by Davis et al. (1999) (80-120 km s^{-1}) derived from the overall shape of the bow and the characteristics of the H_2 2.122μm line profile.

Figure 4.17 shows the radial velocity map of the 1.644μm line: this appears redshifted over the whole bow structure, confirming the analysis performed with the molecular gas, the maximum shift occurring towards the image centre.

We interpret this behaviour as a geometrical effect due to the inclination of the bow with respect to the line of sight. Indeed, if the bow is observed at a certain angle $\alpha \neq 0°, 180°$, the peak of the radial velocity component is seen apart from the bow apex. With reference to Figure 4.17 and assuming the bow shock model described in Section 2.2, we can express the projected distance D$'$ between the emission and the radial velocity peaks as follows:

$$\begin{aligned} D' &= D \cdot \cos(\chi - \alpha) \\ &= \sqrt{z_M^2 + 2 z_M b} \cdot \cos(\chi - \alpha) \end{aligned} \tag{4.3}$$

Table 4.3: Physical parameters estimated in HH99B.

Parameter	This work	McCoey et al. (2004)	Davis et al. (1999)
A_V(Fe II) (mag)	1-4	4-10	-
$A_V(H_2)$ (mag)	2-4	<4	<4.6
A_V(H) (mag)	∼2	-	-
n_e (cm^{-3})	3-6 10^3	-	-
T_e (K)	≤ 16 000	-	-
T_{H_2} (K)	2 500 - 6 000	2 000 - 4 000	-
N_{H_2} (cm^{-2})	3 10^{16} - 2 10^{17}	-	
$\chi_{\rm Fe\,II}$	0.2-0.7	0.25	-
x_e	0.2-0.6	-	-
n_H (cm^{-3})	$\sim 10^4$ (post-shock)	10^4 (pre-shock)	-
V_{bow} (km s^{-1})	110-120 ([Fe II])	50 ([Fe II])	80-120 (H_2)
inclination angle (°)	40-60	-	45

where is z_M the distance along the $z-$axis at which the radial velocity reaches its maximum;

$$\begin{aligned} z_M &= \frac{b}{2}\left[\left(\frac{1}{\sin\theta_M^2}\right)^2 - 1\right] \\ &= \frac{b}{2}\left[\left(\frac{1}{\cos(\alpha/2)}\right)^2 - 1\right] \end{aligned} \tag{4.4}$$

The b parameter is expressed by the Equation 2.34, thus D', which can be directly measure on the velocity map (see Figure 4.17) is a function of α and the H_2 breakdown velocity (V_{dis}), once measures of V_{bow} and R_{dis} (see Figure 4.16) are performed.

The result is depicted in Figure 4.18: interestingly, α values are close to those inferred by Davis et al. (1999) for a range of V_{dis} between 70 and 90 km s^{-1}.

These values can be considered as an indirect measurement of a parameter whose theoretical predictions are so far somewhat controversial, as was discussed in Section 2.2. Moreover the predicted values for V_{dis} are fully consistent with the high FWHM of the 2.122μm line measured in the southern flank (see Section 4.5.1) and reinforce the hypothesis that a fast, continuous shock is responsible for the excitation of the molecular gas at the apex of the bow (see Section 4.4.2).

4.6 Concluding remarks

In this Chapter bi-dimensional, deep near-infrared spectral images of the bow shock HH99B, acquired with the new instrument SINFONI, were presented. These have allowed, for the first time, to accurately derive the physical parameters of both the molecular and ionic gas components (summarized in Table 4.3, where our results are compared with those derived in previous works), and, at the same time, to characterize the geometry and the kinematical properties of the flow. The main results of this study are the following:

- More than 170 emission lines have been detected, mainly ro-vibrational H_2 and [Fe II] lines, many of them never observed before in an Herbig-Haro object. In addition, transitions of hydrogen and helium recombination and fine structure lines of [P II], [Ti II] and possibly [Co II] have been observed.

- A clear bow-shape morphology emerges from the line intensity maps. [Fe II] and other ionic emission reach the peak intensity at the bow-head (B0) whereas H_2 emissions delineate the bow flanks, reaching a peaking in the knots B1 and B3. Noticeably, the H_2 lines with the highest excitation energy ($E_{up} > 30\,000$ K) show a different morphology, being strong towards the bow-head. This implies that H_2 still survives in this zone, even though there is a significant temperature enhancement.

- Extinction maps have been derived from the analysis of both [Fe II] and H_2 lines. These give similar results, with A_V ranging between 1 and 4 mag.

- A detailed electron density map has been obtained in the framework of NLTE approximation for [Fe II] line emissions. This remains almost constant in the [Fe II] emission zone, peaking towards the bow-head. From the same emission, we are able to probe a variation of the electron temperature, which falls from $\sim 16\,000$ K at the apex to less than 10 000 K in the receding parts of the bow.

- An iron depletion degree not higher than 30% has been inferred at the bow apex, which testifies in favour of a J-type shock as the main excitation mechanism in this part of the bow. In this same zone, we infer a fractional ionization of ~ 0.6 and a post-shock density of $\sim 6{\cdot}10^3$ cm^{-3}.

- Analysis of H_2 line emission allowed for probing the molecular temperature variation. In particular, while at the bow apex a temperature of $\sim 6\,000$ K was reached, due probably to the presence of a fast, non dissociative

shock, along the flanks different temperature components are simultaneously present. This was interpreted as a geometric effect, caused to the observation of regions at different temperature in the rear part of the bow.

- From the brightest [Fe II] and H_2 lines we probed the kinematical properties (e.g. shock velocity) of the shocked gas. In particular, we confirm the result by Davis et al. (1999) according to which HH99 is a red-shifted, receding bow.

- The radial velocity map of [Fe II] emission, has been interpreted in the framework of the bow geometry. From this map we have consistently inferred the bow inclination angle and defined a range of 70-90 km s^{-1} for the H_2 breakdown velocity. Moreover these breakdown velocity values are compatible with the estimated electron density values (see Figure 2.9). We propose our method as a valuable tool to derive the jets inclination angle (if larger than 10-20°) in cases where proper motion is unknown.

- The kinematical parameters of the [Fe II] emission estimated in this work do not confirm the model predictions by McCoey et al. (2004). In particular, these authors hypothesize the [Fe II] lines as originating in a pure J-type shock with $V_{shock} \sim 50$ km s^{-1}, that contrasts with our measure of $V_{shock} \sim$ 110-120 km s^{-1}. Thus, the interpretation on the origin of the [Fe II] emission should be maybe revised.

Conclusions

The aim of this thesis is to investigate the properties of shocks occurring between protostellar jets and the surrounding enviroment from the analysis of NIR spectra and spectral images of a sample of "bow shocks" (Herbig-Haro objects).
For this analysis two different observational techniques were used:
(i) the "well-known" NIR long-slit spectroscopy, performed with the ISAAC spectrograph both in high ($R \sim 10\,000$) and low ($R \sim 800$) resolution mode. The sources HH26, HH120 and HH240 were observed with this technique;
(ii) the "innovative" IFU (Integral Fiel Unit) spectroscopy, never used before for this purpose, performed with SINFONI spectrograph in medium ($R \sim 3\,000$) resolution mode. A well known prototype of bow shock, that is HH99, was observed with this technique, in order to test the diagnostic capabilities of the IFU spectroscopy in reproducing the variations of physical and kinematic parameters through the bow surface.
The main results of this work can be summarized as follows:

- A wide number of ro-vibrational H_2 lines (e.g in HH240 and in HH99) were detected. In particular, many of them were never observed before in HH objects, in particular transitions coming from rotational levels $v = 5$, $v = 6$ and $v = 7$, which generally correspond to lines with high excitation energies ($E_{up} > 30\,000$).

- Many atomic lines were observed. Most of them are [Fe II] lines, as well as hydrogen and helium recombination lines and fine structure lines of [P II], [Ti II], [SiI] and [Co II].

- H_2 and [Fe II] emissions originate in separate regions inside the bow structure and trace different shock conditions. This aspect has been pointed out in the spectral images of HH120 and it becomes particularly evident in the case of HH99, where a clear bow-shape morphology emerges from the line intensity maps; [Fe II] and other ionic emissions reach the peak intensity at the head of the bow, whereas H_2 emissions delineate the bow flanks.

- Molecular and atomic emissions were used to establish the kinematic properties, through the measurements of radial velocities and velocity dispersions. Position-Velocity diagrams of HH26 and HH120 show that the observed knots belong to the blue-shifted lobe of the outflows generated by HH26IRS and IRS4, respectively. In the HH120 case, red-shifted knots symmetrically distribuited with respect to IRS4 have been identified belonging to a counterjet.
  The radial velocity maps of HH99, obtained from the brightest [Fe II] and H_2 lines, were interpreted in the framework of a receding, parabolic bow. From these maps we have consistently inferred a bow inclination angle of 40-60° and a dissociation velocity for the molecular hydrogen of 70-90 km s^{-1}. The latter represents the first observational evidence that H_2 can survive against dissociation well above its dissociation potential of $\sim$ 24 km s^{-1}.

- HH26 represents an excellent example of the kinematic evolution of the flow from the exciting source up to the terminal bow shock. The observations revel the presence of an accelerating microjet close to the driving source, followed by several decelerating knots. Such deceleration corresponds to an enhancement of the gas temperature, which rises of $\sim$ 600 K from the microjet region to the external shock surface.

- The H_2 lines with the highest excitation energy ($E_{up} > 30\,000$ K) observed in HH99 show an unexpected morphology, being strong towards the bow-head with respect to the flanks. This result shows that high excitation and low excitation molecular hydrogen lines distribute differently along the shock structure.

- In the framework of the Boltzmann diagrams we have built a map of the temperature of the molecular gas for HH99, finding a decrease from the bow head ($\sim$ 6 000 K) to the receding parts of the shocks ($\sim$ 2 000 K).

- From the displacement of the points in the Boltzmann diagram, the physical characteristics of the shock can be inferred and, in particular, the diagrams obtained for HH26, HH240 and HH99 show that a J-type shock with magnetic precursor is the type of shock which best fits the observations.

- A correspondence between local excitation conditions and shock velocity is found. In particular, in HH26, where the observed emission is constituted mainly by molecular hydrogen lines and the ionic emission is faint, the shock velocity does not exceed 60 km s^{-1}; the opposite occuring in HH120 and

HH99, where the copious ionic emission originates in shocks travelling at speeds higher than 100 km s^{-1}.

- Atomic lines were used to estimate the physical parameters of the observed shock regions, such as electron density, electron temperature, visual extinction, iron depletion and the hydrogen ionization fraction. In the case of HH99, these parameters were inferred as maps which display the variations along the shock structure.
  A NLTE model for [Fe II] line emissions was adopted to measure the electron density in HH120 and HH99, obtaining values which range from 2 to 6 10^3 cm^{-3}, and to probe in HH99 a variation of the electron temperature, which falls from $\sim$ 16 000 K at the bow apex to less than 10 000 K in the receding parts of the bow. The detection of [PII] lines and hydrogen recombination lines allow us to estimate the percentage of iron gas-phase and the hydrogen ionization fraction in HH240 and HH99; a iron depletion degree not higher than 30% and a fractional ionization of $\sim$ 0.5 were inferred in these sources, testifing for the presence of a fast component of the shock able to disrupt the dust grains and to efficiently ionize atoms.

The analysis presented in this thesis shows the limit of the long-slit spectroscopy for investigating the properties of protostellar shocks and, at the same time, reveals the potentiality of IFU spectroscopy for obtaining a complete description of these. In the near future, this kind of observations will be performed on other HH objects, in order to obtain a wider sample of observational results; the final aim is to provide a more realistic view of the physical processes occurring through the bow shock surface and to constrain, with observational data, the development of bi-dimensional shock models, which result more suitable for describing curve shaped shocks.

Bibliography

Anthony-Twarog, B. J. 1982, AJ, 87, 1213

Asplund, M., Grevesse, N., & Sauval, A. J. 2005, in Astronomical Society of the Pacific Conference Series, Vol. 336, Cosmic Abundances as Records of Stellar Evolution and Nucleosynthesis, ed. T. G. Barnes, III & F. N. Bash, 25

Bacciotti, F. & Eislöffel, J. 1999, A&A, 342, 717

Bachiller, R. 1996, ARA&A, 34, 111

Bachiller, R. & Tafalla, M. 1999, in NATO ASIC Proc. 540: The Origin of Stars and Planetary Systems, ed. C. J. Lada & N. D. Kylafis, 227

Bally, J. & Lada, C. J. 1983, ApJ, 265, 824

Beck-Winchatz, B., Bohm, K.-H., & Noriega-Crespo, A. 1996, AJ, 111, 346

Benedettini, M., Giannini, T., Nisini, B., et al. 2000, A&A, 359, 148

Blitz, L. 1993, in Protostars and Planets III, ed. E. H. Levy & J. I. Lunine, 125–161

Bohigas, J., Persi, P., & Tapia, M. 1993, A&A, 267, 168

Bonnet, H., Conzelmann, R., Delabre, B., et al. 2004, in Presented at the Society of Photo-Optical Instrumentation Engineers (SPIE) Conference, Vol. 5490, Advancements in Adaptive Optics. Edited by Domenico B. Calia, Brent L. Ellerbroek, and Roberto Ragazzoni. Proceedings of the SPIE, Volume 5490, pp. 130-138 (2004)., ed. D. Bonaccini Calia, B. L. Ellerbroek, & R. Ragazzoni, 130–138

Bontemps, S., Andre, P., Terebey, S., & Cabrit, S. 1996, A&A, 311, 858

Burton, M. G. 1992, Australian Journal of Physics, 45, 463

Calzoletti, L., Giannini, T., Nisini, B., & Lorenzetti, D. 2007, A&A, in preparation

Caratti o Garatti, A., Eislöffel, J., Froebrich, D., et al. 2007, A&A, in press

Caratti o Garatti, A., Giannini, T., Nisini, B., & Lorenzetti, D. 2006, A&A, 449, 1077

Caselli, P., Walmsley, C. M., Terzieva, R., & Herbst, E. 1998, ApJ, 499, 234

Chrysostomou, A., Hobson, J., Davis, C. J., Smith, M. D., & Berndsen, A. 2000, MNRAS, 314, 229

Combes, F. 1991, ARA&A, 29, 195

Crutcher, R. M. 1999, ApJ, 520, 706

Davis, C. J., Berndsen, A., Smith, M. D., Chrysostomou, A., & Hobson, J. 2000, MNRAS, 314, 241

Davis, C. J., Ray, T. P., Desroches, L., & Aspin, C. 2001, MNRAS, 326, 524

Davis, C. J., Ray, T. P., Eisloeffel, J., & Corcoran, D. 1997, A&A, 324, 263

Davis, C. J., Smith, M. D., Eislöffel, J., & Davies, J. K. 1999, MNRAS, 308, 539

Draine, B. T. 1980, ApJ, 241, 1021

Draine, B. T., Roberge, W. G., & Dalgarno, A. 1983, ApJ, 264, 485

Eisenhauer, F., Abuter, R., Bickert, K., et al. 2003, in Presented at the Society of Photo-Optical Instrumentation Engineers (SPIE) Conference, Vol. 4841, Instrument Design and Performance for Optical/Infrared Ground-based Telescopes. Edited by Iye, Masanori; Moorwood, Alan F. M. Proceedings of the SPIE, Volume 4841, pp. 1548-1561 (2003)., ed. M. Iye & A. F. M. Moorwood, 1548–1561

European Southern Observatory. 1998, The VLT White Book (The VLT White Book, Publisher: Garching near Munich: European Southern Observatory (ESO), 1998)

Evans, II, N. J. 1999, ARA&A, 37, 311

Ferreira, J. 2002, in EAS Publications Series, Vol. 3, EAS Publications Series, ed. J. Bouvier & J.-P. Zahn, 229–277

Flower, D. R., Le Bourlot, J., Pineau des Forêts, G., & Cabrit, S. 2003, MNRAS, 341, 70

Flower, D. R. & Pineau des Forêts, G. 1999, MNRAS, 308, 271

Garcia Lopez, R., Nisini, B., Giannini, T., & Lorenzetti, D. 2007, A&A, in preparation

Genzel, R. 1991, in NATO ASIC Proc. 342: The Physics of Star Formation and Early Stellar Evolution, ed. C. J. Lada & N. D. Kylafis, 155

Giannini, T., McCoey, C., Caratti o Garatti, A., et al. 2004, A&A, 419, 999

Giannini, T., McCoey, C., Nisini, B., et al. 2006, A&A, 459, 821

Giannini, T., Nisini, B., Caratti o Garatti, A., & Lorenzetti, D. 2002, ApJ, 570, L33

Gibb, A. G. & Heaton, B. D. 1993, A&A, 276, 511

Goodman, A. A., Benson, P. J., Fuller, G. A., & Myers, P. C. 1993, ApJ, 406, 528

Graham, J. A. & Heyer, M. H. 1989, PASP, 101, 573

Gredel, R. 1994, A&A, 292, 580

Gredel, R. 2006, A&A, 457, 157

Gueth, F. & Guilloteau, S. 1999, A&A, 343, 571

Haro, G. 1953, ApJ, 117, 73

Hartigan, P. & Graham, J. A. 1987, AJ, 93, 913

Hartigan, P. & Morse, J. 2007, ApJ, 660, 426

Hartigan, P., Raymond, J., & Hartmann, L. 1987, ApJ, 316, 323

Heiles, C., Goodman, A. A., McKee, C. F., & Zweibel, E. G. 1993, in Protostars and Planets III, ed. E. H. Levy & J. I. Lunine, 279–326

Herbig, G. H. 1950, ApJ, 111, 11

Hollenbach, D. 1997, in IAU Symposium, Vol. 182, Herbig-Haro Flows and the Birth of Stars, ed. B. Reipurth & C. Bertout, 181–198

Jeans, J. H. 1902, Phil. Trans. Roy. Soc., 199, 1

Jones, A. P. 2000, J. Geophys. Res., 105, 10257

Jones, B. F., Cohen, M., Wehinger, P. A., & Gehren, T. 1987, AJ, 94, 1260

Kaufman, M. J. & Neufeld, D. A. 1996, ApJ, 456, 611

Konigl, A. & Pudritz, R. E. 2000, Protostars and Planets IV, 759

Kwan, J. 1977, ApJ, 216, 713

Le Bourlot, J., Pineau des Forêts, G., Flower, D. R., & Cabrit, S. 2002, MNRAS, 332, 985

Lorenzetti, D., Giannini, T., Vitali, F., Massi, F., & Nisini, B. 2002, ApJ, 564, 839

Mac Low, M.-M. & Klessen, R. S. 2004, Reviews of Modern Physics, 76, 125

Marraco, H. G. & Rydgren, A. E. 1981, AJ, 86, 62

McCoey, C., Giannini, T., Flower, D. R., & Caratti o Garatti, A. 2004, MNRAS, 353, 813

Mestel, L. & Spitzer, Jr., L. 1956, MNRAS, 116, 503

Milman, A. S. 1975, ApJ, 202, 673

Moorwood, A. 1998, in NICMOS and the VLT: A New Era of High Resolution Near Infrared Imaging and Spectroscopy, Pula, Sardinia, Italy, June 26-27th 1998 ESO Conference and Workshop Proceedings 55, 1998, ed. W. Freudling & R. N. Hook, 6

Mouri, H. & Taniguchi, Y. 2000, ApJ, 534, L63

Munoz-Tunon, C., Gavryusev, V., & Castoneda, H. O. 1995, AJ, 110, 1630

Nisini, B., Bacciotti, F., Giannini, T., et al. 2005, A&A, 441, 159

Nisini, B., Caratti o Garatti, A., Giannini, T., & Lorenzetti, D. 2002, A&A, 393, 1035

Nussbaumer, H. & Storey, P. J. 1988, A&A, 193, 327

O'Connell, B., Smith, M. D., Davis, C. J., et al. 2004, A&A, 419, 975

Oliva, E., Marconi, A., Maiolino, R., et al. 2001, A&A, 369, L5

Pavlovski, G. 2004, PhD thesis, Queen's University of Belfast

Pettersson, B. 1984, A&A, 139, 135

Podio, L., Bacciotti, F., Nisini, B., et al. 2006, A&A, 456, 189

Quinet, P., Le Dourneuf, M., & Zeippen, C. J. 1996, A&AS, 120, 361

Richer, J. S., Shepherd, D. S., Cabrit, S., Bachiller, R., & Churchwell, E. 2000, Protostars and Planets IV, 867

Rieke, G. H. & Lebofsky, M. J. 1985, ApJ, 288, 618

Sauty, C., Tsinganos, K., & Trussoni, E. 2002, in Lecture Notes in Physics, Berlin Springer Verlag, Vol. 589, Relativistic Flows in Astrophysics, ed. A. W. Guthmann, M. Georganopoulos, A. Marcowith, & K. Manolakou, 41

Scalo, J. M. 1986, Fundamentals of Cosmic Physics, 11, 1

Schultz, A. S. B., Burton, M. G., & Brand, P. W. J. L. 2005, MNRAS, 358, 1195

Schwartz, R. D. & Greene, T. P. 2003, AJ, 126, 339

Shu, F. H. & Shang, H. 1997, in IAU Symposium, Vol. 182, Herbig-Haro Flows and the Birth of Stars, ed. B. Reipurth & C. Bertout, 225–239

Smith, M. D. 1991, MNRAS, 252, 378

Smith, M. D. & Brand, P. W. J. L. 1990, MNRAS, 245, 108

Smith, N. & Hartigan, P. 2006, ApJ, 638, 1045

Stahler, S. W. & Palla, F. 2005, The Formation of Stars (The Formation of Stars, by Steven W. Stahler, Francesco Palla, pp. 865. ISBN 3-527-40559-3. Wiley-VCH , January 2005.)

Stahler, S. W., Shu, F. H., & Taam, R. E. 1980a, ApJ, 241, 637

Stahler, S. W., Shu, F. H., & Taam, R. E. 1980b, ApJ, 242, 226

Storey, P. J. & Hummer, D. G. 1995, VizieR Online Data Catalog, 6064, 0

Tomisaka, K., Ikeuchi, S., & Nakamura, T. 1988, ApJ, 326, 208

Walmsley, C. M., Natta, A., Oliva, E., & Testi, L. 2000, A&A, 364, 301

Zhang, H. L. & Pradhan, A. K. 1995, A&A, 293, 953

Zuckerman, B. & Evans, II, N. J. 1974, NASA STI/Recon Technical Report N, 75, 10885